UNIVERSITÀ DEGLI STUDI DI PADOVA

UNIVERSITA' DEGLI STUDI DI PADOVA

Dipartimento di Ingegneria Industriale DII

Corso di Laurea Magistrale in Energy Engineering

Modelling of All Vanadium Redox Flow Batteries with COMSOL Multiphysics

Relatore:
Prof. Andrea Trovò

Correlatori:
Dott. Nicolò Zatta
Dott. Matteo Rugna

Laureando:
Davide Bordignon
Matricola 2076787

Anno Accademico 2023/2024

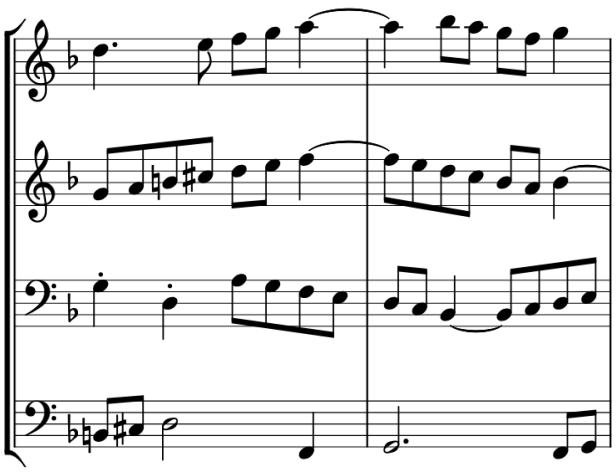

J.S. Bach, The Art of Fugue, Contrapunctus X, Measure 17-18

Abstract

Vanadium redox flow batteries (VRFBs) have gained prominence as a pivotal technology for the storage of large-scale energy, particularly within the realm of renewable energy systems. The complexity inherent in precisely determining the internal dynamics of VRFBs and refining their design based on empirical data presents a substantial challenge. In this context, the formulation of mathematical models that leverage observable parameters like voltage and current emerges as a critical, and indispensable, strategy. This thesis work embarks on an investigative journey into the dynamic models present within existing literature as its initial step. It then progresses to the creation of a comprehensive 2D Multiphysics model, which sets the stage for the subsequent development of an advanced 3D Multiphysics model utilizing the capabilities of the COMSOL Multiphysics® simulation platform.

Significant emphasis is placed on the validation of these models. The models are validated through a meticulous process of parameter calibration and physics reformulation using empirical datasets. This rigorous validation ensures the models are reliable and applicable to real-world scenarios. By comparing the simulated results with actual data, the study confirms the accuracy of the models and their ability to replicate and predict the complex behaviors of VRFB systems.

The work concludes by discussing the remaining challenges in the field and suggests potential directions for future research. It highlights how these mathematical models not only enhance our understanding but also aid in the optimization of VRFB systems.

This work highlights the importance of mathematical modeling in advancing VRFB technology and provides a solid basis for further enhancements in the management and optimization of large-scale energy storage systems.

INDEX

Chapter 1

Introduction

The increasing adoption of renewable energy sources has brought attention to advanced energy storage systems, where flow batteries emerge as a promising solution. This introduction aims to outline the context and rationale behind research focused on the development of flow battery. It sets the foundation by elucidating the operational principles, advantages, and challenges of Redox Flow Batteries, highlighting their significance in energy storage applications. It then delves into the specificities of Vanadium-based systems, discussing the unique properties of Vanadium ions that make All Vanadium Redox Flow Batteries (AVRFB) a promising solution for large-scale energy storage. This chapter aims to bridge the gap between general RFB technology and the specific attributes of Vanadium, setting the stage for a deeper exploration of AVRFB modelling

1.1. Context and Principles of Flow Batteries

1.1.1. The Necessity of Energy Storage Systems

The integration of renewable energy sources into the power grid presents unique challenges due to the inherent variability and intermittency of these sources. Renewable energy, derived from sources such as solar and wind, is characterized by its fluctuating nature. The intermittent availability of these energy sources can lead to imbalances between energy generation and consumption, posing a significant challenge to grid stability.

To maintain a reliable and stable power supply, it is crucial to match electricity generation with demand in real-time. Energy storage systems play a pivotal role in grid balancing by storing excess energy during periods of high generation and releasing it when demand exceeds supply, as shown in Figure 1.1.1. This capability enhances the overall stability and reliability of the power grid.

Energy storage systems contribute to environmental sustainability by facilitating the efficient use of renewable energy, reducing the reliance on fossil fuels, and decreasing greenhouse gas emissions. This aligns with global efforts to transition towards a low-carbon and sustainable energy future.

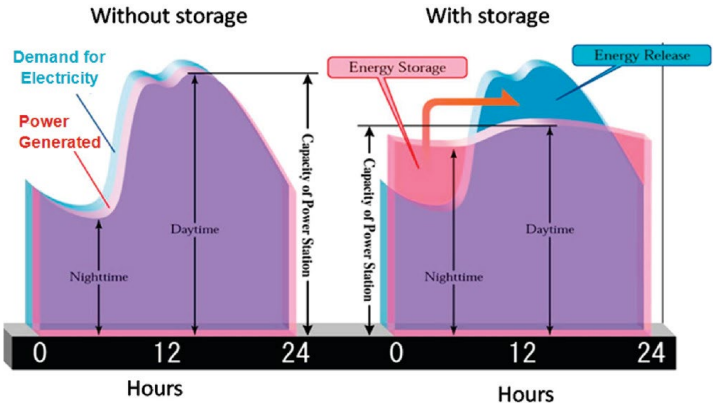

Figure 1.1.1 - Schematic of balancing generation and demand via load leveling, a typical case of load shifting. [1]

1.1.2. The Prominence of Redox Flow Batteries

Among the myriad of energy storage technologies, Redox Flow Batteries (RFBs) emerge as a compelling choice due to their unique characteristics. Unlike conventional solid-state batteries, RFBs store energy in liquid electrolyte solutions, contained in external tanks. This design offers unparalleled scalability and flexibility, allowing for the independent scaling of power and energy capacity by adjusting the size of the electrolyte tanks and the surface area of the electrochemical cell, respectively. RFBs are particularly suited for applications requiring large-scale energy storage, such as grid stabilization and peak shaving, where their ability to provide long-duration discharge becomes invaluable.

Flow batteries play a central role in the realm of energy storage systems, representing an advanced and promising solution to meet the needs of a sustainable energy transition. Flow batteries find widespread use in both large-scale grid systems and microgrids, where their versatility and ability to respond quickly to load variations prove essential for ensuring stable and resilient energy supply[2].

The advantages of RFBs extend beyond their scalability and modularity. They include:

- Long Cycle Life: RFBs can undergo thousands of charge-discharge cycles with minimal degradation, making them ideal for applications with frequent cycles over many years.

- Safety and Reliability: The risk of thermal runaway is significantly reduced in RFBs due to the physical separation of energy storage components, enhancing operational safety. Additionally, the aqueous nature of most RFB electrolytes further reduces the risk of fire.

- Environmental Sustainability: RFBs often use materials that are less harmful to the environment compared to the metals used in conventional batteries. Moreover, the ability to recycle and reuse the electrolyte solutions contributes to their sustainability profile.

- Flexibility in Application: The independent scaling of power and energy capacities allows RFBs to be tailored to a wide range of applications, from stabilizing renewable energy outputs to providing backup power and grid services.

1.1.3. Principles of Redox Flow Batteries

Flow batteries consist of two electrolyte solutions stored in separate tanks: one with a positive redox couple and the other with a negative redox couple. These redox couples are usually dissolved in electrolyte solution which flow through the system's electrochemical cell during operation.

The electrochemical cell, where energy conversion occurs, is comprised of two half-cells separated by a membrane. Each half-cell contains an electrode and is associated with one of the electrolyte solutions.

In the cell the redox reactions take place. During discharge, electrons are released from the oxidation half-reaction at the anode, providing electrical power, while at the cathode, the reduction half-reaction accepts electrons. This process is reversed during charging.

The spatial separation between the electrolyte tanks and the electrodes in the cell allow to decouple the energy and power of the Redox Flow Battery. This flexibility in the design of the flow battery allow to more easily match the request of the energy storage system with the development of the battery.

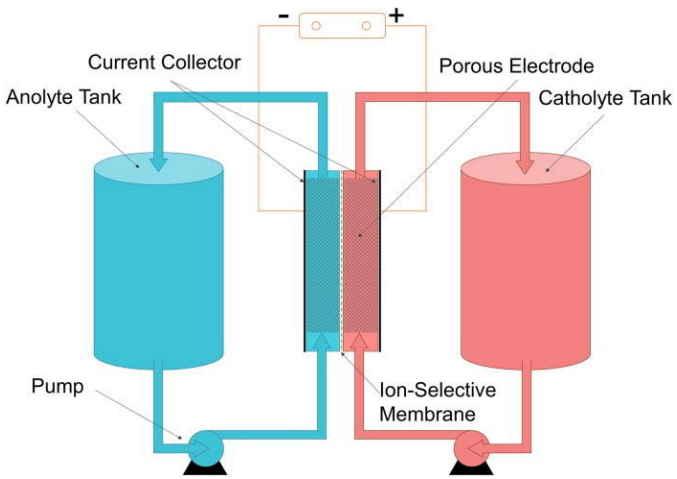

Figure 1.1.2 – Simple scheme of a flow battery where is possible to distinguish the two separate tanks and the cell. [3]

1.1.4. Types of Redox Flow Battery

Flow batteries encompass a diverse range of chemistries, each tailored to specific applications and operational requirements. These incudes:

- **Vanadium Redox Flow Batteries (VRFB):** VRFBs use vanadium ions in different oxidation states (V^{2+}/V^{3+} and V^{4+}/V^{5+}) as the two electrolytes. They are known for their long cycle life, high efficiency, and scalability. VRFBs are considered one of the most mature and commercially viable flow battery technologies.

- **Zinc-Bromine Flow Batteries (ZBB):** Zinc and bromine are used as the active materials in the electrolytes. During charging, zinc is plated on the anode, and bromine is reduced to form bromide ions at the cathode. ZBBs are known for their high energy density and low cost.

- **Iron-Chromium Flow Batteries (ICFB**): ICFBs use iron and chromium in different oxidation states (Fe^{2+}/Fe^{3+} and Cr^{2+}/Cr^{3+}) as the active materials in the electrolytes. They offer good energy density and have the potential for cost-effectiveness. However, challenges include corrosion and crossover of ions between the electrolytes.

- **Organic Redox Flow Batteries (ORFB):** ORFBs use organic molecules as the active materials in the electrolytes. Examples include quinones, which can undergo reversible redox reactions. Organic molecules can be designed and synthesized with specific properties, potentially offering a wide range of

electrochemical characteristics. ORFBs are being researched for their sustainability and environmental friendliness.

- **Hybrid Flow Batteries**: Hybrid flow batteries combine features of different flow battery chemistries to leverage their respective advantages. For example, they may use a solid-state cathode combined with a liquid anode. Hybrid flow batteries aim to address specific challenges of individual chemistries and improve overall performance, efficiency, and cost-effectiveness.

Each type of flow battery has its own set of advantages and challenges, and the choice of a particular technology depends on the specific requirements of the application, such as energy density, scalability, cost, and cycle life.

In Table 1.1 are reported the major characteristics of different types of redox flow batteries beyond the chemistry just presented.

Active Species	Cell Voltage (V)	Power Density (W/m^2)	Energy Density (Wh/L)	Lifetime (Cycles)
Chromium-iron	1.07	200	30	1000
Iron-iron	1.21	500	20	10 000
Organic–ferrocyanide	1.62	2000	21.7	75
Organic–bromine	2.13	3000	35	10
Sulfonate viologen	0.9	500	10	1000
VRFB	1.4	800	25	20 000
Zinc–bromine	1.85	1000	75	2000

Table 1.1 – Overview of the most common types of redox flow batteries. [4]

1.1.5. All Vanadium Redox Flow Batteries

Vanadium Redox Flow Batteries (VRFBs) represent a prominent category within the realm of flow battery technologies, offering distinctive features that make them particularly suitable for various energy storage applications.

VRFBs operate based on the redox reactions of vanadium ions in different oxidation states (V^{2+}/V^{3+} and V^{4+}/V^{5+}, Figure 1.1.3) as the active materials in the electrolytes [5]. The electrolytes, containing vanadium ions, are stored in separate tanks, and the electrochemical reactions occur when these electrolytes are circulated through the cell stack during charge and discharge processes.

Vanadium chemistry offers a broad set of advantages compared to the other RFBs. The four states of oxidation of the Vanadium allows to have high life cycle of the battery compared other chemistry. This is related mostly to the crossover phenomenon which in the case of Vanadium is associated only at a self-discharge of the battery and not to a contamination of the electrolyte. Furthermore, the reaction phases remains the same without deposition of reactants at the electrodes which can led to dendrites growth or loss of performances.

VRFBs exhibit high energy efficiency, with typical values ranging between 70-80%. This efficiency is attributable to the symmetrical nature of the vanadium redox couples, which minimizes energy losses during the conversion processes. The near-identical charge and discharge voltage curves of VRFBs reduce overpotential losses, further enhancing their efficiency.

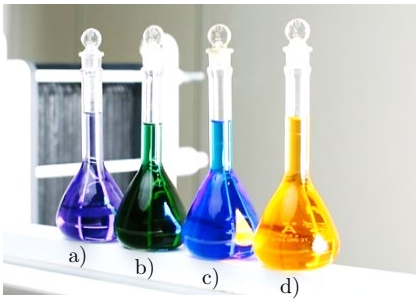

Figure 1.1.3 – The fourth oxidation states of Vanadium: a) V^{2+} b) V^{3+} c) VO^{2+} d) VO_2^{+}

The modular design of VRFBs allows for excellent scalability, making them adaptable to a wide range of energy storage capacities. Moreover, VRFBs exhibit high energy efficiency in converting chemical energy to electrical energy and vice versa, contributing to their suitability for long-duration applications [2]. They have also demonstrated robust performance, maintaining their efficiency and capacity over a large number of charge and discharge cycles.

VRFBs find extensive applications in stationary energy storage, especially in scenarios requiring grid-level storage and integration of renewable energy sources. Their ability to provide reliable and stable power output over extended periods makes them valuable for smoothing out fluctuations in renewable energy generation.

Despite their advantages, VRFBs face challenges, including a relatively lower energy density compared to some other battery technologies. The cost of vanadium, a critical component in the electrolyte, can impact the overall economic viability of VRFBs.

Ongoing research and development efforts focus on improving the energy density, reducing costs, and addressing challenges associated with VRFBs. Also, innovations in membrane technology and electrode materials aim to enhance overall performance and competitiveness in the energy storage market.

Concerning this, the modeling plays a crucial role in the improvement and optimization of Vanadium Redox Flow Batteries (VRFBs). The use of mathematical and computational models allows researchers and engineers to simulate and analyze various aspects of VRFBs, leading to a better understanding of their behavior and performance.

Chapter 2

Principles of Flow Battery Model

This chapter is focused on the built of a basic flow battery model, breaking down the science behind flow batteries, focusing on the Vanadium Redox Flow Battery (VRFB). The chapter explains the main ideas and math needed to understand how these batteries work, understanding the thermodynamic, reaction kinetics, charge, and mass transport phenomenon, with reference to [6]. The goal of the chapter is to identify the most important aspect who influence and describe the behavior and performances of the battery.

2.1. Thermodynamics Principles for VRFB

2.1.1. Flow Batteries Thermodynamic Principles

The thermodynamics of flow batteries, provides an understanding of the energy transformations that occur within these systems, and then the efficiency correlated to these processes.

The final goal of the batteries regards the capacity of storage the energy in the more efficient way. To understand how the electrical energy can be stored and the re-used, it is necessary to derive the maximum amount of electrical work which is possible to extract from the cell reaction. This operation starts from the definition of the Gibbs free energy that represents the exploitable energy potential, of the system. By definition, the Gibbs free energy is:

$$G = U - TS + pV = H - TS \tag{2.1.1}$$

where U represent the internal energy, T the temperature and S the entropy of the system.

By the definition of H, U and dU:

$$H = U + pV \tag{2.1.2}$$

$$U = U(S, V) \tag{2.1.3}$$

$$dU = TdS - dW = TdS - (pdV + dW_{elec}) \tag{2.1.45}$$

it is possible to derive an equation for the variation of G:

$$dG = dU - TdS - SdT + pdV + Vdp = -SdT + Vdp - dW_{elec} \tag{2.1.56}$$

For a constant temperature and pressure system, as attended in the battery's cell this reduces to:

$$dG = -dW_{elec} \tag{2.1.6}$$

Thus, the maximum electrical work that a system can perform in a constant-temperature, constant-pressure process is given by the negative of the Gibbs free-energy difference for the process[6]. For a reaction using molar quantities, this equation can be written as:

$$W_{elec} = \Delta\hat{g}_{rxn} \tag{2.1.7}$$

where $\Delta\hat{g}_{rxn}$ indicates the variation on the Gibbs free energy of a reaction on molar basis (values which can be calculated from some tabulated value of g).

Because the electrical work is defined as:

$$W_{elec} = EQ \tag{2.1.8}$$

with E the electrical field and Q the charge, and Q:

$$Q = nF \tag{2.1.9}$$

with n the number of moles of charged particles (electrons) and F the Faraday's constant, the potential electrical work could be also written as:

$$\Delta\hat{g} = -nFE \tag{2.1.10}$$

Thus, the Gibbs free energy sets the magnitude of the reversible voltage for an electrochemical reaction. This is fixed, cannot be varies for a specific reaction and so

represent one of the more important aspects for the choose of the electrolyte solution in a redox flow battery.

It is possible to demonstrate how these electrochemical potential changes with temperature, pressure, and chemical composition.

Concerning the cell of a flow battery, variation due to temperature and pressure can be considered almost negligible. Differently occur with the concentration. To understand how the reversible voltage change with concentration, it is necessary to introduce the concept of chemical potential. Chemical potential measures how the Gibbs free energy of a system changes as the chemistry of the system changes. This is defined as:

$$\mu_i^{\alpha} = \left(\frac{\partial G}{\partial n_i}\right)_{T,p,n_{j\neq i}} \tag{2.1.11}$$

where $\mu\alpha_i$ is the chemical potential of species i in phase α and $(\partial G/\partial n_i)_{T,p,n_{j\neq i}}$ expresses how much the Gibbs free energy of the system changes for an infinitesimal increase in the quantity of species i. Chemical potential is related to concentration through activity a:

$$\mu_i = \mu_i^0 + RT\, ln\, a_i \tag{2.1.12}$$

where μ_i^0 is the reference chemical potential of species i at standard-state conditions and a_i is the activity of species i. The activity of a species depends on its chemical nature, so for example:

- Ideal solution: $a_i = c_i \,/\, c^0$, where c_i is the molar concentration of the species and c^0 is the standard-state concentration (1 M = 1 mol/L).
- Non-ideal solution: $a_i = \gamma(c_i/c^0)$ where γ is used to describe the departure from ideality.
- Pure components: $a_i = 1$

The variation in the Gibbs free energy becomes:

$$dG = \sum_i \mu_i dn_i = \sum_i (\mu_i^0 + RT\, ln\, a_i)\; dn_i \tag{2.1.13}$$

From the property of logarithm and recognizing that the standard-state chemical potential terms represent the standard-state molar free-energy change for the reaction, $\Delta\hat{g}^0$, the equation can be simplified to a final form:

$$\Delta\hat{g} = \Delta\hat{g}^0 + RT\,ln\frac{\prod a_{products}^{v_i}}{\prod a_{reactants}^{v_i}} \tag{2.1.14}$$

Having defined also the free Gibbs energy as $\Delta\hat{g} = -nFE$:

$$E = E^0 + \frac{RT}{nF}\,ln\frac{\prod a_{products}^{v_i}}{\prod a_{reactants}^{v_i}} \tag{2.1.15}$$

This equation is known as Nernst equation.

With the Nernst equation it is possible to calculate the Open Circuit Voltage (OCV) of a cell of a RFB in function of the chemistry and their concentration.

2.1.2. Efficiency of Flow Battery

The efficiency of flow batteries is a critical parameter that determines their performance and viability for various applications.

Efficiency in flow batteries can be broadly classified into three categories: Coulombic efficiency, voltage efficiency, and energy efficiency. Each type of efficiency offers insights into different aspects of the battery's performance, from its chemical reaction processes to its overall energy conversion capabilities:

- **Coulombic Efficiency (η_c)**: This measures the effectiveness of the battery in conserving charge during the charge and discharge cycles. It is defined as the ratio of the total charge extracted from the battery to the total charge put into the battery during charging:

$$\eta_c = \frac{\int_0^{t_d} I(t)dt}{\int_0^{t_c} I(t)dt} \tag{2.1.16}$$

  where I is the battery current and t_d, t_c the discharge and charge time respectively. Factors affecting Coulombic efficiency include principally the rate of self-discharge and electrolyte crossover through the membrane.

- **Voltage Efficiency (η_v)**: This efficiency is concerned with the potential losses during the operation of the battery. It is calculated as the ratio of the discharge voltage to the charge voltage:

$$\eta_v = \frac{\frac{1}{t_d}\int_0^{t_d} E(t)dt}{\frac{1}{t_c}\int_0^{t_c} E(t)dt} \tag{2.1.17}$$

where E is the battery voltage. Voltage efficiency is influenced by factors such as the internal resistance of the battery, the kinetics of the electrochemical reactions, and the operational current density.

- **Energy Efficiency (η_e)**: The overall energy efficiency of a flow battery is the product of Coulombic and voltage efficiencies. It represents the proportion of energy put into the battery during charging that can be retrieved during discharge:

$$\eta_e = \eta_c \cdot \eta_v = \frac{\int_0^{t_d} P(t)dt}{\int_0^{t_c} P(t)dt} \tag{2.1.18}$$

where P is the battery power. Energy efficiency is a crucial indicator of the battery's performance for practical applications, as it directly affects the cost and effectiveness of the energy storage system.

The efficiency of flow batteries, especially VRFBs, is a complex interplay of electrochemical, physical, and operational factors. Understanding and optimizing Coulombic, voltage, and energy efficiencies are essential for improving the performance and economic viability of flow battery systems.

2.2. Flow Battery Reactions Kinetics

2.2.1. Electrochemical Reactions in a VRFB

Reaction kinetics in flow batteries describe the rates at which the electrochemical reactions occur at the electrodes. These reactions involve the transfer of electrons between the electrolyte and the electrode surface, a process that is influenced by various factors, including the concentration of reactants, the surface area of the electrodes, and the temperature of the system.

The conversion of reactants into products becomes after the overcome of an activation barrier, i.e., the energy required to initiate the electrochemical reactions. The characterization of the activation barrier derives from the study of the free energy of the species involved in the reaction.

In a VRFB cell, each step for the reaction from reactants to products is affected by transports and kinetics limits. The reaction, assuming the discharge phase, of a completely charged RFB can be subdivided in four passages at the anode:

1. Mass transport of Vanadium electrolyte (V^{2+}) to the electrode.
2. Absorption of V^{2+} onto the electrode surface (inner-sphere mechanism).
3. Transfer of electron from chemisorbed Vanadium to the electrode.
4. Mass transport of V^{3+} ions away from electrode.

The semi-reaction at the anode takes the form:

$$V^{2+} \rightarrow V^{3+} + e^{-} \tag{2.2.1}$$

During the reaction a proton of H^{+} pass trough a proton-exchange membrane to the cathode side, or conversely a negative ion can flow in the reverse direction thought an anion-exchange membrane. It is easily to recognize how the concentration of V^{3+} ions increase in the electrolyte solution with the progress of discharge, conversely it will increase during the charge.

Similarly, at the cathode, the reaction follows the passages:

1. Mass transport of Vanadium electrolyte $VO_2^{-}, (V^{5+} + 2O_2^{-})$ to the electrode.
2. Transfer of electron from the electrode to VO_2^{-} trough collision with electrode (outer sphere mechanism).
3. Formation of VO^{2+} and H_2O.
4. Mass transport of VO^{2+} and H_2O away from electrode.

The semi-reaction at the cathode during discharge takes the form:

$$VO_2^{-} + 2H^{+} + e^{-} \rightarrow VO^{2+} + H_2O \tag{2.2.2}$$

All these passages involved a change into free energy of the elements, function of the distance from interface.

However, in literature there are different and inconsistency theory in the reaction mechanism which could be partly due to differences in the analysis system (surface structures and interfacial environments of the working electrode for these analyses can vary due to the difference in carbon material, cell configuration, and flowing conditions).

The process of adsorption and desorption, which includes the reorganization of a solvated structure, demands high activation energy for inner-sphere electron transfers, leading to a higher charge transfer resistance when compared to outer-sphere electron transfers. This difference can be attributed to the fact that V^{2+} and V^{3+} ions are encased in a rigid hydration shell due to strong ion-dipole interactions, in contrast to

VO_2^+ ions, which possess a more loosely structured hydration shell. The well-organized hydration shell acts as an impediment to electron transfer between the carbon felt (CF) and the vanadium ion, making direct electron transfer through this dense shell challenging for V2+ and V3+ ions. Thus, the presence of an OH functional group, which facilitates the breaking of the hydration shell and secures the vanadium ions to the electrode surface, is crucial for reducing the activation energy needed for electron transfer. On the other hand, for VO2+ ions, the disorganized nature of their hydration shell allows for the direct interaction of the vanadium ions with the electrode surface upon contact, permitting electron transfer to occur without needing the OH functional group's assistance [7].

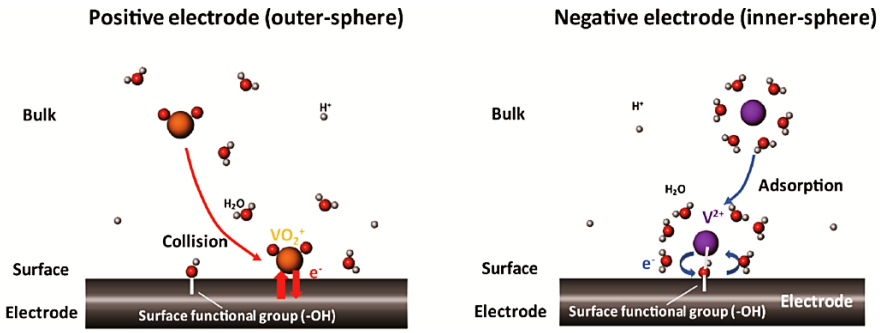

Figure 2.2.1- Inner-sphere and Outer-sphere mechanism [7].

It is possible to assume that the first three steps are energetically favorable near the interface and then ions after the reactions tend to be transport away from the surface. There will be a distance a where the reactions take place in the most favorable condition. The distance a identify the activated state of the reactions. Only species in the activated state can undergo the transition from reactant to product. The rate of reaction is then determinate by the probability for the species to be at the activated state.

The probability of finding a species in the activated state is exponentially dependent on the size of the activation barrier:

$$P_{act} = exp\left(-\frac{\Delta G_1^*}{RT}\right) \tag{2.2.3}$$

where P_{act} is the probability of finding a reactant species in the activated state, ΔG_1^* is the size of the energy barrier between the reactant and activated states, R is the gas constant, and T is the temperature.

2.2.2. The Butler-Volmer Equation

The rate at which the reactants are transformed into product in an electrochemical reaction is defined reaction rate. It is possible to define the net reaction rate J as the difference between the forward and the reverse reactions rate:

$$J = J_1 - J_2 \tag{2.2.4}$$

In general, $J_1 \gg J_2$ which holds $\Delta G_1^* \ll \Delta G_2^*$. Considering then the reactant surface concentration c_R^s and the decay rate to product f_1 (lifetime of the activated species and the likelihood that it will convert to a product instead of back to a reactant):

$$J = c_R^s f_1 P_{act_1} - c_P^s f_2 P_{act_2} \tag{2.2.5}$$

Expressing this reaction rate in function to the current density j ($j = \frac{J}{Area}$):

$$j = nFJ = nF\left(c_R^s f_1 e^{\left(-\frac{\Delta G_1^*}{RT}\right)} - c_P^s f_2 e^{\left(-\frac{\Delta G_2^*}{RT}\right)}\right) \tag{2.2.6}$$

Generally, it is expected that the forward reaction j_1 will be favorable than the reverse reaction j_2. However, these unequal rates quickly result in a buildup of charge, with e^- accumulating in the metal electrode and V^{3+} accumulating in the electrolyte. The charge accumulation continues until the resultant potential difference $\Delta\phi$ across the reaction interface exactly counterbalances the chemical free-energy difference between the reactant and product states ($\Delta G_{rxn} = -\, nF\Delta\phi$):

$$j_2 = nFc_P^s f_2 e^{\left(-\frac{\Delta G_2^*}{RT} - nF\Delta\phi\right)} \tag{2.2.7}$$

Thus:

$$j_1 = j_2 = j_0 \tag{2.2.8}$$

The build-up potential equalizes the situation increasing the activation barrier for forward reaction and decreasing the activation barrier for reverse reaction. This electrical potential across the anode and the cathode is known as Galvani potential.

The Galvani potential at the anode and the cathode must both be reduced in order to extract a net current from a cell. Decreasing the Galvani potential reduce the forward activation barrier increasing the reverse activation barrier as shown in Figure 2.2.2.

To quantify the reduction is introduced the coefficient α, called transfer coefficient. Reducing of the quantity η the Galvani potential, the total forward activation barrier is reduced of $\alpha nF\eta$, while the reverse activation barrier of $(1-\alpha)nF\eta$.

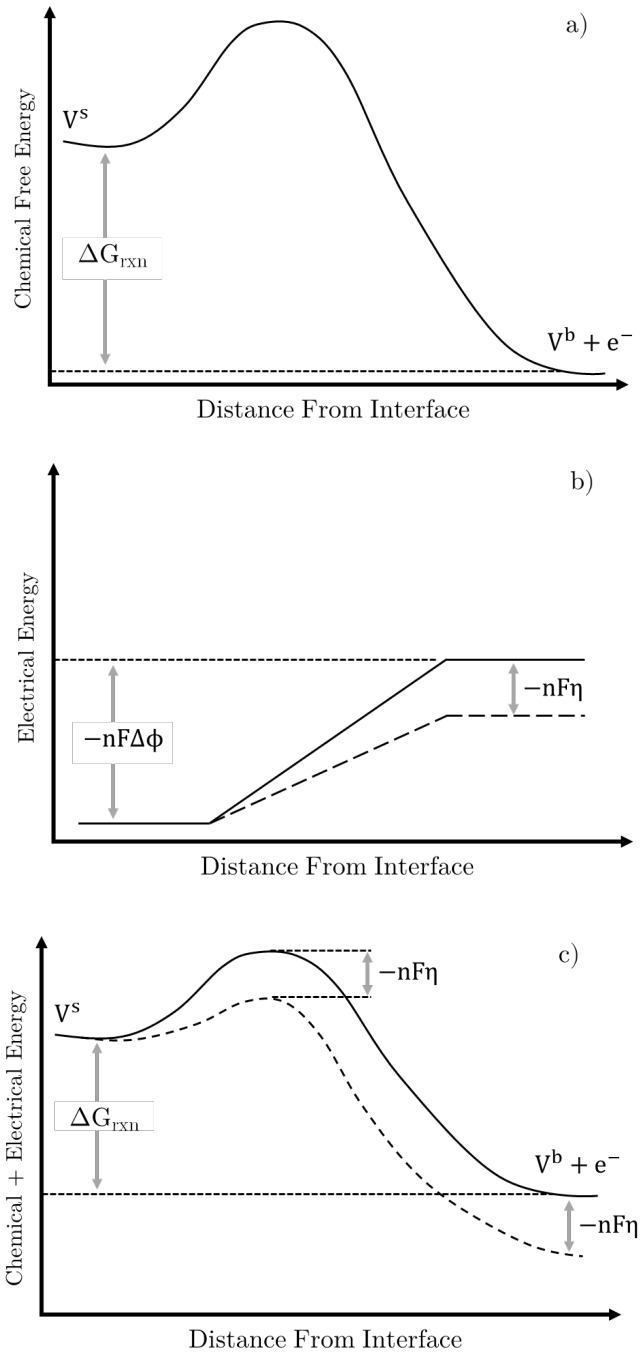

Figure 2.2.2 - The chemical energy (a) of the reaction system remains constant, but changing the electrical potential (b) upsets the balance between the forward and reverse activation barriers (c). Decreasing the Galvani potential reduce the forward activation barrier increasing the reverse activation barrier. In the figure, V^s indicates the Vanadium concentration at the surface, V^b the Vanadium concentration at the bulk (away from the electrode surface).

Away from the equilibrium, the net current, assuming the concentration of reactants and products not affected by the presence of a net reaction rate, will be then:

$$j = j_1 - j_2 = j_0 \left(e^{\frac{\alpha n F \eta}{RT}} - e^{-\frac{(1-\alpha) n F \eta}{RT}} \right) \tag{2.2.9}$$

The coefficient coefficients α and $(1-\alpha)$ are obtained usually by fitting experimental data[8].

The equation 2.2.9 is known as Butler-Volmer equation. The Butler–Volmer equation generally serves as an excellent approximation for most single-step electrochemical reactions.

From the Butler–Volmer equation it is possible to recognize as the current produced by an electrochemical reaction increases exponentially with activation overvoltage, η_{act} representing voltage which is lost to overcome the activation barrier associated with the electrochemical reaction. In other words, the Butler–Volmer equation explicate how much is the price to pay in terms of voltage if the current request increase.

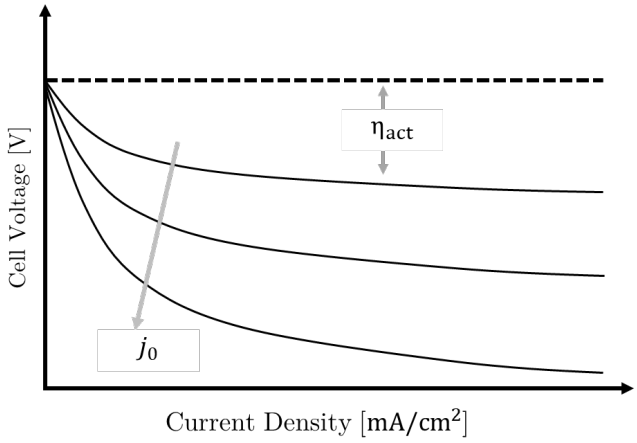

Figure 2.2.3 - Activation overvoltage losses trend.

Activation overvoltage losses are minimized by maximizing j_0. There are four major ways to increase j_0 [6]:

1) increase reactant concentration;
2) increase reaction temperature;
3) decrease the activation barrier (by employing a catalyst);
4) increase the number of reaction sites (by fabricating high-surface-area electrodes and 3D structured reaction interfaces).

To increase j_0, RFB's catalyst–electrodes are designed to maximize the number of reaction sites per unit area. The best catalyst–electrodes are carefully optimized, porous, high-surface-area structures.

A complete Butler-Volmer equation can be derived from equation 2.2.6 also considering the effects of concentration of reactants, obtaining:

$$j = j_0^0 \left(\frac{c_R^s}{c_R^{0*}} e^{\frac{\alpha n F \eta_{act}}{RT}} - \frac{c_P^s}{c_P^{0*}} e^{\frac{(1-\alpha) n F \eta_{act}}{RT}} \right) \tag{2.2.10}$$

where c_R^{0*}, c_P^{0*} indicates a reference reactants or products concentrations. This reference concentration can be the bulk concentration of the product or reactants, i.e. the concentration away from the electrodes. The evaluation of this quantity will be derived in the next chapter.

2.3. Transport Mechanisms

2.3.1. Charge Transport

In an electrochemical cell the charge transport plays a fundamental role, moving the charges from the electrode where they are collected to the electrode where they are "consumed".

Both electrons and ions must be transported in the cell. Resistance to charge transport results in a voltage loss for the cells, an ohmic loss. Ohmic losses are minimized by making the membrane as thin as possible and employing high-conductivity materials.

There are three major driving forces that give rise to charge transport:

- electrical driving forces (as represented by an electrical potential gradient dV/dx);
- chemical driving forces (as represented by a chemical potential gradient $d\mu/dx$);
- mechanical driving forces (as represented by a pressure gradient dP/dx).

In the VRFB's cell, the accumulation/depletion of electrons at the two electrodes creates a voltage gradient, which drives the transport of electrons from the anode to the cathode. In the electrolyte, accumulation/depletion of protons creates both a voltage gradient and a concentration gradient. These coupled gradients then drive the transport of protons from the anode to the cathode.

Generally the major driving force result in the electrical driving force (electrical potential gradient). For this, it is easy to quantify the voltage loss through the Ohm's law:

$$V = j\left(\frac{L}{\sigma}\right) = i\left(\frac{L}{A\sigma}\right) = iR \tag{2.3.1}$$

where σ is the conductivity and R the resistance of the conductor.

While the electronic current involves the movement of electrons through conductive materials such as metals (in the VRFB's contest the electrodes and the external circuit), ionic currents involve the movement of charged species (ions) within the electrolyte solution. Despite the same driving force (dV/dx) govern the two mechanisms, completely different resistance terms control the transport.

For the electrons, the electrode material is generally the only cause of the resistance, so σ is only dependent by the electrode itself. Conversely, for the ionic transport, several parameters play a fundamental role.

In the metal electrodes, only a voltage gradient drives electron charge transport. However, in the electrolyte, both a concentration (chemical potential) gradient and a voltage (electrical potential) gradient drive ion transport.

A material's conductivity is influenced by two major factors: how many carriers are available to transport charge and the mobility of those carriers within the material. The following equation defines σ in those terms:

$$\sigma_i = z_i F\ c_i \mu_i \tag{2.3.2}$$

where c_i represents the molar concentration of charge carriers are available per unit volume (unitary value for a solid as the electrode) and μ_i is the mobility of the charge carriers within the material.

The complete expression for conductivity combines carrier concentration and carrier mobility is provided by the Nernst Einstein relation:

$$\mu_{m,i} = \frac{D_i}{RT} \tag{2.3.3}$$

$$\sigma = \frac{F^2}{RT} z_i^2 c_i\ D_i \tag{2.3.4}$$

The ionic flux considering only the electrical driving force can be derived from the Farady law:

$$J = \sigma \ \nabla\phi_l = z_i F \cdot N_i \tag{2.3.5}$$

where N_i is the ionic flux:

$$N_i = \frac{F}{RT} z_i c_i \ D_i \ \nabla\phi_l \tag{2.3.6}$$

Considering also the chemical driving force:

$$N_i = \frac{F}{RT} z_i c_i \ D_i \ \nabla\phi_l + D_i \nabla c_i \tag{2.3.7}$$

Adding the mechanical driving force (advection):

$$N_i = \frac{F}{RT} z_i c_i \ D_i \ \nabla\phi_l + D_i \nabla c_i + c_i \ u \tag{2.3.8}$$

The last equation obtained is the Nernst-Planck equation who describe the molar flux ($\mathrm{mol/m^2 s}$), direct correlated to the ionic current ($\mathrm{A/m^2}$), through the physical quantity $z_i F$.

Generally, the ionic contribution to R tends to dominate the charge transport but this strongly depends on the cell configuration. Indeed, the porose electrode nature reduce the mobility of the electrons in the electrode as well as the diffusivity of the ions in the electrolyte. These reductions are often corrected with some empirical correlations as the Bruggeman corrections [4]. For the electrode conductivity:

$$\sigma^{eff} = \sigma^0 (1 - \varepsilon)^{1.5} \tag{2.3.9}$$

where σ^{eff} is the effective conductivity of the porose electrode and σ^0 the nominal electrode conductivity and ε the porosity of the compressed electrode.

For the electrolyte species:

$$D^{eff} = D^0 \ \varepsilon^{1.5} \tag{2.3.10}$$

where D^{eff} is the effective diffusion coefficient of the species in the porose electrode and D^0 the diffusion coefficient in the free electrolyte (often associated with the limit diffusion coefficient).

The Bruggeman's corrections shown how the increase of electrode conductivity increase for an increase of electrode compression, while the ionic diffusivity decreases as well. From a charge transport point of view, for an efficient VRFB design there will be searched for a trade-off between these two trends in order to find the optimum electrode compression.

2.3.2. Mass Transport

In the context of Vanadium Redox Flow Batteries (VRFBs), the efficiency with which reactants are delivered to and products are removed from the reaction sites is known as mass transport. Inadequate mass transport can lead to considerable performance degradation in VRFBs, as the battery's output is closely linked to the concentrations of reactants and products within the electrode layers.

Mass transport challenges within VRFBs can be categorized into problems that occur at different scales: within the electrodes and within the flow structure of the battery. The flow structure, characterized by well-defined channels through which the electrolyte flows, is governed by the principles of fluid mechanics. Here, transport is primarily driven by fluid flow and convection. Conversely, the electrodes, with their micro and nanometer-scale porosity and structure, present a different set of transport phenomena.

In the flow structures (outside from the electrodes) the electrochemical reaction doesn't takes place, so only fluid dynamics losses are relevant for the final battery performance, but not for the electrochemical cell performance, if not for the flow channel ability to guarantee fresh reactants in an homogeneous way in he electrode.

By assuming the electrode's fibers thickness is equivalent to the diffusion layer thickness, it's possible to examine the transport phenomena occurring within the electrode. At the point of the electrochemical reaction, the depletion of reactants leads to a decrease in performance for two primary reasons:

- Nernstian Losses: As the concentration of reactants at the reaction site drops, the reversible voltage of the VRFB, as dictated by the Nernst equation, decreases.
- Reaction Losses: The decrease in reactant concentration at the catalyst layer, relative to the bulk concentration, results in increased reaction (or activation) losses.

Together, these effects contribute to what is known in the VRFB as concentration (or mass transport) losses, highlighting the critical role of efficient mass transport in maintaining optimal battery performance.

The flux of reactants (or products) is determined by the equation:

$$J_{diff} = -D\frac{dc}{dx} \tag{2.3.11}$$

where D is the diffusion coefficient and c the species concentrations. For a steady state situation:

$$J_{diff} = D^{eff}\frac{c^s - c^b}{\delta} \tag{2.3.12}$$

where c^s is the catalyst layer reactant concentration, c^{b} is the bulk reactant concentration, δ is the electrode (diffusion layer) thickness, and D^{eff} is the effective reactant diffusivity within the catalyst layer. Because of:

$$j = nFJ_{diff} \tag{2.3.13}$$

the reactants concentration in the catalyst layer:

$$c^s = c^b - \frac{j\delta}{nFD^{eff}} \tag{2.3.14}$$

The equation 2.3.14 indicates how the reactant concentration in the catalyst layer is less than the bulk concentration by an amount that depends on j, δ, and D^{eff}. As j increases, the reactant depletion effect intensifies. Thus, the higher the current density, the worse the concentration losses.

The parameters δ and D^{eff} are difficult to evaluate for this, empirical correlation relate the catalyst layer concentration (also indicated as the surface concentration) with a parameter $\mathrm{k_m}$ defined "mass transfer coefficient":

$$c^s = c^b - \frac{j}{nF\ k_m} \tag{2.3.15}$$

The mass transfer coefficient is related in general to the macroscopic velocity within the porose electrode (u) with two empirical coefficients, a and b, so that:

$$k_m = a\ |u|^b \tag{2.3.16}$$

Recalling the Nernst equation, it is possible to derive the reduction of the E, η_{nernst} due to different concentration level of the reactants:

$$\eta_{nernst} = \frac{RT}{nF} ln \frac{c^b}{c^s} \tag{2.3.17}$$

The ratio c^b/c^s, can be transformed explicating the terms, introducing the limiting current voltage j_L, the current at which the reaction can't be sustained because the reactants drop to zero ($c^s = 0$), obtaining:

$$\eta_{nernst} = \frac{RT}{nF} ln \frac{j_L}{j_L - j} \tag{2.3.18}$$

Concerning the way how concentration affects the reaction rate, is recalled the Butler-Volmer equation (equation 2.2.10):

$$j = j_0^0 \left(\frac{c_R^s}{c_R^{0*}} e^{\frac{\alpha n F \eta_{act}}{RT}} - \frac{c_P^s}{c_P^{0*}} e^{\frac{(1-\alpha) n F \eta_{act}}{RT}} \right) \tag{2.3.19}$$

It is possible calculate how the concentration c^s changes the overvoltage over c^b:

$$\eta_{conc,BV} = \eta_{act}^* - \eta_{act}^0 = \frac{RT}{\alpha nF} ln \frac{c^b}{c^s} \tag{2.3.20}$$

So, the effect of Nernst equation and Butler-Volmer equation can be summed and the total concentration loss results:

$$\eta_{conc} = \eta_{Nernst} + \eta_{BV} = \left(\frac{RT}{nF} \right) \left(1 - \frac{1}{\alpha} \right) ln \frac{j_L}{j_L - j} \tag{2.3.21}$$

Totally, the concentration loss due to Nernstian effect modify the $j - V$ curve as report in Figure 2.3.1.

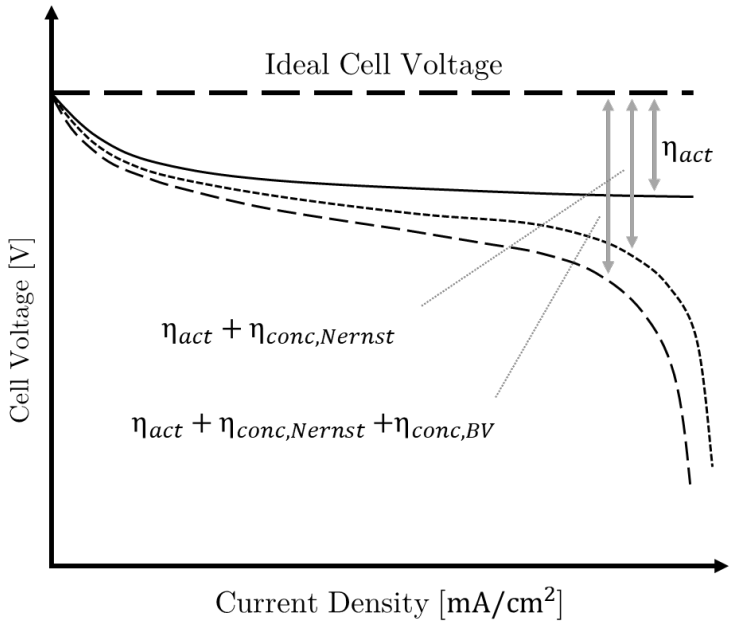

Figure 2.3.1 - Concentration losses due to concentration effects and activation effects.

2.4. Basic Flow Battery Model

2.4.1. Overpotentials Contributions

How much described in the previous chapters allow to have a broad overview about the major factors influencing the electrochemical performances in the VRFB cell. The different overpotentials contributions can be summarized as follow:

- Activation Overpotential: This is associated with the energy barrier that must be overcome to initiate the electrochemical reactions at the electrodes. It is influenced by the reaction kinetics and the surface properties of the electrodes.
- Ohmic Overpotential: This results from the resistance to ion and electron flow within the electrolyte, membrane, and electrode materials. It is affected by the conductivity of these components and the design of the battery.
- Concentration Overpotential: Caused by the difference in reactant concentration at the electrode surface compared to the bulk solution. It occurs when the rate of electrochemical reaction is fast enough that mass transport (diffusion and convection) cannot replenish the reactants quickly enough, leading to a depletion of reactants at the electrode surface.

The final voltage of the cell of the flow battery is affected by several losses:

$$V = E_{therm} - \eta_{act} - \eta_{ohmic} - \eta_{conc} \tag{2.4.1}$$

The result of these losses can be shown in Figure 2.4.1 and it is known as polarization curve of the flow battery.

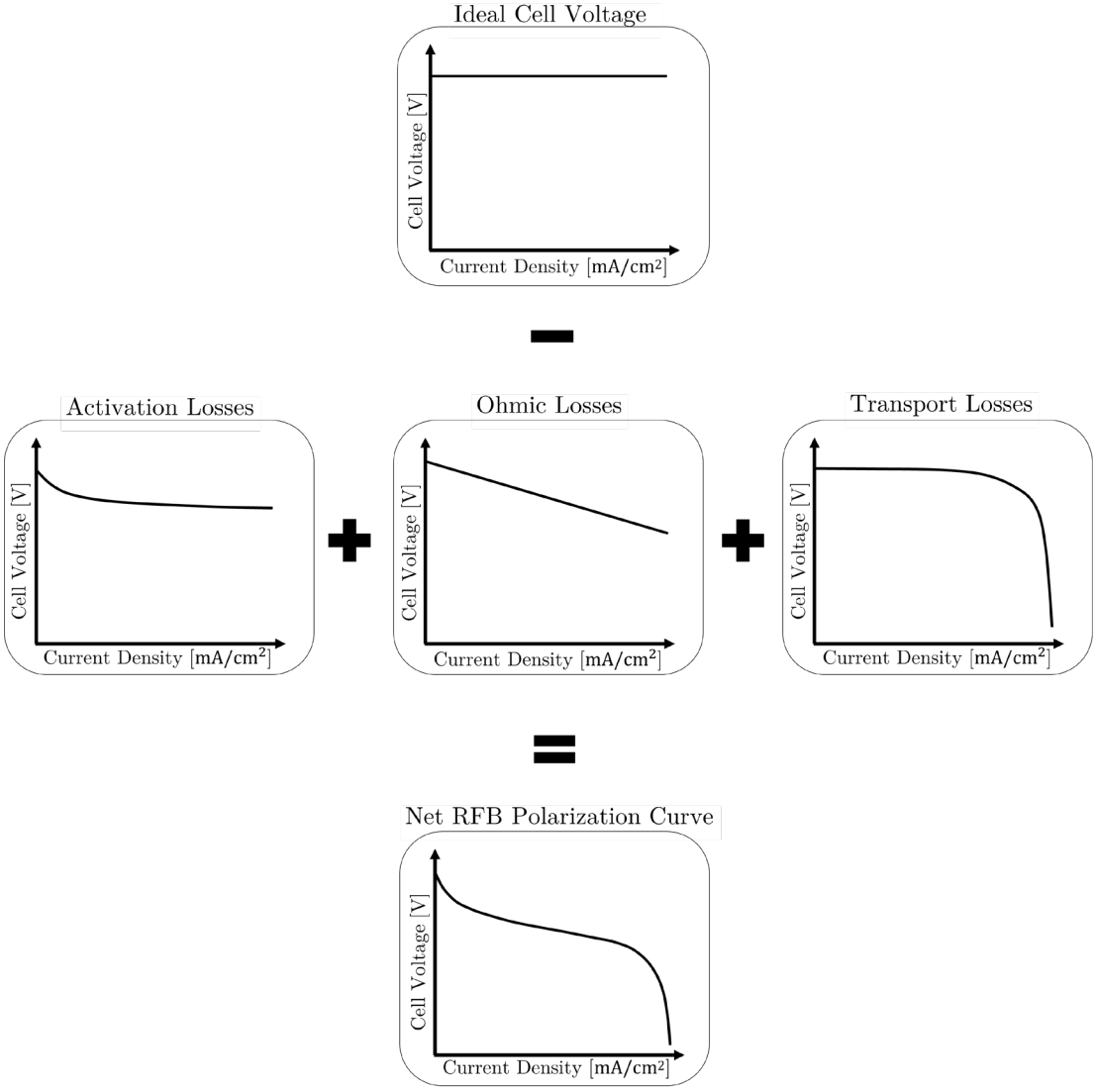

Figure 2.4.1 - Summary of major factors that contribute to the RFB polarization curve. To the ideal cell voltage are subtracted the activation losses, the ohmic losses and the concentration losses to obtain the net RFB polarization curve.

The polarization curve of the battery is one of the most important aspect who characterize the battery itself, giving an overview on the major losses aspects. To accurately reflect the behavior of most cells, an additional loss term, known as the leakage loss j_{leak}, must be introduced.

The leakage loss j_{leak} is associated with the parasitic loss due to current leakage, gas crossover, unwanted side reaction, and so on. The net effect of this parasitic current loss is to offset a cell's operating current to the left by an amount given by j_{leak}. This has the effect of reducing a cell's open-circuit voltage below the thermodynamically predicted value [6].

The polarization curve is a powerful tool for visualizing the combined effects of various overpotentials in a VRFB. By analyzing this curve, researchers and engineers can identify the dominant factors limiting battery performance at different operating conditions. This understanding is crucial for developing strategies to minimize overpotentials, such as optimizing electrode design, improving electrolyte conductivity, and enhancing mass transport, ultimately leading to more efficient and effective VRFB systems.

2.4.2. The Multiphysics Model Approach

Starting from the qualitative analysis of overpotentials discussed in the previous chapters, that has permitted the built of the simple model of a redox flow battery, this section outlines the methodology and steps to undertake in creating a comprehensive multiphysics model of a VRFB.

The multiphysics models use numerical methods to simulate the cell behavior. This type of modeling permits detailed investigation and visualization of electrochemical and transport phenomena. It is especially useful when experimental investigation is difficult or impractical and illustrates tremendous promise and power as a redox flow battery design tool.

In the context of advancing the understanding and optimization of Vanadium Redox Flow Batteries (VRFBs), developing a multiphysics model stands out as a crucial methodology. This approach integrates the various physical phenomena, electrochemistry, fluid dynamics, and thermal management, into a cohesive framework:

1) Defining the Model Parameters: The first step in the multiphysics modeling approach involves defining the key parameters that influence VRFB performance. These include:
    a. Electrochemical Properties: Incorporating the activation, concentration, and ohmic overpotentials, alongside reaction kinetics and the Nernst equation, to model the electrochemical reactions accurately.
    b. Fluid Dynamics: Characterizing the flow of electrolyte solutions through the battery system, including the flow rates, viscosity, and pressure

drops, to understand how they impact mass transport and overall battery efficiency.

c. Thermal Properties: Including the heat generated from the electrochemical reactions and the operational environment to assess how temperature variations affect the battery's performance and longevity.

2) Incorporating Material Properties: A critical aspect of multiphysics modeling is the accurate representation of the materials used in the VRFB, including the electrolyte solutions, membrane, and electrodes. Material properties such as conductivity, porosity, and permeability are essential for simulating ion transport, electron flow, and the interactions within the battery system.

3) Developing the Mathematical Framework: With the parameters and material properties defined, the next step involves developing the mathematical equations that describe the behavior of the VRFB under various conditions. This framework should integrate:

   a. Electrochemical Equations: To model the redox reactions and the associated overpotentials.
   b. Fluid dynamics equations: For fluid flow dynamics within the electrolyte channels.
   c. Heat Transfer Equations: To account for thermal effects on battery operation.

4) Simulation and Validation: The mathematical model is then implemented in a computational simulation tool designed for multiphysics analysis. This simulation allows for the visualization and examination of the interactions between electrochemical, fluidic, and thermal phenomena in the VRFB. Validation of the model is crucial and involves comparing the simulation results with experimental data to ensure accuracy and reliability.

Differently from the analytical modelling, where all the overpotentials contribution are derived and explicated in analytical equation, the multiphysics approach discretize the governing equations on small elements in the domains ensuring the congruence between these. This process is performed by solver iterative algorithms which allows to efficiently reach the convergence of the solution. The higher advantages of this approach are the possibility to analyze different complex geometries and to observe in each point of the domains the values of almost all parameters. However, a good analytical knowledge about the physical problem can help to catch not physically acceptable solutions, that can be due to discretization or numerical errors.

Chapter 3

Multiphysics Model of a Vanadium Redox Flow Battery

Chapter 3 embarks on creating a multiphysics model for Vanadium Redox Flow Batteries (VRFBs), inspired by an example available in COMSOL and grounded in literature references. This segment outlines the transition from analyzing an existing COMSOL model, designed to illustrate the general principles of multiphysics simulations, to constructing a novel model tailored to the specific objectives of this research. The process involves a thorough examination of the initial example, identifying key elements and methodologies that are applicable to VRFB systems, and then devising a new model that addresses the unique challenges and questions posed by VRFB technology.

3.1. COMSOL Multiphysics®

COMSOL Multiphysics is a powerful simulation software designed for modeling and solving complex physical phenomena in a wide range of scientific and engineering disciplines. The name COMSOL stands for "COMmunity SOLver," emphasizing its collaborative and customizable nature. It operates on the finite element method, a numerical technique for solving partial differential equations that describe physical processes.

Its extensive features and capabilities make it particularly suited for modeling Vanadium Redox Flow Batteries (VRFBs), offering a comprehensive toolkit for exploring the multifaceted aspects of VRFB systems.

The major key features of COMSOL Multiphysics are:

- Multiphysics Environment: COMSOL's core strength lies in its ability to couple different physics phenomena—electrochemical, fluid dynamics, and thermal management—into a single modeling environment. This is crucial for VRFBs,

where interactions between these phenomena significantly impact battery performance.

- User-friendly Interface: With its intuitive graphical interface and pre-defined physics interfaces, COMSOL simplifies the setup of complex models, making it accessible to users with varying levels of expertise in simulation.
- Customization and Flexibility: COMSOL allows for extensive customization through its physics-based building blocks and equation-based modeling capabilities. Users can tailor models to specific requirements of VRFB systems, including custom reaction kinetics, material properties, and boundary conditions.
- Geometry and Meshing Tools: The software offers advanced tools for creating detailed geometric models of VRFB components and for generating meshes that can resolve complex structures and gradients, essential for accurate simulations.
- Solver and Optimization Capabilities: COMSOL provides robust solver algorithms that can handle the nonlinearities and coupling inherent in VRFB models. Additionally, its optimization tools enable users to refine design parameters for improved battery efficiency and performance.

COMSOL's capabilities are particularly beneficial for modeling the intricate dynamics of VRFBs. It can simulate the electrochemical reactions within the electrodes, the flow of electrolytes through the system, and the thermal effects that arise during operation. By accurately capturing these processes, COMSOL can help in:

- Predicting Battery Performance: Simulating the impact of various operational and design parameters on VRFB efficiency, capacity, and longevity.
- Design Optimization: Identifying optimal configurations of battery components, such as electrode geometry and membrane properties, to enhance overall system performance.
- Investigating Degradation Mechanisms: Understanding the causes of performance degradation over time, including membrane fouling and electrolyte instability, to develop strategies for improving battery durability.
- Evaluating Thermal Management Strategies: Assessing the effectiveness of different cooling and thermal management approaches to maintain battery performance under varying environmental conditions.

COMSOL Multiphysics offers a powerful and versatile platform for the detailed modeling and analysis of VRFB systems. Its comprehensive feature set, coupled with its flexibility and optimization capabilities, makes it an invaluable tool for advancing VRFB technology through simulation-driven insights and design improvements.

3.2. 2D Multiphysics Model

The objective in this chapter is to realize a 2D Simulation of a Single-Cell Vanadium Flow Battery (VFB) in a flow-through cell configuration with an active area of 50 cm2. The model is prone to obtain a polarization curve and to determine the distribution of reactants within the cell.

In the following is explained in detail the fundamental of a 2D model. As starting point is taken as reference the VRFB COMSOL tutorial model, available in the COMSOL open libraries. The tutorial has been created on the base references [9], [10], [11].

3.2.1. Assumptions

The model assumptions are made in order to simplify the first modelling approach. Thus, the main simplifications are:

- Stationary case
- The electrolyte flow is incompressible and laminar because of the small pressure gradient and low flow velocities.
- The evolution of hydrogen and oxygen and the accompanying gas bubble formation in the electrodes are ignored.
- The dilute-solution approximation is used to describe species transport.
- The properties of the electrode, electrolyte, and membrane are assumed to be isotropic.
- The velocity flow field is assumed homogeneous in all electrodes domains.

3.2.2. Geometry of the Cell

The structure of a cell for a flow battery cold be summarized in three different components:

1- Electrode: There are typically two electrodes in each cell, one on each side of the cell stack. The positive electrode (cathode) and negative electrode (anode) facilitate the redox reactions.
2- Ion-Exchange Membrane: Separate the positive and negative electrolyte allowing the passage of H^+ ions (in the case of Cation Exchange Membrane CAEM).
3- Bipolar plates or current collectors: separate adjacent cells within the stack in the case of multiple cells, act as current collectors in the case of a single cell or at the terminal of a stack.

Multiple cells put in series will form a stack, which structure is represented in Figure 3.2.1:

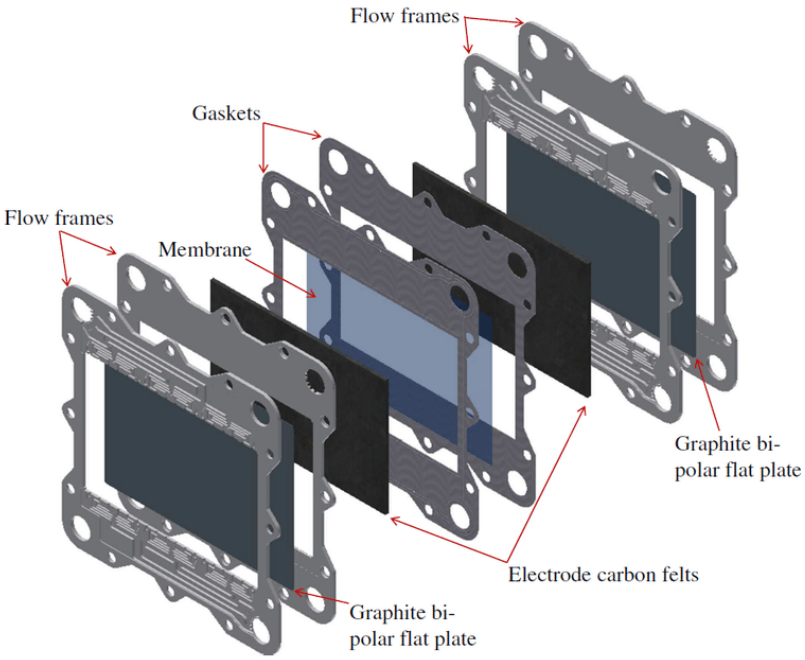

Figure 3.2.1 – Main component of the stack of a RFB in a flow-trough configuration[12]

In literature it is possible to find two major types of cell configuration: Flow-trough configuration and interdigitated. The second one will be explored in the next chapters.

With the flow-through configuration it is possible to assume the flow of reactants entering on the lower part of the cell in a homogeneous mode, excluding the collectors channels and then rise on the top where it is drive to the exit.

With these assumptions it is possible to build a preliminary geometry for the simulation 2D considering (Figure 3.2.2):

- Square plate of $49cm^2$ with a side of $7cm^2$;
- Negative and positive electrode of $3.7mm$ thick;
- Ion-exchange membrane

Each side of the cell is fed with an electrolyte containing sulfuric acid and a vanadium redox couple, flowing through the porous electrodes.

The calculation domain consists of the negative electrode, proton exchange membrane, and positive electrode, as shown in Figure 3.2.2.

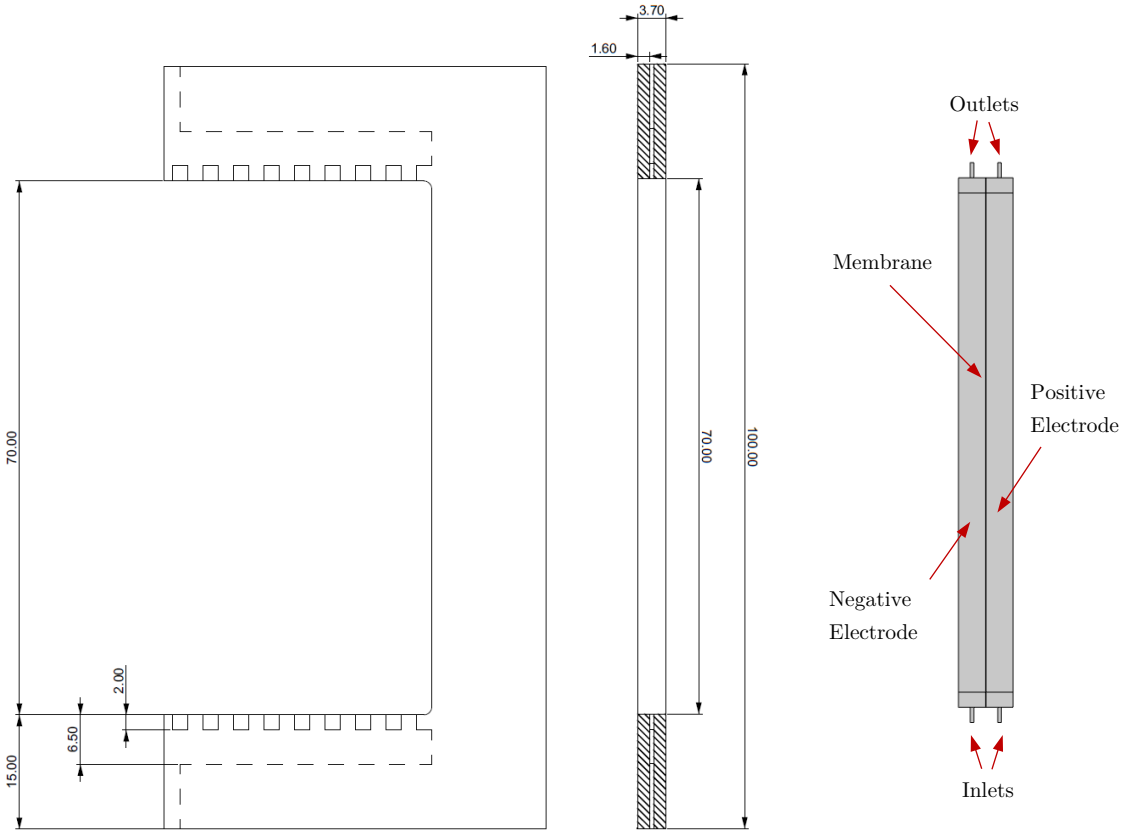

Figure 3.2.2 - Section of the cell used for the model in the left, COMSOL Domains in the right side.

3.2.3. Parameters

The data and the parameters used in the models are reported in Table 3.1. Apart for the Geometry parameters of the cell as the cell height and the cell depth, all the other parameters are maintained that of the tutorial reference. Indeed, the objective now is to create implemented and analyze a preliminary multiphysics model without its validation.

Symbol	Value	Description
D_{V2}	2.4e-10 [m²/s]	V(2+) diffusion coefficient
D_{V3}	2.4e-10 [m²/s]	V(3+) diffusion coefficient
D_{V4}	3.9e-10 [m²/s]	VO(2+) diffusion coefficient
D_{V5}	3.9e-10 [m²/s]	VO2(+) diffusion coefficient
D_{H}	9.312e-9 [m²/s]	H(+) diffusion coefficient
D_{SO4}	1.065e-9 [m²/s]	SO4(2-) diffusion coefficient
D_{HSO4}	1.33e-9 [m²/s]	HSO4(-) diffusion coefficient
T	298 [K]	Cell temperature
σ_e	66.7 [S/m]	Electrode conductivity

ε	0.93	Electrode porosity
a	35e4 [m²/m³]	Electrode specific area
$E_{0_{pos}}$	1.004 [V]	Standard potential, positive reaction
k_{pos}	2.5e-8 [m/s]	Rate constant, positive reaction
α_{pos}	0.55	Transfer coefficient, positive reaction
$E_{0_{neg}}$	-0.255 [V]	Standard potential, negative reaction
k_{neg}	7e-8 [m/s]	Rate constant, negative reaction
α_{neg}	0.45	Transfer coefficient, negative reaction
β	0.25	Dissociation constant
k_d	1e4 [mol/(m³s)]	HSO4(-) dissociation rate constant
c_{Hm}	1.99 [mol/l]	Membrane proton concentration
c_{V2_0}	560 [mol/m³]	V(2+) initial concentration
c_{V3_0}	884 [mol/m³]	V(3+) initial concentration
c_{V4_0}	884 [mol/m³]	VO(2+) initial concentration
c_{V5_0}	560 [mol/m³]	VO2(+) initial concentration
$c_{H_0,neg}$	4447.5 [mol/m³]	H(+) initial concentration, negative electrode
$c_{H_0,pos}$	5097.5 [mol/m³]	H(+) initial concentration, positive electrode
$c_{HSO4_0,neg}$	2668.5 [mol/m³]	HSO4(-) initial concentration, negative electrode
$c_{HSO4_0,pos}$	3058.5 [mol/m³]	HSO4(-) initial concentration, positive electrode
i_{avg}	-100 [mA/m²]	Average current density
$i_{0_{neg}}$	6.75 [A/m²]	Exchange current density, negative reaction
$i_{0_{pos}}$	2.41 [A/m²]	Exchange current density, positive reaction

Table 3.1 - Input parameter of the preliminary model

3.2.4. Governing Equations

The governing equations for the porose electrode and for the membrane regard the balance of mass and charge in the electrolyte.

Mass balance:

$$\nabla \cdot J_i + u \cdot \nabla c_i = R_i \tag{3.2.1}$$

where J_i represent a generic flux i which can be referred to a mass flux, diffusion, electromigration etc. as indicates the Nernst-Planck equation (equation 2.3.7). In this case it is equal to:

$$J_i - n \cdot \left(- \underbrace{D_i \nabla c}_{Diffusion} - \underbrace{z_i \mu_{m,i} F c_i \nabla \phi_l}_{Electromigration} \right) = 0 \tag{3.2.2}$$

Current balance:

$$\nabla \cdot i_{l,s} = F \sum_i z_i R_i + i_{v,tot} \tag{3.2.3}$$

where $i_{l,s}$ states for the current in the electrolyte and the electrode respectively, $i_{v,tot}$ is the current density of the Butler-Volmer equation and z_i the charge of each species i. For the electrolyte and the electrode respectively, from the Farady law:

$$i_l = F \sum_i z_i J_i \tag{3.2.4}$$

$$i_s = -\sigma \nabla \phi^{surface} \tag{3.2.5}$$

The term R_i is the reaction source due to the porous electrode reactions, while $R_{i,tot}$ the total reaction source, who is sum of the contributes of the reaction sources:

$$R_{i,tot} = \sum_i R_i \tag{3.2.6}$$

The reaction source terms assume different forms for the positive and negative electrodes, reported in Table 3.2.

Species	Negative R_i	Positive R_i
$\mathbf{V^{2+}}$	$A_v i_{loc}/nF$	
$\mathbf{V^{3+}}$	$-A_v i_{loc}/nF$	
$\mathbf{VO^{2+}}$		$A_v i_{loc}/nF$
$\mathbf{VO_2^+}$		$-A_v i_{loc}/nF$
$\mathbf{H^+}$	$-S_d$	$-S_d - 2A_v i_{loc}/nF$
$\mathbf{HSO_4^-}$	S_d	$-S_d$

Table 3.2 – Source terms for the different electrolyte species at negative and positive electrodes. The term S_d indicated the dissociation rate, which will be described in the next section.

Condition of electroneutrality:

$$\sum_i z_i \, c_i = 0 \tag{3.2.7}$$

The condition of electroneutrality is applied for all the species and allows to determine the concentration of the SO_4^{2-} ions without using the equations 3.2.1 and 3.2.3.

Momentum Conservation:

The flow field in the cell electrodes is described by combining the Navier-Stokes equations, which describe fluid motion, with Darcy's law for porous media: the Brinkman's equations. However, for simplicity it is assumed for the moment a homogeneous flow field in all the electrode domains, assumption which is acceptable looking at electrode nature which ensure an equalization of the velocity profile in the cell for a Flow Through configuration. The velocity value is calculated simply in the form $u = \dot{V}/L_e$ where $\dot{V}$ is the volumetric flow rate and L_e the electrode thickness.

The momentum equations will be added successively in order to study also different and more complex cells geometries, for the moment.

3.2.5. Electrodes Domains

At the negative electrode takes place the semi-reaction:

$$V^{3+} + e^- \longleftrightarrow V^{2+} \tag{3.2.8}$$

The species involved in the reaction are:

- H^+: the proton derives from the dissociation of the sulphury acid and is drive through the ion-exchange membrane in order to re-balance the charge.
- HSO_4^-: the acid is used as solvent in the Vanadium solution at negative.
- SO_4^{2-}: after the dissociation of the HSO_4^- the ion SO_4^{2-} remain.
- V^{3+}
- V^{2+}

Similarly, for positive electrode, the semi-reaction:

$$VO_2^+ + 2H^+ + e^- \rightarrow VO^{2+} + H_2O \tag{3.2.9}$$

and the species involved in the reaction are:

- H^+ : the proton comes from the ion exchange membrane and react reducing VO_2^+ into VO^{2+}.
- HSO_4^-: the acid is used as solvent in the Vanadium solution at positive.
- SO_4^{2-}: after the dissociation of the HSO_4^- the ion SO_4^{2-} remain.
- VO_2^+: oxidized specie, can be seen as $V^{5+} + 2\mathrm{O}^{-2}$.
- VO^{2+}: reduced specie, can be seen as $V^{4+} + \mathrm{O}^{-2}$.

The potential at the anode and cathode can be calculated with the Nernst equation (equation 2.1.15) and is respectively:

$$E_{eq}^{-} = E^0 + \frac{RT}{nF} ln \frac{a_{V^{2+}}}{a_{V^{3+}}} \tag{3.2.10}$$

$$E_{eq}^{+} = E^0 + \frac{RT}{nF} ln \frac{a_{VO^{2+}} a_{H^+}^2}{a_{VO_2^+}} \tag{3.2.11}$$

The activity term it is supposed equal to the reactants concentration itself (low concentration species) but with the units of mol/L.

The Current density (local reactions rates), recalling the Butler-Volmer equation (equation 2.2.10):

$$i_v^{-} = A\ j_0^{-} \left(\frac{c_{V^{2+}}}{c_{V^{2+}}^{0*}} e^{\frac{\alpha n F \eta_{act}}{RT}} - \frac{c_{V^{3+}}}{c_{V^{3+}}^{0*}} e^{\frac{(1-\alpha) n F \eta_{act}}{RT}} \right) \tag{3.2.12}$$

$$i_v^{+} = A\ j_0^{+} \left(\frac{c_{VO_2^+}}{c_{VO_2^+}^{0*}} e^{\frac{\alpha n F \eta_{act}}{RT}} - \frac{c_{VO^{2+}}}{c_{VO^{2+}}^{0*}} e^{\frac{(1-\alpha) n F \eta_{act}}{RT}} \right) \tag{3.2.13}$$

In the equation 3.2.12 and 3.2.13, the concentration $c_{V^{2+}}, c_{V^{3+}}, c_{VO_2^+}, c_{VO^{2+}}$ represents the average concentration at the mesh element in the electrode, while $c_{V^{2+}}^{0*}, c_{V^{3+}}^{0*}, c_{VO_2^+}^{0*}, c_{VO^{2+}}^{0*}$ represent reference concertation equals to 1M. The term A is the specific surface area of the porous electrode, or volumetric area (m^3/m^2).

The activation losses for positive and negative electrodes are respectively:

$$\eta^{+} = \phi_s - \phi_l - E_{eq}^{-} \tag{3.2.14}$$

$$\eta^{-} = \phi_s - \phi_l - E_{eq}^{+} \tag{3.2.15}$$

where ϕ_s, ϕ_l denotes the equilibrium potentials at the surfaces and at the electrolyte.

It is necessary to implement also the dissociation of the sulfuric acid in order to have a correct evaluation of the source term for the protons as reported in Table 3.2. In literature it is often assumed that the first step of dissociation process occurs to completion, while the dissociation rate of the second step, R_d, is determined by the following equation [13]:

$$H_2SO_4 \ \rightarrow \ HSO_4^{-} + H^{+} \qquad (1^{th}\ step) \tag{3.2.16}$$

$$HSO_4^- \rightarrow SO_4^{2-} + H^+ \qquad (2^{nd}\ step) \tag{3.2.17}$$

For this non-electrochemical reaction in the negative electrolyte domain, the source term corresponds to the reaction rate:

$$S_d = k_d \left(\frac{c_{H^+} - c_{HSO_4^-}}{c_{H^+} + c_{HSO_4^-}} - \beta \right) \tag{3.2.18}$$

where k_d is the dissociation rate constant, and β is the degree of dissociation of HSO_4^-.

At all these equations it is possible to apply some correction for the active surface and for the electrical conductivity of the electrode, this for it porose nature. These corrections are available in literature as the Bruggeman correction (section 292.3.1, equations 2.3.9 and 2.3.10).

3.2.6. Electrodes Boundary Conditions

Referring to the geometry in Figure 3.2.2, it is possible to assume no flux boundary conditions in the external regions of the electrode, where the current collector i.e., the bipolar plates take place.

In these regions, the equations of the model are:

$$-n \cdot J_i = 0 \tag{3.2.19}$$

where J_i represent a generic flux i.

The negative electrode is supposed grounded, so, at the negative current collector, together with the no flux condition:

$$\phi_s = 0 \tag{3.2.20}$$

At the inlet and outlet flow stream, both for positive and negative electrode, the insulation boundary conditions are assumed, which describes the walls of a cell or the boundaries of the cell that do not face a conductor. These boundary conditions impose the equation:

$$i_k \cdot n = 0 \tag{3.2.21}$$

where i_k denotes the current density vector and $k = l, s$ is an index for the electrolyte and electrode, respectively.

Moreover, at the inlet region, will be specified the initial concentrations of the reactants c_{i_0}, as reported in Table 3.1. The equation at the inlets boundaries is:

$$n \cdot \left(J_i + u_{c_i}\right) = n \cdot \left(u\ c_{i_0}\right) \tag{3.2.22}$$

Concerning the outflow, it is assumed that convection are the dominating transport mechanisms across the boundary, and therefore that the diffusive transport can be ignored, that is:

$$n \cdot \nabla(-D\nabla c) = 0 \tag{3.2.23}$$

3.2.7. Membrane Domain

In the membrane no chemical reaction takes place, but generally only transport mechanisms. However, a detailed modelling considers the boundary of the membrane as reactions sites where the interfaces of the electrodes is in contact with that of the membrane.

The ionic conductive membrane theoretically allows the passage only for the H^+ protons. Considering only this ideal behavior of the membrane, according with the Faraday law:

$$n \cdot J_{H^+} = n \cdot \frac{i_l}{F} \tag{3.2.24}$$

where i_l is the current in the electrolyte who derive from the electrodes reactions how described in Chapter 3.2.5. This current is "ionic" current, transported by ionic species inside the membrane. The membrane act as a "ionic conductor", characterized by a specific conductivity for each ion who pass through.

Making an analogy with the Ohm law, as explained in section 2.3.1, the electrolyte current i_l becomes:

$$i_l = \sigma_{l,mem}^{eff} \nabla \phi_l \tag{3.2.25}$$

with $\sigma_{l,mem}^{eff}$ the effective membrane conductibility. It is easy to recognize from the combination of the Nernst-Planck equation and the definition of electrolyte current the expression for $\sigma_{l,mem}^{eff}$, as made for equation 2.3.4:

$$\sigma_{l,mem}^{eff} = \sum_i z_i^2 F^2 c_i \mu_{m,i} \tag{3.2.26}$$

With the Nernst-Einstein relation for the mobility $\mu_{m,i}$ (equation 2.3.3)

$$\sigma_{l,mem}^{eff} = \frac{F^2}{RT}\sum_i z_i^2 c_i \; D_i \tag{3.2.27}$$

where c_i is the ionic membrane concentration of the specie i calculated by taking the arithmetic mean of the positive and negative half-cell. The diffusion coefficients are assumed to be of the ideal electrolyte, and they are corrected for the membrane tortuosity with the Bruggeman correction.

In this case, differently from the case for which equation 2.3.4 has been obtained, the conductivity of the membrane is due by the sum of all the membrane conductivities values for all the species who cross the membrane.

3.2.8. Membrane Boundary conditions

Two major phenomena must be taken into account at the membrane boundaries: the self-discharge reactions due to the crossover and the built-in of the Donnan potential.

Concerning the crossover phenomenon, it is assumed a fast irreversible electrode reaction at the electrode-membrane interface where the kinetics is so fast that the only factor limiting the reaction rate is the transport of a species to the reacting surface[5]. In this way it is set the rate limiting species concentration to zero at the boundary, and balance the fluxes of the species participating in the reaction and the current densities according to the stoichiometric coefficients. These chemical reactions are:

- At negative half cell:

$$VO_2^+ + 2V^{2+} + 4H^+ \rightarrow 3V^{3+} + 2H_2O \tag{3.2.28}$$

$$VO^{2+} + V^{2+} + 2H^+ \rightarrow 2V^{3+} + H_2O \tag{3.2.29}$$

- At positive half cell:

$$V^{2+} + 2VO_2^+ + 2H^+ \rightarrow 3VO^{2+} + H_2O \tag{3.2.30}$$

$$V^{3+} + VO_2^+ \rightarrow 2VO^{2+} \tag{3.2.31}$$

These reactions occur at the electrode surface so that this kinetic must be represented as a boundary condition:

$$n \cdot J_i = n \cdot \frac{-\nu_i i_l}{nF} \tag{3.2.32}$$

Regarding the Donnan potential, this describes the distribution of ions across a semipermeable membrane that separates two solutions. This phenomenon occurs when there are permeant ions (those that can pass through the membrane) and non-permeant ions (those that cannot pass through the membrane). The movement of permeant ions leads to a separation of charges across the membrane, and can create an electrical potential across the membrane, known as the Donnan potential ($\Delta\phi_l$). This potential affects the movement of ion and can be expressed as:

$$\Delta\phi_l = \phi_{l,1} - \phi_{l,2} = -\frac{RT}{z_{i,2}F} ln\left(\frac{c_{i,1}}{c_{i,2}}\right) \tag{3.2.33}$$

where 1 and 2 indicate the electrolyte and membrane phases respectively.

The membrane consists of a polymer electrolyte, with additional negative ions fixed in the polymer matrix, implying that the concentration for this species is constant. In the ion-exchange membrane domain, a fixed space charge, ρ_{fix} is added while calculating the sum of charges in the electroneutrality condition:

$$\rho_{fix} + \sum_i z_i \, c_i = 0 \tag{3.2.34}$$

For consistency, the equality of the current density across the membrane must be verified:

$$n \cdot i_{l,1} = n \cdot i_{l,2} \tag{3.2.35}$$

3.2.9. Computational Details

The model here exposed presents 23 different depended variables:

- Negative Electrode:

$$cH_{neg} \quad cSO_4^{2-}{}_{neg} \quad cHSO_4^{-}{}_{neg} \quad cV^{2+} \quad cV^{3+} \quad \phi_{l_{neg}} \quad \phi_{s_{neg}}$$

- Membrane:

$$cH_{neg} \quad cSO_4^{2-}{}_{neg} \quad cHSO_4^{-}{}_{neg} \quad cV^{2+}_{mem} \quad cV^{3+}_{mem} \quad V^{4+}_{mem} \quad V^{5+}_{mem} \quad \phi_{l_{mem}} \quad \phi_{s_{mem}}$$

- Positive electrode:

$$cH_{neg} \quad cSO_4^{2-}{}_{neg} \quad cHSO_4^{-}{}_{neg} \quad cV^{4+} \quad V^{5+} \quad \phi_{l_{pos}} \quad \phi_{s_{pos}}$$

The computational problem has been solved with a structured mesh that present the following characteristics:

- Number of elements: 4616
- Elements average quality: 0.9857

It has been used a Direct solver method and the final problem has presented:

- Degree of freedom: 116 992
- Internal Degree of freedom: 5788

The solution time is 44 seconds.

3.3. Preliminary Results

3.3.1. Reactants Concentration

The study of reactants concentration is one of the major goals of this thesis. A preliminary result of the reactants concentration is displayed in Figure 3.3.1.

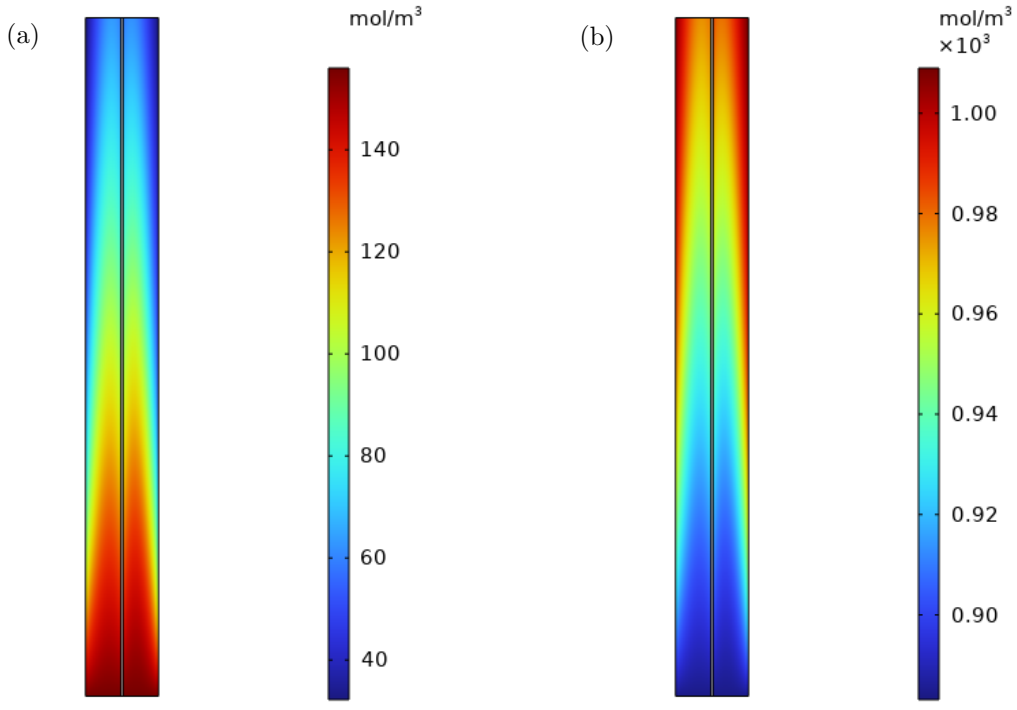

Figure 3.3.1 – V2, V5 species concentration (a), V3, V4, species concentration (b), in the 2D section of the cell. Flow rate: 30ml/min, Current extracted: 100 A/m².

Some parametric sweeps have been performed in order to observe the variation of reactant distribution inside the electrode. The results obtained are reported in Figure 3.3.2. The observed trend shows how for an increasing of electrolyte velocity in the cell there is a more homogeneous reactant distribution. This led at higher current densities a flatter polarization curve for the high renovation rate of reactants.

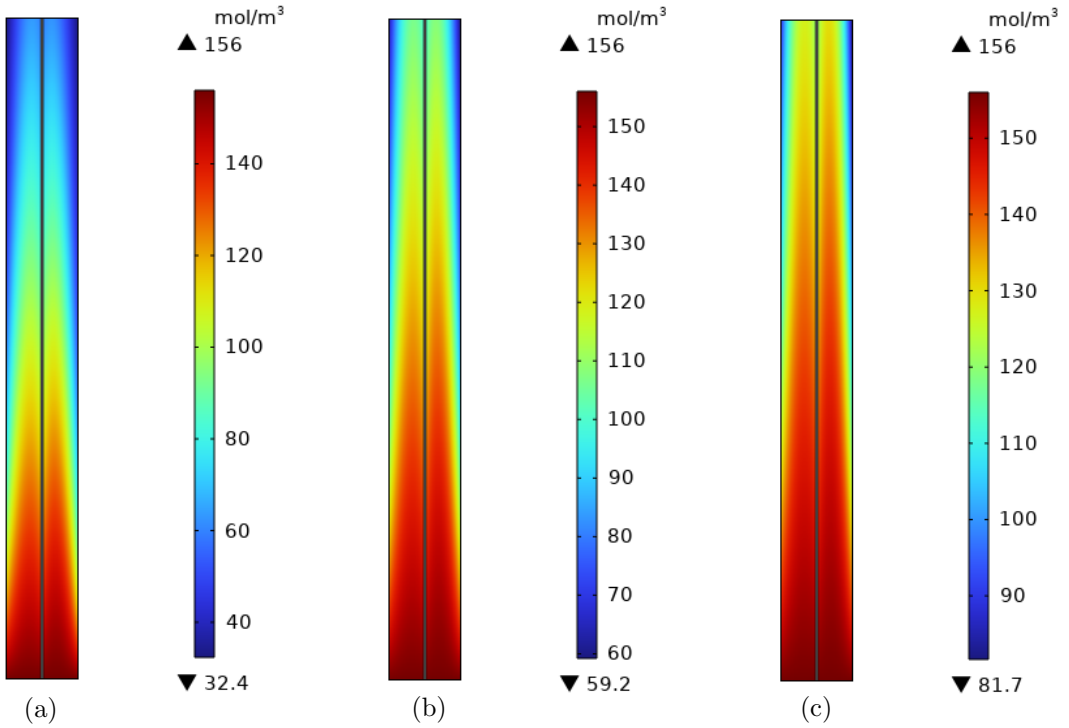

Figure 3.3.2 - Reactants concentration V2-V5 in the electrodes for different values of flow rate: (a) 30 ml/min, (b) 50 ml/min, (c) 80 ml/min, at a current density extracted of 100 mA/cm²

3.3.2. Electrolyte Potential

The electrolyte potential is a form of measure of the electrolyte species concentration. This is plotted for a cut-line at half-cell height in Figure 3.3.3. The Donnan potential shifts at the membrane boundaries are clearly visible in Figure 3.3.3.

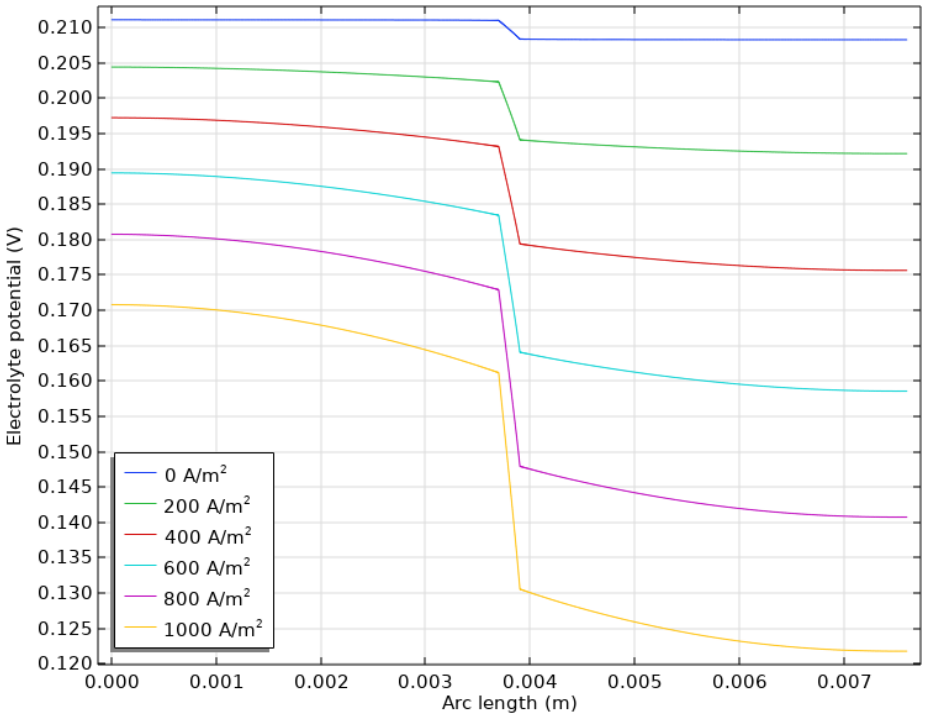

Figure 3.3.3 – Electrolyte potential for different current extracted, flow rate 30 ml/min.

3.3.3. Electrode Reaction Sources

The electrode reaction current source has a maximum value located toward the current collectors, with a minimum located in the middle of the electrodes. For an increase of the velocity the differences between the minimum and maximum values are accentuated as for an increase of the current extracted (current extracted has negative values), as shown in Figure 3.3.4 and Figure 3.3.5.

The big difference between the trend of the reaction sources at the two flow rates can be attributed to the high rate of reactants depletion in the boundaries of the cell which cause a sharp reduction of the reaction rate in these areas, as visible in Figure 3.3.2, especially for the lower flow rates.

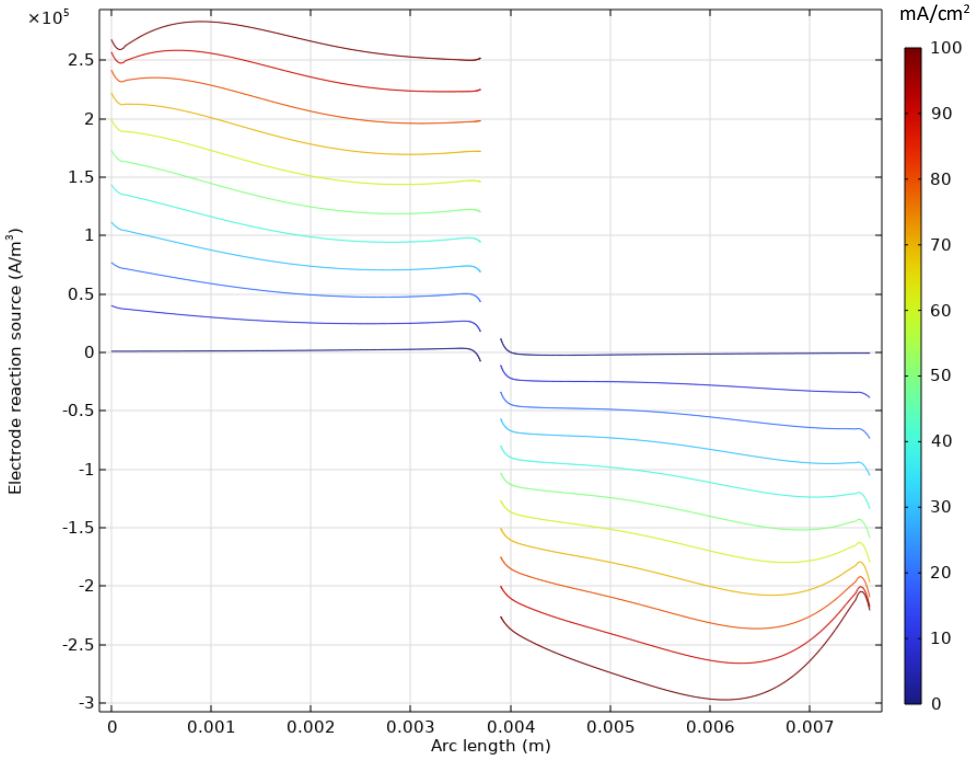

Figure 3.3.4 – Electrode reaction sources for different current densities, flow rate: 30ml/min.

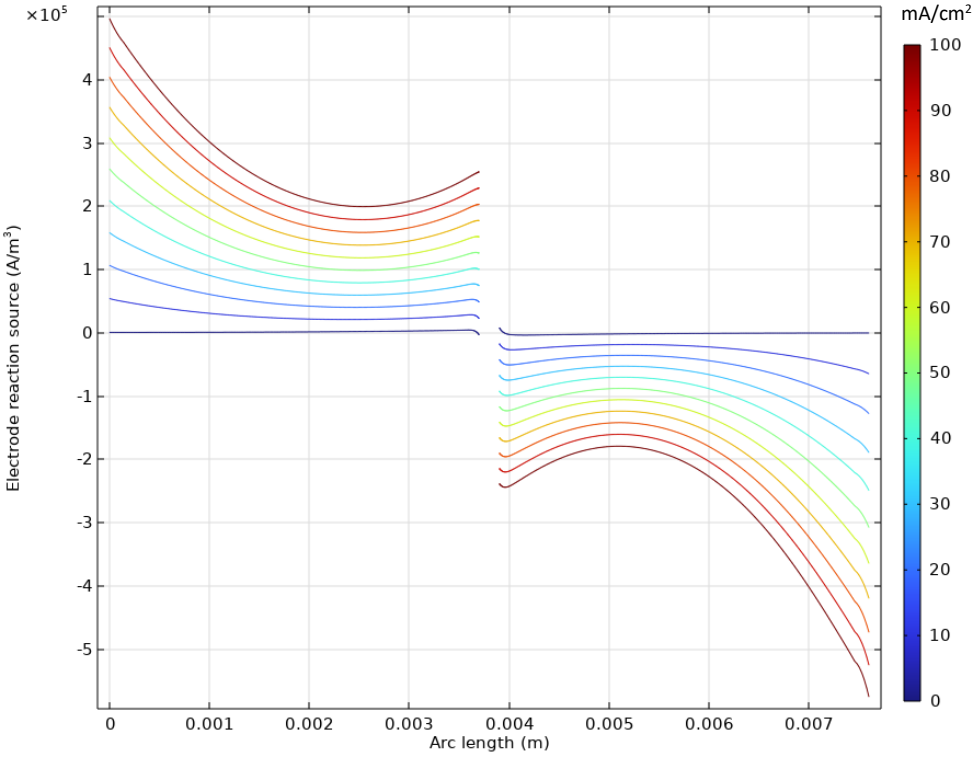

Figure 3.3.5– Electrode reaction sources for different current densities, flow rate: 100ml/min.

3.3.4. Polarization Curve

The plot of polarization curve is done by varying the applied current i_{avg} and monitoring the electric potential at the boundary (ϕ_s^+).

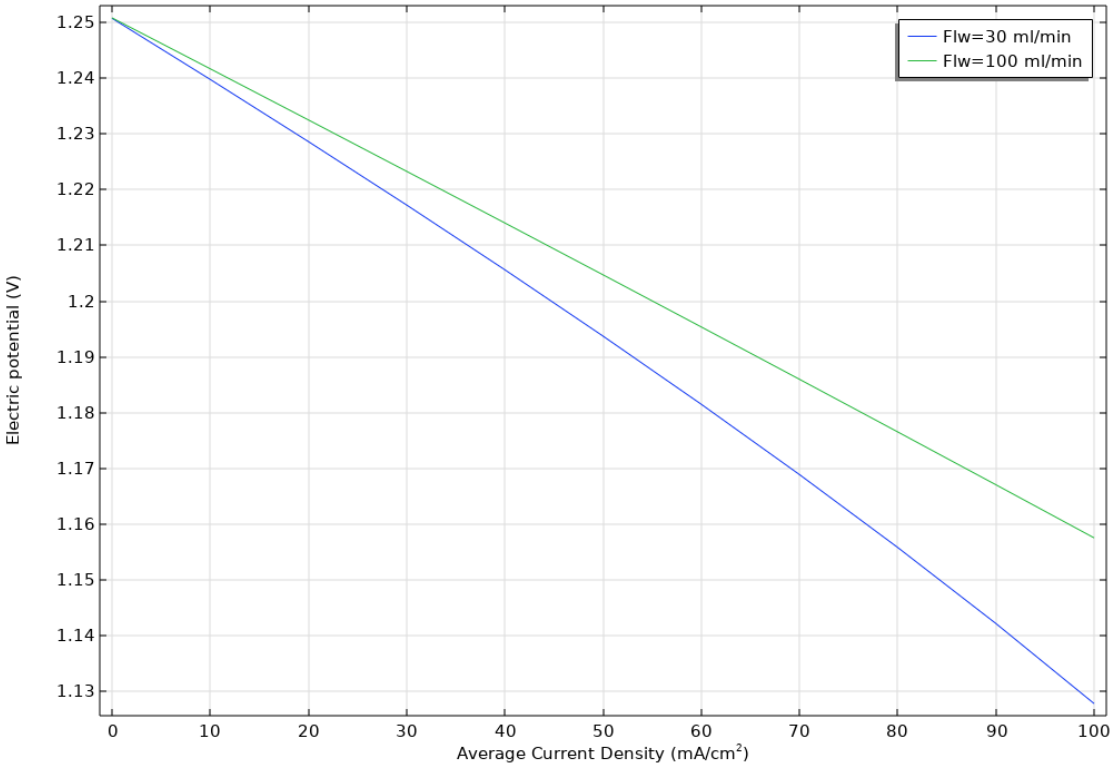

Figure 3.3.6 – Polarization curve of the cell for different flow rate values. High polarization values are evident for low velocity and high current densities.

It is possible to see in Figure 3.3.6 a noticeable deviation in the polarization curve's trajectory, particularly at lower velocities and higher currents. This deviation is attributed to concentration losses (Section 2.3.2), which become more pronounced under these conditions, exacerbated at higher currents, where the demand for reactants increases, and at lower velocities, where the reduced flow does not sufficiently replenish the depleted reactants.

This deflection is a critical observation as it highlights the interplay between fluid dynamics and electrochemical reactions within the VRFB system.

3.4. Reformulation of the 2D Model

The engineering approach to validate and optimize the electrochemical cell led to the necessity to formulate simpler models, easier to understand and easier to re-adapt, that needs few input parameters but who guarantee precise and realistic results.

3.4.1. Assumptions

The model assumptions remain almost identical to that of the previous model reported in 3.2.1:

- Stationary case
- The electrolyte flow is incompressible and laminar because of the small pressure gradient and low flow velocities.
- The evolution of hydrogen and oxygen and the accompanying gas bubble formation in the electrodes are ignored.
- The dilute-solution approximation is used to describe species transport.
- The properties of the electrode, electrolyte, and membrane are assumed to be isotropic.

3.4.2. Fluid Dynamics Physics

In VRFB, the electrolyte flow rate plays an important role in the overall system performance: to provide a sufficiently high supply of reactants to the stack is crucial to guarantee its proper operation, as just explained in Chapter 2.3.2.

In general, a high flow rate increases the cell voltage in discharge and reduces it in charge, hence improving the voltage efficiency of the system. This positive effect on the electrochemical performance occurs because a high flow rate increases the reactant concentration inside the stack, thus raising (reducing) the discharge (charge) voltage via the Nernst equation and, more importantly, enhances the mass transport, which permits to substantially reduce the concentration overpotentials.

However, an excessive flow rate results in an increase of the pump power, and augments the pressure drop within the cells which, in turn, may increase the risk of leakage.

The velocity field (profile) is calculated through the Brinkman equations starting from the inlet and outlet conditions:

$$0 = \nabla \cdot [-p2I + K] - \left(\mu\kappa^{-1} + \beta\rho|u_i| + \frac{\rho\nabla \cdot u_i}{\epsilon_p^2}\right) u_i + F \tag{3.4.1}$$

where p is the pressure; μ is the viscosity; ρ is the fluid density; ϵ_p is the porosity, and κ is the absolute permeability of the porous medium. The term I represent the identity matrix and K the permeability tensor, β is the drag coefficient and F the external forces. In this case β and F are equal to zero.

For the porous medium the value of K is:

$$K = \mu \frac{1}{\epsilon_p}(\nabla u_i + (\nabla u_i)^T) - \frac{2}{3}\mu \frac{1}{\epsilon_P}(\nabla \cdot u_i)I \tag{3.4.2}$$

For that model it is considered an isotropic medium while gravitational effects are not considered. The isotropic simplification led to simplify the equation 3.4.1 in the form:

$$\frac{\rho}{\varepsilon}\left((u \cdot \nabla)\frac{u}{\varepsilon}\right) = -\nabla p + \frac{\mu}{\varepsilon}\nabla^2 u - \frac{\mu}{\kappa}u \tag{3.4.3}$$

The value of permeability is estimated by the Kozeny-Carman equation[14]:

$$\kappa = \frac{d_f^2 \varepsilon^3}{16 k_{ck}(1-\varepsilon)^2} \tag{3.4.4}$$

where d_f is the mean fiber diameter in the electrode and k_{ck} is the Kozeny-Carman constant. The Kozeny-Carman constant represents the shape of the objects of which the solid structure is built from. The value of this constant cannot be calculated straightforward for complex microstructures depends [15]. However, literature offers a wide range of Kozeny-Carman constant respect to the porosity of the felts electrodes [16][17] as reported in Table 3.3.

Kozeny-Carman Constant	**Porosity**			
	0.4	0.6	0.8	Close to 1
In plane directon	10.6	7.3	5.9	5.0
Through plane direction	20.9	12.3	8.9	7.1

Table 3.3 - Kozeny-Carman constant respect to the porosity.

Despite the wide range of empirical correlation as the just illustrated such the Kozeny-Carman relation (equation 3.4.4), it is known that the value of electrodes permeability varies significantly in function of the electrode treatment, fiber diameters, fiber dispositions, compression, impurities etc., making the permeability parameters vary between values of $1 \cdot 10^{-12}$ m^2 and $1 \cdot 10^{-10}$ m^2. For this reason, it is better to use a directly estimated empirically value through an experimental setup.

The relation between the permeability parameter and the pressure losses in the porose medium is clearly explicates by the Darcy law [18]:

$$\kappa = \frac{Q}{A}\frac{\mu L}{\Delta P} \tag{3.4.5}$$

with Q the volumetric flow rate, A the cross-sectional area, μ the viscosity, L the length of the porose medium in the flow direction and ΔP the pressure losses.

From equation 3.4.5 the permeability of the porous media can be calculated by applying a pressure boundary condition on the two opposite faces of the medium and calculating the flux of fluid flowing through the electrode. This procedure will be undertaken in the next chapter for the model validation.

At the inlet, it is supposed a fully developed flow where a flow rate is imposed as constraint. This holds the equation 3.4.6, where A indicates the cross sectional area at the inlet of the electrolyte collector.

$$Q = -\int_A u \cdot n \; dS \tag{3.4.6}$$

For the 2D model the value of A will be represent the inlet area after the collector i.e., the area at the interfaces between the electrode and the flow channel.

At the outlet section the pressure is supposed to be zero with the condition of no-reflux:

$$p_0^{out} \leq p_0 \tag{3.4.7}$$

3.4.3. Physical and Computational Simplification

In this model are make some simplification that importantly reduce the physical and computational complexity of the model. These regards principally the ions transport phenomena in the membrane.

In the previous model as described in section 3.2.7, the mechanism of ions transport is described by the Nernst-Planck equation within the Nernst-Einstein correlation for the ions mobility. In this way the conductivity of the membrane can be calculated starting from the diffusion coefficient as explicated in equations 3.2.27 and the membrane current (equation 3.2.25).

This approach allows to find the distribution of reactants also inside the membrane and a very precise description of the crossover phenomena. However, this required a

very deep knowledge about the membrane material as its properties and the behavior of each species at the membrane interface and in the membrane domain. It is very difficult to find this kind of information in literature and at the end also with this kind of model a lot of simplification must be done in order to have all the parameters in input (diffusion coefficients in the membrane, membrane porosity, membrane selectivity, contact resistances etc.).

To avoid meshing complexity and with the aim to have a model that work with low parameters easy to measure, some additional assumptions have been taken.

Having very thin membranes, the membrane domain can be not considered instead of a boundary condition between the two electrolyte domains. This boundary condition is known in COMSOL as "Thin Electrolyte Layer" and works with the following simplification:

- Single ion transfer: No crossover is considered, only H^+ ions pass trough membrane. This simplifies also the modelling of the fast irreversible reaction at the electrode-membrane interfaces present in the previous model because the vanadium crossover is neglected.
- Predeterminate membrane conductivity: are not more used the diffusions coefficients of the membrane to model, but an average statistical value assumed from experimental measurements or fitting.

The membrane is then seen as a boundary condition, which setting equations are:

$$n \cdot i_l = \frac{\sigma_l}{d_l}(\phi_l^+ - \phi_l^- - \Delta\phi) \tag{3.4.8}$$

$$\Delta\phi = -\frac{RT}{zF} ln\left(\frac{c^-}{c^+}\right) \tag{3.4.9}$$

In equation 3.4.3 σ_l is the membrane conductivity, ϕ_l^+ the electrolyte potential for at the positive half-cell, ϕ_l^- the electrolyte potential at the negative half-cell and $\Delta\phi$ the Donnan potential reported in equation 3.4.4, function of the difference between the positive and negative electrode of the charge carrying species concentration, c^- and c^+ respectively.

The molar flux of the protons $N_{\mathrm{H^+}}$ in the membrane is:

$$N_{H^+} = \frac{n \cdot i_l}{zF} \tag{3.4.10}$$

Another possible simplification regards the fluid dynamics physics. For this specific geometry, it is possible to assume a complete homogeneous flow in the through cell configuration. This hypothesis is coherent with the velocity profile that will be present in the porose electrode, results of the fluid dynamic simulation implementing the equations described in Section 3.4.2. Indeed, for the very low permeability value of the electrode, the velocity field is extremely easy and present a very flat velocity profile as plotted in Figure 3.4.1.

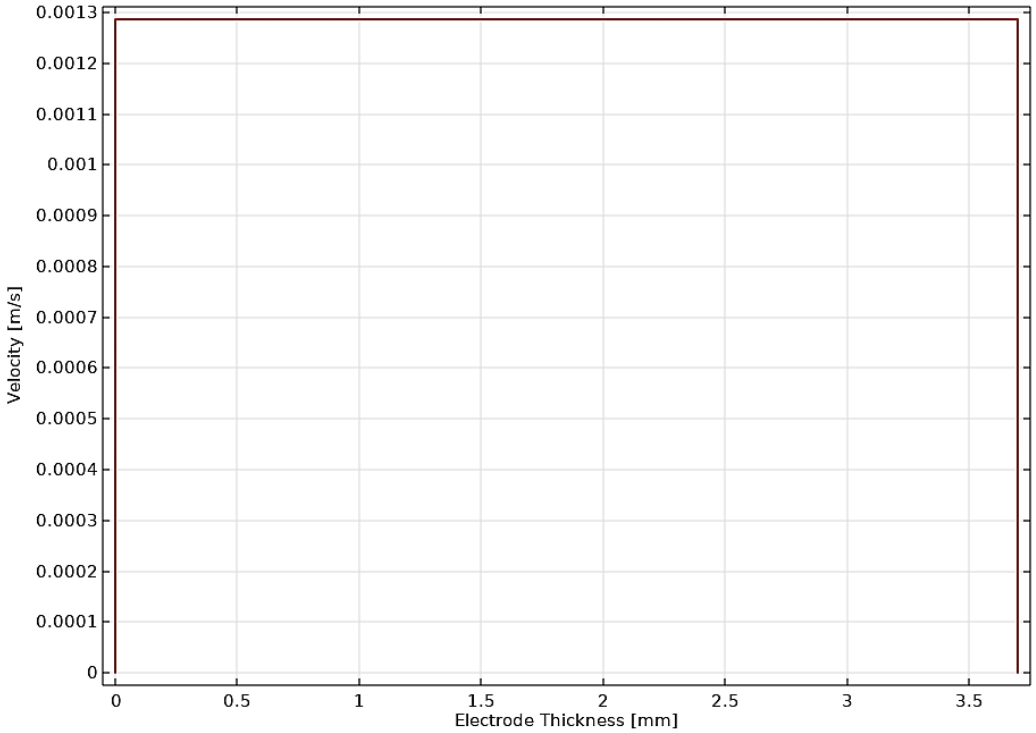

Figure 3.4.1 – Flow Field Velocity profile in the cell. The flow rate is of 80ml/min with an electrode permeability of 3E-11 m^{-1}. The parabolic profile of the velocity, is null at the wall and almost flat in the electrode.

The similarity between the real velocity profile and a complete flat velocity profile led to very similar electrochemical results, if not identical. The distinction lies in the computational time, which is notably higher, by approximately 30%, when fluid dynamics coupling is incorporated.

No more differences have been found also considering the inlet and outlet collectors for the flow through configuration, but converging problem due to the edge at the inlet collectors that led to infinite velocity gradients as reported in Figure 3.4.2. This suggests that while the impact on electrochemical performance might be minimal, the choice of modeling approach can significantly affect computational efficiency and the smoothness of simulation results.

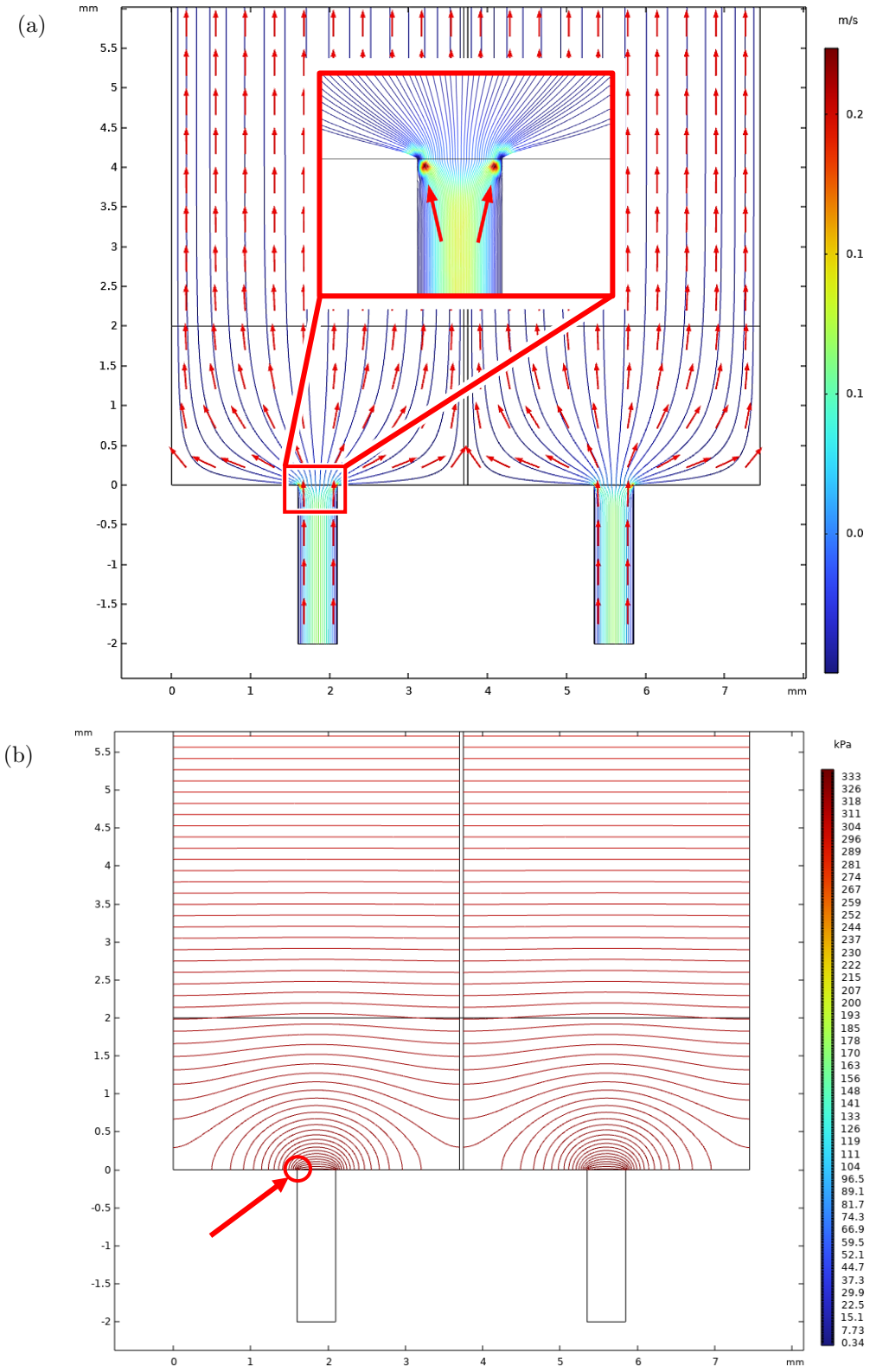

Figure 3.4.2 – Velocity (a) and pressure (b) field in two electrodes at a flow rate of 80ml/min. Are underlined the numerical problems (peak of pressures and velocities) at the edge of two hypothetical inlet collectors. It is possible to observe how at a distance over 2mm from the inlet collectors the pressure and then velocity profile is almost flat.

For the reasons illustrated in this section no flow field coupling is considered for this cell configuration. However, the fluid dynamic implementation described in Section 3.4.2 is not useless because the fluid dynamic physics can play a very fundamental role in the cell performances as the case of other cells configuration such the interdigitated flow field[19].

3.4.4. Computational Details

These simplifications allow to have a very lower input parameters request by the model but at the same time ensure lower computational complexity. Indeed, only one Physic Interface has been used in COMSOL and in this case the model presents 9 different depended variables:

$$cH, \quad cSO_4^{2-}, \quad cHSO_4^{-}, \quad cV^{2+}, \quad cV^{3+}, \quad cV^{4+}, \quad V^{5+}, \quad \phi_l, \quad \phi_s$$

The computational problem has been solved with a structured mesh that present the following characteristics:

- Number of elements: 3840
- Elements quality: 0.9966

The structured mesh presents a lower number of elements because the membrane domain is not considered for the meshing but as explained in section 3.4.3, the role of the membrane is taken into account as boundary condition for both electrodes

It has been used a Direct solver method and the final problem has present:

- Degree of freedom: 94 713
- Internal Degree of freedom: 4272

The computational time result in 18 seconds. For the lower amount of DOF the new model uses half computational time respect the first model, as expose in section 3.2.9.

3.4.5. Variables and Parameters

The data and the parameters used in the models are the same of that reported in Table 3.1, plus the membrane conductivity. To make a comparison more coherent as possible, the input value of the membrane conductivity is assumed to be the mean conductivity value of the previous model, who correspond to:

$$\sigma_{mem}^{eff} = 7.16 \quad S/m$$

3.5. Preliminary Results Comparison

3.5.1. Reactants Concentration

The differences about reactants concentration of the two models are almost null, as reported in Figure 3.5.1. This is a first good indicators which confirms that the discretization of the membrane can be avoided for the analysis of the electrolyte concentration and distribution.

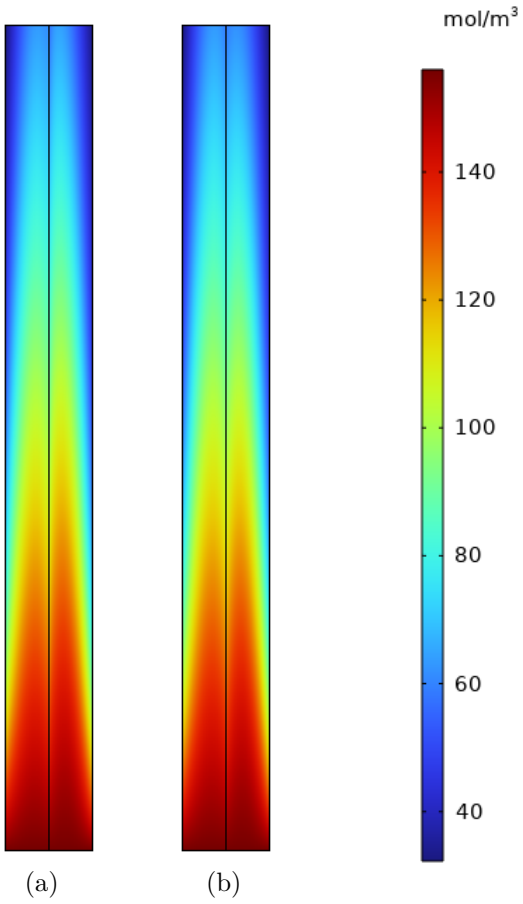

Figure 3.5.1 – V2 - V5 concentration comparisons between the new simplified model (a) and the first model (b). Flow rate 30ml/min, current: 100mA/cm². The differences are almost null.

3.5.2. Electrolyte Potential

Concerning the electrolyte potential, the principal difference between the two model regards the electrode membrane interface. The two models differ of an infinitesimal term to the membrane for the different species concentration. Indeed, species as Vanadium not pass through the membrane in the new model, so they not feel the

concentration potential across the membrane. As consequence, in the new simplified model the Donnan potential is calculated only by the ratio between the protons (or the other carrying charge species) between the two half-cells, while in the first model also the other species was considered.

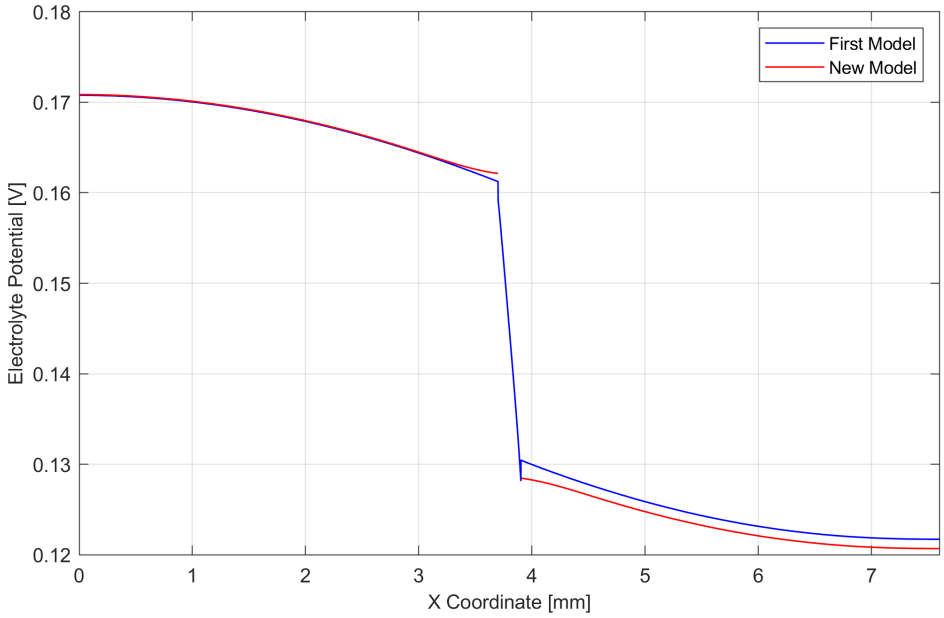

Figure 3.5.2 – Electrolyte Potential comparisons

The very infinitesimal difference confirms the coherence of the assumption at the electrodes-membrane interfaces.

3.5.3. Electrodes Reaction Sources

Similarly to the electrolyte potential, the electrodes reaction sources are very similar in the two models. Small differences are found near the membrane. This can be due for the absence of the fast-irreversible reactions in the new model due to the neglecting of the crossover phenomenon which causes the self-discharge of the membrane.

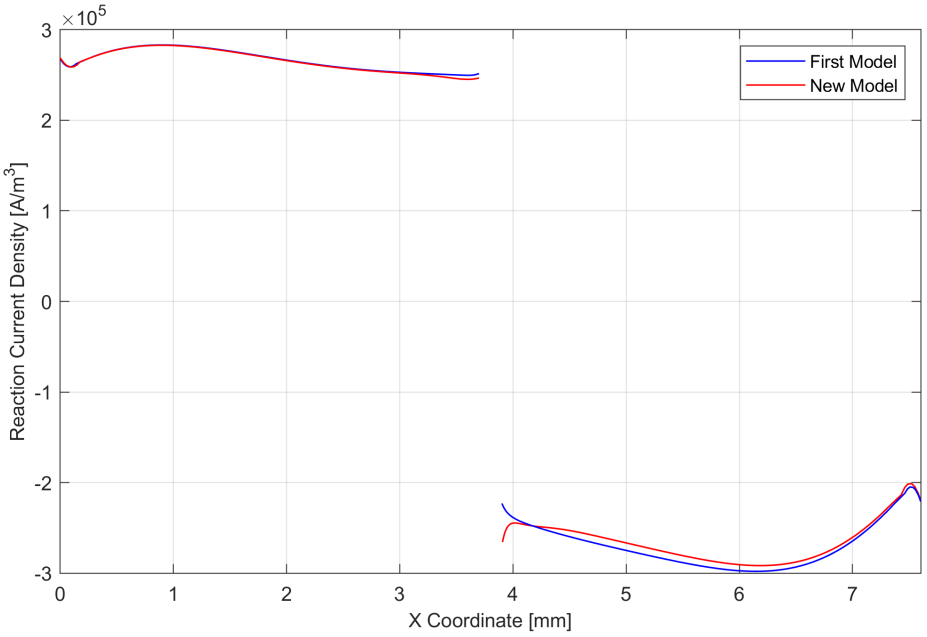

Figure 3.5.3 – Electrode reaction Sources comparisons

3.5.4. Ionic Fluxes

For the assumption of single ion transfer, the fluxes of ions in the cell thickness are very different. While for the first model species as SO_4^{2-} and HSO_4 have a low diffusion coefficient but not null, for the new model this species does not cross the membrane, and protons are the only species carrying the charge. This is well shown in Figure 3.5.4.

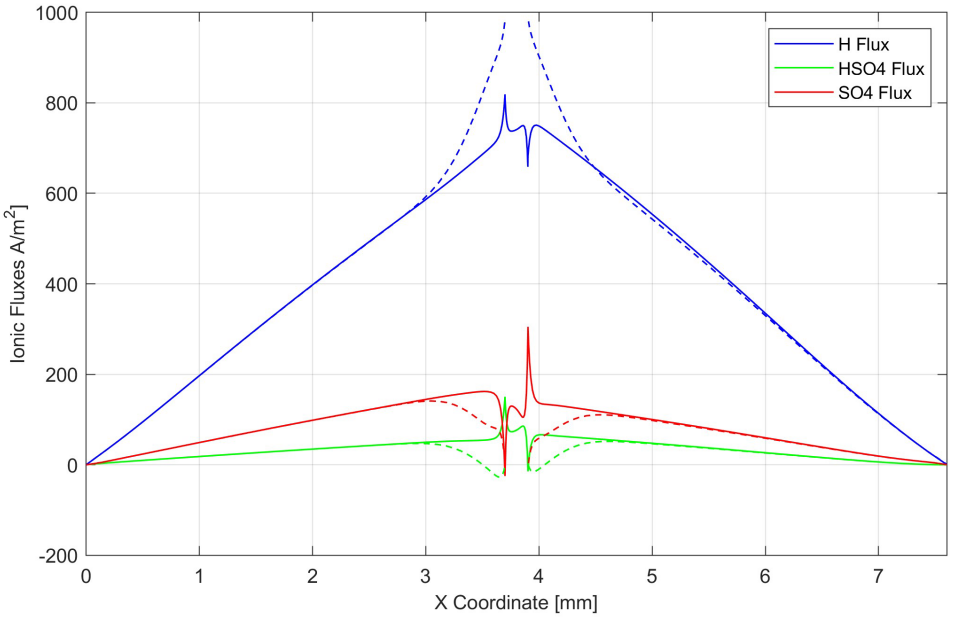

Figure 3.5.4 – Ionic Fluxes Comparisons. The continuous line refers to the first model, the dotted line to the new model.

3.5.5. Polarization Curves

The two demonstrative polarization curves are reported in Figure 3.5.5. The differences are almost null in each point. This means that for a future validation of the model or future analysis based on the cell performance the new model can be very attractive for its simplicity and precision respect the first model.

This results also justifies the decision to omit the crossover phenomena and auto-discharge effects from the new model. When the primary goals are to predict the polarization curve accurately, identify overpotentials, and map the concentration of reactants across the cell's spatial coordinates, these omissions are acceptable. Such simplifications align with the objectives of this work, which aim to provide clear insights into the performance characteristics of the cell without the computational burden of modeling every physical phenomenon.

This approach allows for an efficient yet effective analysis, focusing on key performance indicators relevant to the study.

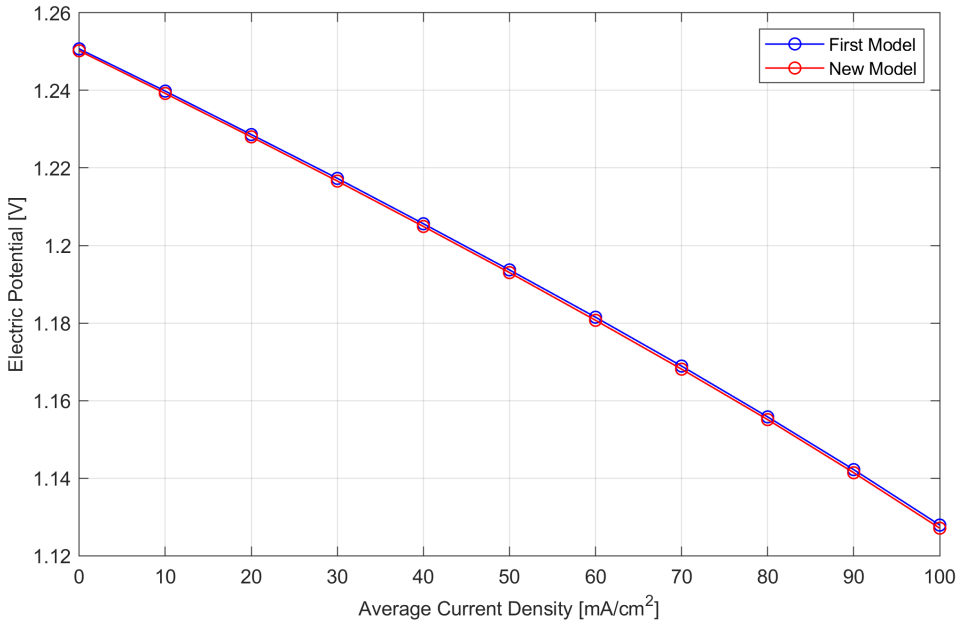

Figure 3.5.5 – Polarization curves comparisons at flow rate of 30ml/min. The two polarization curves are almost identical.

3.6. 3D Model

The need to develop a 3D model is related to the limitation of the 2D models that even if it is very useful to evaluate initial insights, with a very reduced computational complexity, often fail to capture the full complexity of VRFB operation. As VRFBs evolve to larger scales and encounter diverse operational conditions, a 3D representation becomes imperative to account for spatial variations in key parameters such as electrolyte flow, species concentration, and current density distribution. The transition aims to enhance the predictive accuracy and fidelity of VRFB simulations, enabling more informed design choices and optimization strategies.

3.6.1. Assumptions

The model assumptions for the 3D Model remains the same of the last 2D model

- Stationary case
- The electrolyte flow is incompressible and laminar because of the small pressure gradient and low flow velocities.
- The evolution of hydrogen and oxygen and the accompanying gas bubble formation in the electrodes are ignored.
- The dilute-solution approximation is used to describe species transport.
- The properties of the electrode, electrolyte, and membrane are assumed to be isotropic.

Unlike the 2D models, incorporating fluid dynamics becomes crucial, if not indispensable, in 3D modeling to fully capture the distribution of reactants across every transversal section of the cell. The parameters used for the fluid dynamics simulation are identified from literature [19], [20] and will be discussed in the next chapter together with the validation of the model.

3.6.2. Model

The 3D model was developed based on the principles of the new model introduced in Section 3.4, utilizing the same geometric domain outlined in Section 3.2.2.

To streamline the modeling process and reduce computational demands, the model focuses on only half of the cell domain, leveraging the symmetry inherent to the problem's structure. It's important to note that, despite this simplification and the transition to a 3D framework, the physical equations governing the model remain unchanged. This consistency ensures that the fundamental dynamics and phenomena

characterizing the system's behavior are accurately represented, regardless of the dimensional approach.

The specific domains used in COMSOL for this modeling are detailed in Figure 3.6.1, providing a clear visual reference for this comprehensive simulation approach.

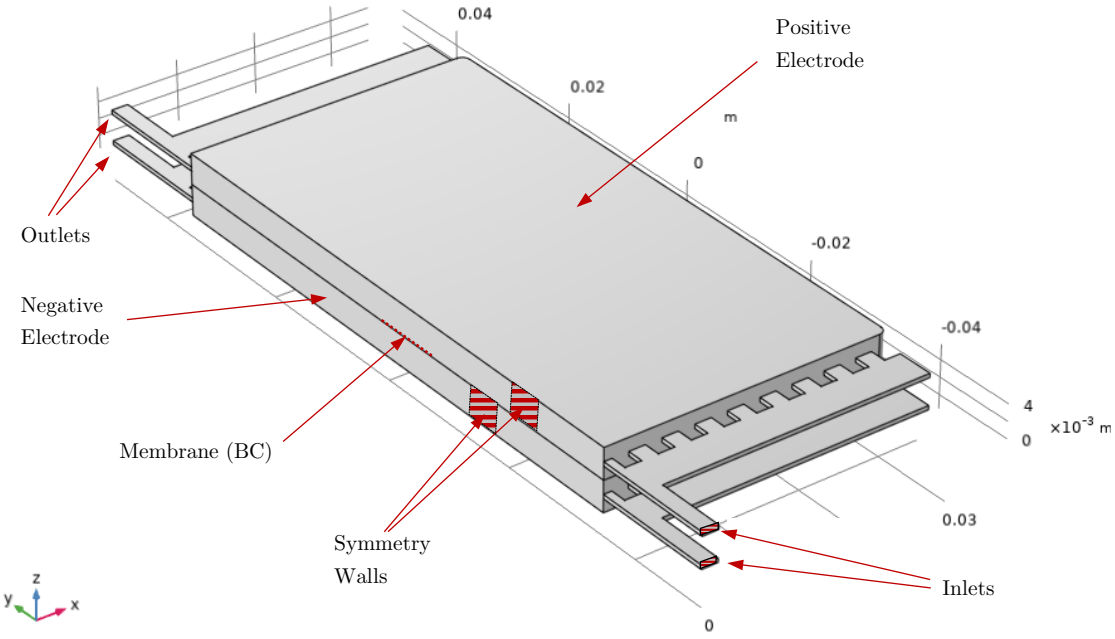

Figure 3.6.1 – 3D model half-cell domains in COMSOL. Are highlight the most important section of the domain geometry as the Positive and negative electrode, the membrane considered as boundary condition (BC), the inlets and outlets for the electrolyte and the symmetry walls which split the cell at the half depth.

The 3D model implemented is designed to use relatively low computational resources, primarily due to the decision not to mesh the membrane. Meshing smaller domains often leads to significantly increased computational times and can adversely affect the convergence of simulation results.

The model has been also simplified no the bases of the reformulated 2D model described in Section 3.4 by reducing the number of dependent variables and neglecting some physical phenomenon as the Vanadium crossover and multiple-ions transfer across the membrane.

Finally, the symmetry condition at the cut-plane allows to reduce of a half the computational burden of the model. This condition can be written as a no flux condition at the boundaries:

$$n \cdot J_i = 0 \tag{683.6.1}$$

These simplifications, as just discussed greatly eases understanding, usage, and resolution of the model.

Detailed analysis of the results obtained from this 3D model will be discussed in the following chapter, which focuses on model validation.

Chapter 4

Model Validation

This chapter focuses on the validation of the 2D Model by comparing it with laboratory measurements and existing models from the literature, specifically looking at Flow Through Flow Field and Interdigitated Flow Field cell configurations. The validation process begins with laboratory measurements to determine the physical and material parameters of the cell, along with experimental data regarding the polarization curves. Following this, a detailed analysis compares the model's output with the experimental data. Through this comparison, the model undergoes calibration and correction, culminating in its validation.

4.1. 2D Model Validation

4.1.1. Reference System and Parameters

To validate the model, it is used a Flow Thought reference cell with the geometrical characteristics described in Chapter 3 at Section 3.2.2.

The geometry built in COMSOL remain then the same described in Section 3.2.2 for the 2D model an in Section 3.6.2 for the 3D model, which validation will be performed successively to the 2D model.

For the validation of the 2D model, as explained in Section 3.4.3, it is assumed the same inlet velocity for each channel, with a homogeneous velocity distribution which led to a flat velocity profile allowing to not coupling the fluid-dynamics with the electrochemistry physics decreasing the computational burden of the model.

The cell is equipped with an Anion Exchange Membrane FAPQ-350, and with two porose electrode SGL-4.65EA. All the data and the parameters of these components used in the model are defined in Table 4.1, in addition or substitution to the just defined values in Table 3.1.

		GEOMETRY	
$\mathbf{H_{cell}}$	0.07[m]	Cell height	Measured
$\mathbf{w_{cell}}$	0.07[m]	Cell depth	Measured
$\mathbf{L_e}$	0.00375[m]	Electrode thickness	Measured
$\mathbf{A_{ex}}$	1.7E-5 [m^2]	Exit Area for the electrolyte	Measured
		ELECTRODES SGL – 4.65EA	
$\boldsymbol{\sigma_e}$	613.3 [S/m]	Electrode conductivity 80% of Compression	Datasheet
$\boldsymbol{\varepsilon_0}$	0.94	Electrode nominal porosity	Datasheet
$\mathbf{A_0}$	115 000 [m^2/m^3]	Electrode nominal specific area	[17]
$\mathbf{L_{e0}}$	4.6 [mm]	Nominal Electrode Thichness	Datasheet
		MEMBRANE – FAPQ-350	
$\mathbf{L_m}$	35e-6[m]	Membrane thickness	Datasheet
$\mathbf{R_m}$	0.7 [Ohm cm^2]	Membrane area resistance	Datasheet
$\boldsymbol{\sigma_m}$	0.9[S/m]	Membrane conductivity	Datasheet
		ELECTROLYTE	
$\boldsymbol{\rho_{neg}}$	1430 [kg/m^3]	Electrolyte Density	[19]
$\boldsymbol{\mu_{neg}}$	4.3E-3 [Pa s]	Electrolyte Viscosity	[19]
$\boldsymbol{\rho_{pos}}$	1430 [kg/m^3]	Electrolyte Density	[19]
$\boldsymbol{\mu_{pos}}$	4.3E-3 [Pa s]	Electrolyte Viscosity	[19]

Table 4.1 - Reference input parameter of the real cell for the model validation. "Measured" indicates measured values in laboratory, "Datasheet" indicates values from the component datasheet, the other are assumed by literature.

The parameters such the electrolyte viscosity and density will be used for the 3D model because for the 2D model the fluid dynamic simplification hold.

The major difference with the preliminary model of Chapter 3 regards the membrane. In this case the membrane used is an anionic membrane (AEM) who allows the passages only for the negative ions. These two types of membranes depend on the fixed ion exchanged groups.

Normally Cationic Exchanged Membrane carry negatively fixed groups while Anionic Exchange Membrane positively charged groups. The interaction of the Vanadium ions whit these groups increase the proton conductivity for the CEM and the proton selectivity for the AEM. For these reasons the carrying charge species across the membrane is assumed to be the ions SO_4^{2-} instead of the protons.

4.1.2. Determination of Ions Concentrations

The polarization curves which will be obtained in laboratory will be relative to a specific state of charges (SOC). In order to make a coherent comparison between the model result and the experimental results, will be necessary to estimate the inlet ions concentration in the electrolyte (c_0) starting from a defined SOC. This because the SOC is determinate by evaluating the OCV of the cell from historical data and measurements so that at each OCV correspond a specific SOC.

To translate the State of Charge (SOC) parameters into reactant concentration values, an analysis of the SOC definition is conducted starting from the following equation:

$$SOC = \frac{Q_{discharged}}{Q_{tot}} \tag{4.1.1}$$

where:

- $Q_{discharged}$ is the quantity of charge discharged by the battery in [Ah];
- Q_{tot} is the total capacity of the battery.

Assuming equal electrolyte flow rate in both electrode, and equal rate of discharge of the two electrodes, it is possible to correlate directly the quantity of charge discharged by the battery and the total capacity of the battery with the concentration of reactants at the inlet of the cell. In this way, the SOC can be expressed in function of the Vanadium concentration in the two electrolytes:

$$SOC = \frac{c_{V,catode} - c_{V,anode}}{c_{V,max}} \tag{4.1.2}$$

where $c_{V,catode}$ and $c_{V,anode}$ indicate the concentration at the inlet at the cathode and anode respectively and $c_{V,max}$ the maximum Vanadium concentration corresponding to the concentration of Vanadium at SOC 100. Assuming the battery is balanced, the resulting equation for the SOC in terms of the Vanadium concentrations results[4]:

$$SOC = \frac{c_{V2}}{c_{V2} + c_{V3}} = \frac{c_{V5}}{c_{V5} + c_{V4}} \tag{4.1.3}$$

Thus:

$$c_{V2} = c_{V3} \frac{SOC}{1 - SOC} \tag{4.1.4}$$

$$c_{V3} = c_{V2}\frac{1 - SOC}{SOC} \tag{4.1.5}$$

With equations 4.1.4 and 4.1.5 will be possible to estimate the inlet Vanadium concentration at negative and positive electrodes of the cell knowing the SOC of the battery.

Assuming for simplicity a SOC of 50, equations 4.1.4 and 4.1.5 hold:

$$c_{Vneg} = c_{Vpos} = \frac{1}{2}c_V^0$$

where c_V^0 indicates the nominal electrolyte V^{2+} and V^{5+} concentration used for the first charge of the battery.

In the laboratory cell, is used the electrolyte 1.6M VSO_4 and 4.6M H_2SO_4. This allows to estimate the Vanadium concentration at the negative and positive electrodes equal to:

$$c_{Vneg} = c_{Vpos} = 800\ mol/m^3$$

A similar approach can be used for the determination of the protons and acid ions concentration. For these are estimated the values of[19]:

$$c_{H^+_{neg}} = 5622.5\ mol/m^3$$

$$c_{H^+_{pos}} = 5622.5\ mol/m^3$$

$$c_{HSO_{4_{neg}}} = 3373.5\ mol/m^3$$

$$c_{HSO_{4_{pos}}} = 3373.5\ mol/m^3$$

4.1.3. Laboratory Polarization Curves Measurements

The measurement of the polarization curves of the cell has been performed at the EESCoLab (Electrochemical Energy Conversion Laboratory) at University of Padova.

The measurement setup used for the determination of the polarization curves is represented in Figure 4.1.1 and Figure 4.1.2.

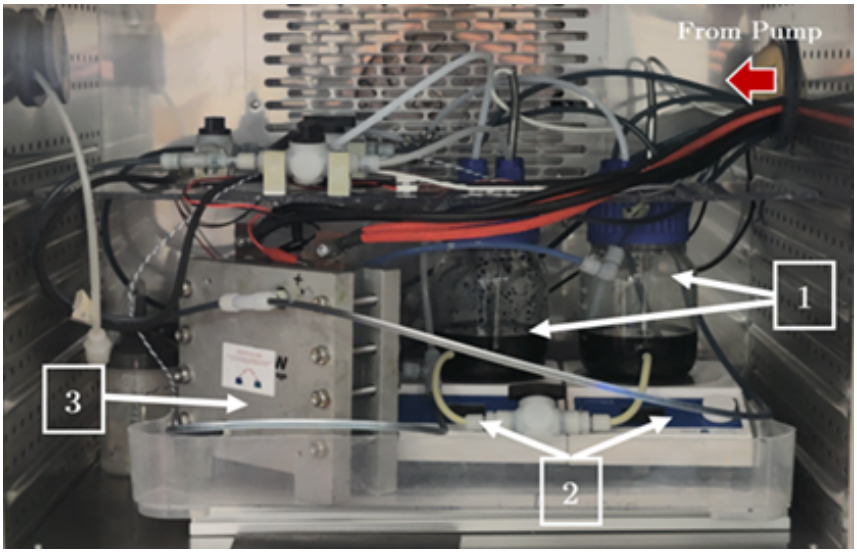

Figure 4.1.1 – Thermal chamber installed at EESCoLab where take place two electrolyte tanks (1), stirrer (2), 50 cm2 FTFF cell (3).

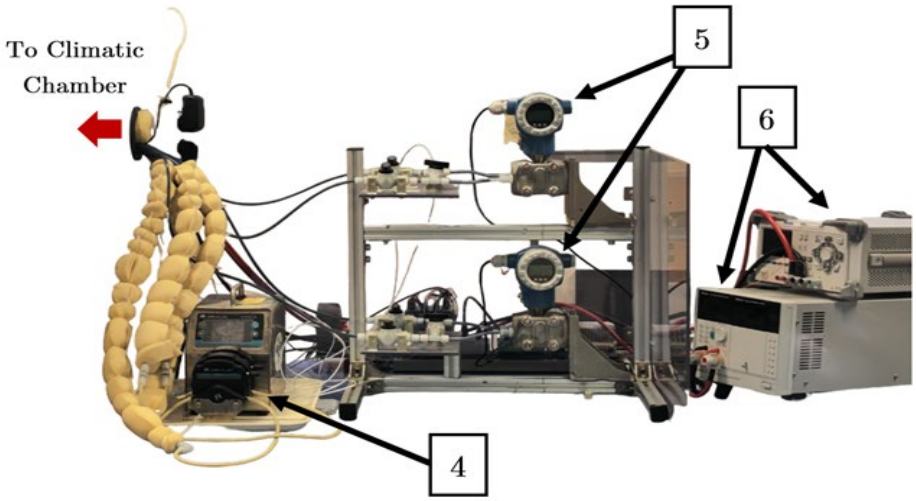

Figure 4.1.2 - VRFB cell test facility (VRFB CTF) installed at EESCoLab: the pump (4), the pressure gauges (5), the power supply (6).

With reference to Figure 4.1.1 and Figure 4.1.2 the experimental setup is composed of:

1- Electrolyte tanks: Two 500ml tanks are used for storing positive and negative electrolytes, containing V4+/V5+ and V2+/V3+ respectively. These electrolytes are dissolved in water and sulfuric acid solution, with a molar concentration of vanadium at 1.6 M and an initial average oxidation state (AOS) of +3.5.
2- Stirrer: Each tank is equipped with a stirrer to ensure uniform concentration, a thermoresistance for temperature measurement, and a nitrogen inlet to prevent

V2+ oxidation in the negative electrolyte. Furthermore, a "bypass" valve connects the tanks when opened.

3- The FTFF 49cm2 cell is equipped with the SGL GFD4.6EA carbon felt electrode and the FAPQ330 AEM membrane.
4- The peristaltic pump is responsible for transferring catholyte and anolyte from the tanks to their respective half-cells and returning them to the tanks. The hydraulic system consists of PE and PTFE pipelines.
5- Differential pressure gauges are installed to measure pressure losses between the inlet and outlet of the cell.
6- Power Supply: The power supply provides the necessary electrical energy for charging the battery and allows controlling the charging process by imposing desired constant voltages and currents. The electronic load absorbs the energy supplied by the battery, simulates electrical loads, and imposes constant discharge currents and voltages. Both can be remotely controlled via a computer. These devices will therefore play a key role in the charging and discharging tests

Between the tanks' outlet and the entrance of the test cell takes place the auxiliary cell, with purpose to measure the open circuit voltage (OCV) of the cell. The OCV is closely related to the cell potential by the Nernst equation. The load voltage can be expressed as $E = E_0 - \eta$, where E_0 is precisely the OCV and η represents the overpotentials due to the charging and discharging processes. During charging, the cell voltage E will be greater than E_0; conversely, during discharging, E will be less than E_0.

The data acquisition station utilizes LabVIEW software, a development and programming environment developed by National Instruments, and consists of a series of modules installed in a dedicated terminal block. These modules acquire signals for temperature through thermoresistances for measuring temperature in the electrolyte tanks and ambient temperature inside the thermal chamber, voltage (direct connection to the cell from the acquisition module), current through an external current probe, and differential pressure through dedicated pressure sensors. One module also enables control of the peristaltic pump for flow rate regulation. All measurements are sent to the computer, which allows data saving and user interface. The aforementioned software autonomously manages data acquisition and dialogue between the user and modules through a script written by laboratory personnel. The control screen of the cell is visible in Figure 4.1.3.

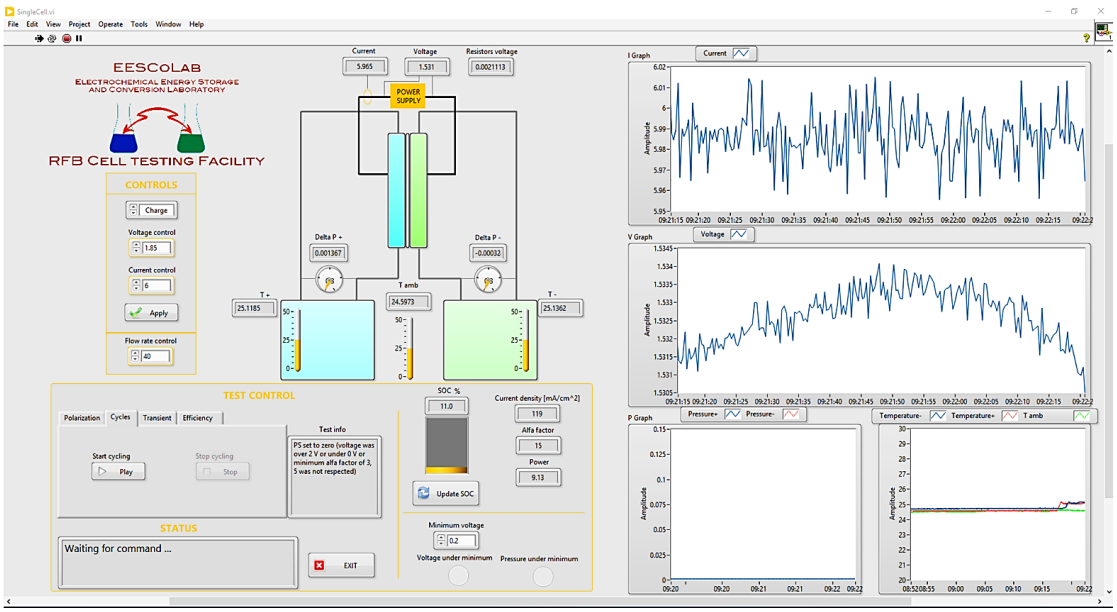

Figure 4.1.3 - Human Machine Interface (HMI) of Flow Battery Management System (FBMS) at VRFB-CTF.

The measurement setup can be resumed in Figure 4.1.4.

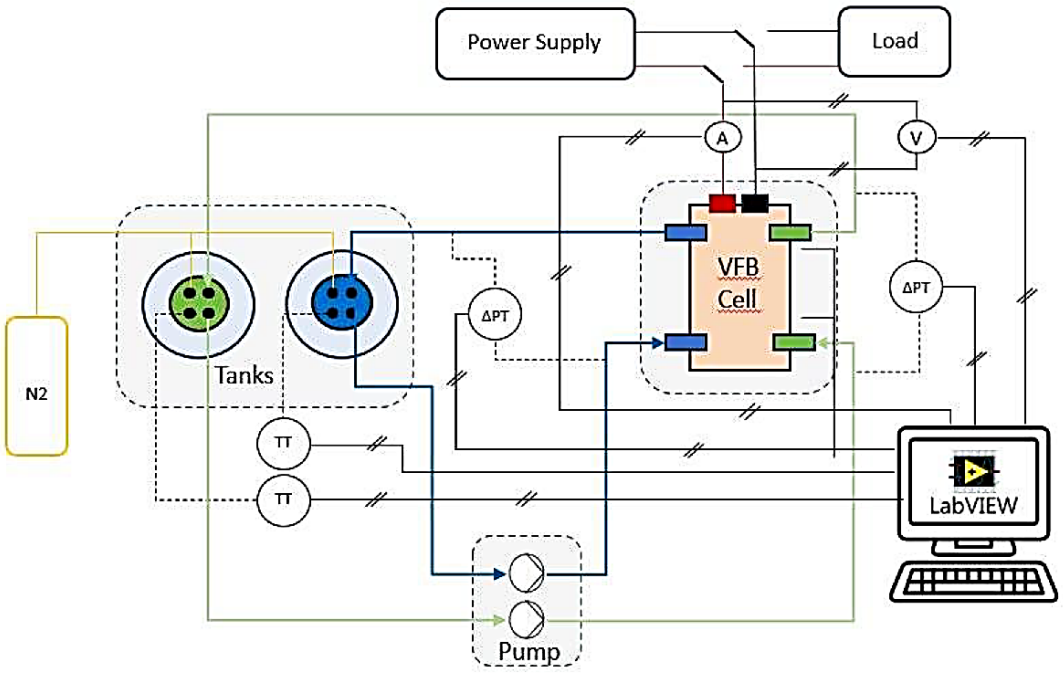

Figure 4.1.4 - Scheme of the measurement setup.

The procedure for conducting these experiments in a laboratory has been performed following the steps:

1. Electrolyte Preparation: Prepared an appropriate electrolyte solution tailored to the specific electrochemical system under study, ensuring consistency and purity in the composition.

2. Initial SOC Adjustment: Set the initial state of charge (SOC) of the system to 50% through controlled charging or discharging processes, maintaining stability prior to commencing measurements.

3. Flow Rate Control: Established two distinct flow rates: 20 ml/min and 80 ml/min, utilizing calibrated flow rate control mechanisms to ensure accuracy and repeatability.

4. Baseline Stabilization: Allowed the system to stabilize at the desired SOC (50%) and flow rate conditions for a sufficient duration to ensure steady-state conditions (Figure 4.1.5 a).

5. Polarization Curve Measurement (20 ml/min): Initiated the measurement process by setting the flow rate to 20 ml/min. Applied a range of potential values across the electrodes while recording corresponding current responses. Ensured each potential value was maintained for adequate time intervals to allow the system to reach steady-state conditions before recording the current in the last time points where the voltage is more stable.

6. Polarization Curve Measurement (80 ml/min): Replicated the measurement procedure described above for the flow rate of 80 ml/min, maintaining consistent experimental conditions.

Commonly, when conducting measurements especially for the lower flow rates and at higher current densities, the experimental protocol includes applying a reverse current immediately after each measurement point. This step is critical to neutralize the effects of battery charging or discharging that occurs during the testing phase. The purpose of this reverse current application is to ensure that the State of Charge (SOC) of the battery remains constant throughout the entire set of measurements for the polarization curve. By doing so, it helps in maintaining uniform conditions, allowing for a more accurate and reliable comparison of the battery's performance across different operating points. This approach is particularly important when exploring the battery's behavior under varying electrical loads and flow conditions, as it directly influences the integrity and consistency of the experimental results.

a)

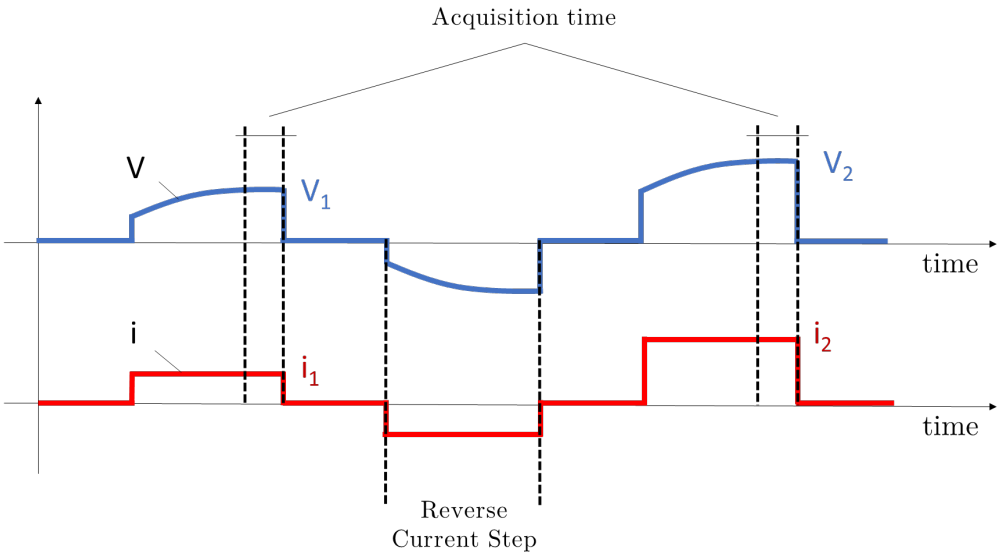

b)

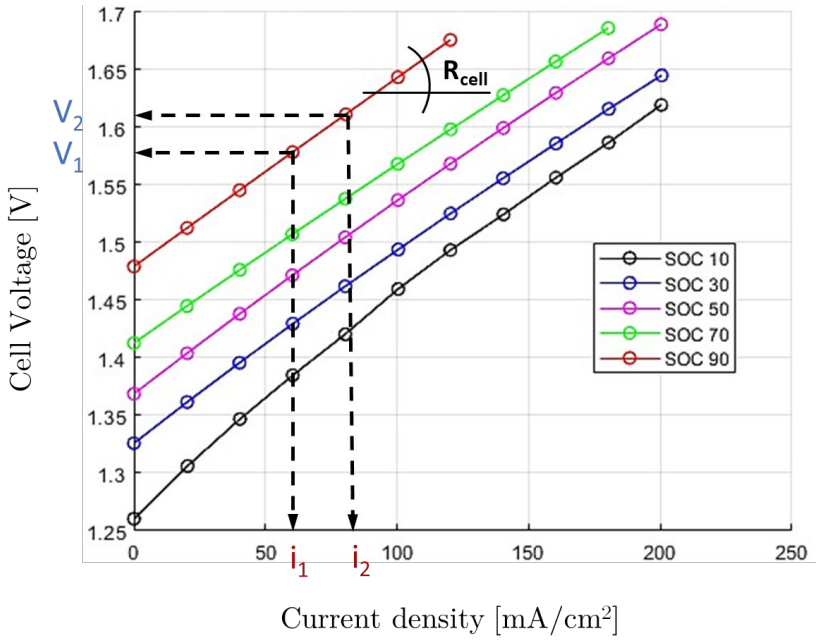

Figure 4.1.5 - Time path for the measurements procedure (a). The acquisition period is performed after the stabilization of the system, successively a reverse current is applied in order to maintain the SOC of the battery almost constant. The polarization curves in (b) are obtained with a flow rate of 50ml/min for different SOC in charge conditions.

4.1.4. Results

The polarizations curves obtained are reported in Figure 4.1.6 where a first comparison with the laboratory measurements is made.

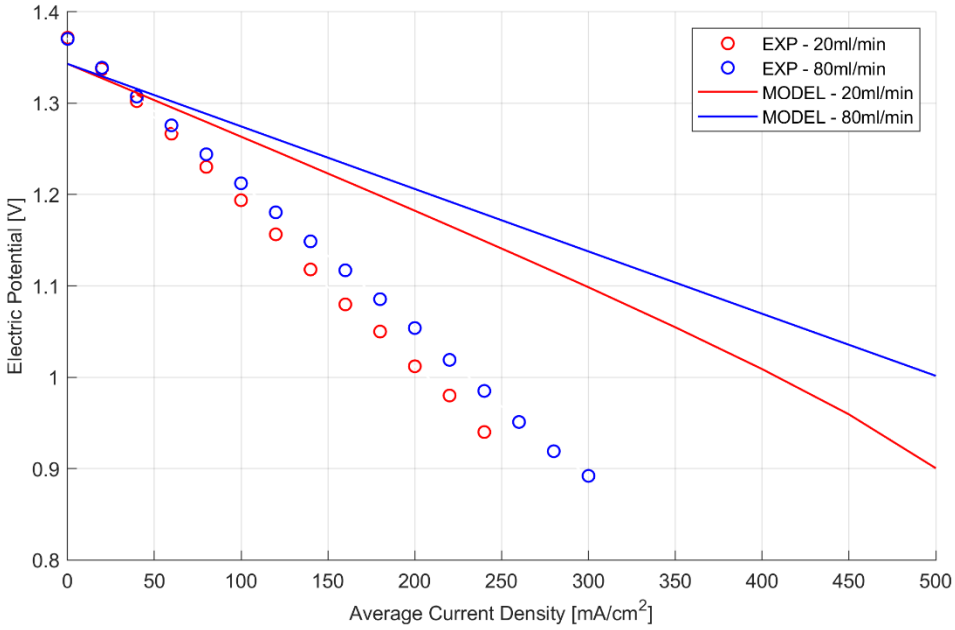

Figure 4.1.6 – Polarization curve comparisons between laboratory measurements and COMSOL 2D-Model.

The curves exhibit distinct differences. Specifically, it is evident that:

1- The open-circuit voltages do not align. These voltages, primarily determined by the Nernst equation, are essentially a function of the concentration of Vanadium at the electrodes, as well as the concentration of other species.
2- The slope of the curves is significantly different, exhibiting much less steepness compared to laboratory data. The slope deviation, according with Section 2.3 is attributed not so much to activation losses but rather to transport losses and ohmic losses. Examination of the membrane conditions, as well as the conductivity factors of the electrode and possibly current collectors, is necessary to ensure accuracy.

These two aspects will be thoroughly examined in the forthcoming sections, which will detail the process of modifying and refining the model. The upcoming analysis will include a step-by-step explanation of the adjustments made to address identified issues, ensuring the model's accuracy and reliability are enhanced. This process will not only involve technical corrections but also integrate additional data or insights that have emerged from the initial findings, laying the groundwork for a more precise and validated model.

4.1.5. Open Circuit Voltage

To analyze the mismatching between the polarization curves obtained it is made a deeper analysis concerning the Open Circuit Voltage OCV.

A complete equation including the proton concentration and the Donnan potential for OCV is [4]:

$$E_{OC} = E_0 + \frac{RT}{F} ln \left(\frac{c_{V_2} \cdot c_{V_5} \cdot (c_H^+)^2}{c_{V_3} \cdot c_{V_4}} \right) \tag{4.1.6}$$

where E_0 is the sum of the equilibrium potential at the negative and positive electrode:

$$E_0 = 1.004 - (-0.225) = 1.229V \tag{4.1.7}$$

A possible explanation of the difference between the OCV measured and that calculated in the model can derive from the proton concentration assumption. A lot of literature articles shown as it is correct to calculated that assuming the complete dissociation of the sulfuric acid [19], [20] thus:

$$c_H^+ = c_H^{ini} + c_{V_5} \tag{4.1.8}$$

where c_H^{ini} is the initial proton concentration at SOC zero.

Considering the vaues used for the Model validation (SOC 50), equation 4.1.6 become:

$$E_{OC} = 1.229 + \frac{8.31 \cdot 298}{96485.33} ln \left(\frac{0.800 \cdot 0.800 \cdot (7.690 + 0.8)^2}{0.800 \cdot 0.800} \right) = 1{,}368 \ V$$

In this way, including that correction in the model, the error with the value measured in laboratory of 1,370V is:

$$Err = \frac{1.370 - 1.363}{1.370} = 0.0051 = 0.51\% \tag{4.1.9}$$

The residual differences between the laboratory and model and in terms of OCV can be influenced by the following reasons:

- Ideal solution assumption
- Imbalanced sytem at measure time
- Measurements errors

However this error can be considered negligible for the goals of the model.

4.1.6. Electrode Conductivity - Bruggeman Correction

The slope of the polarization curve is determinated principally by the ohmic losses in the cell, as just explained in Section 2.3. Generally these losses are determinated by three parameters:

- Electrode conducibility
- Elelctrolyte conducibility
- Membrane conducibility

The electrolyte conducibility depends on the diffusion coefficients of the ions and depends on electrolyte concentration as explained in section 3.2.7. To takes into account more precisely the effect of the porose nature of the electrode the Bruggeman correction is used to calculate the effective diffusion coefficient (equation 2.3.10) as:

$$D_i^{eff} = \varepsilon^{1.5} D_i \tag{4.1.10}$$

where D_i^{eff} is the effective diffusion coefficient of the species i in the porose electrode and D_i^0 the diffusion coefficient in the free electrolyte (often associated with the limit diffusion coefficient) and ε the compressed porosity.

This preclude top know the value of compression ratio (CR) of the electrode which can be derived as:

$$CR = \frac{L_e^{nom} - L_e^{comp}}{L_e^{nom}} = \frac{4.6 - 3.75}{4.6} = 18.5\% \tag{4.1.11}$$

where L_e^{nom} indicates the nominal electrode thickness, L_e^{comp} the compressed electrode thickness.

The compressed porosity is derived from the equation 4.1.11:

$$\varepsilon = \frac{\varepsilon_0 - CR}{1 - CR} = 0.926 \tag{4.1.12}$$

Concerning the membrane conductivity this value has been assumed from the datasheet for its complexity to be measured. The value asusmed is a ponderate average conducibility taken as low as possible in order to consider also possible contact resistances between the membrane and electrodes.

The electrode conductivity can be corrected with the Bruggeman correction (equation 2.3.9) to takes into account for the compression of the electrode:

$$\sigma_e^{eff} = \sigma_e(1-\varepsilon)^{1.5} \tag{4.1.13}$$

where ε is the electrode porosity after compression, while σ_e is the nominal electrode conducibility.

The Bruggeman correction say that the electrode conductivity decrease for an increase of the compression an for a reduction of the void fraction.

The value of conductivity has been evaluated from datasheet. This has been extrapolated by the specific area resistance (AR) for a compression of 80% with the equation:

$$\sigma_e = \frac{L_e^{comp}}{AR} = \frac{0.92\ cm}{0.15\ \Omega\ cm^2} = 613\ \ S/m \tag{4.1.14}$$

Using the Bruggeman correction the electrical conductivity of the electrode compressed at 18% will be:

$$\sigma_e^{eff} = 71.46\ \ S/m$$

The active surface area is corrected for the compression with the equation [17]:

$$A' = A_0 \frac{1-\varepsilon}{1-\varepsilon_0} = 140\ 000\ \frac{m^3}{m^2} \tag{4.1.15}$$

where A' is the active surface area after compression.

4.1.7. Mass Transfer Phenomena

Another significant factor influencing the performance of the electrochemical cell is the mass transfer phenomena. These phenomena play a crucial role, as explained in Section 2.3.2, because the electrochemical reactions take place at the interfaces between the electrolyte and electrodes. The efficiency of these reactions is directly impacted by the concentration of reactants present at these specific locations, which may vary from the average concentrations within the cell. This variation in concentration at the electrode-electrolyte interfaces is essential for understanding and evaluating the cell performances.

According with Section 2.3.2 are made two distinctions:

- Surface concentration: is the concentration of reactants near the solid fibers of the electrode (c_i^s) ;

- Bulk concentration: is the concentration of reactants in the interiors porous region (c_i^b).

In this way the Butler Volmer equation (equation 2.2.10) will be modified in order to takes into account the surface-to-bulk concentration difference:

$$i_v^+ = A\ j_0^+ \left(\frac{c^s_{V^{5+}}}{c^b_{V^{5+}}} e^{\frac{\alpha n F \eta_{act}}{RT}} - \frac{c^s_{V^{4+}}}{c^b_{V^{4+}}} e^{\frac{(1-\alpha) n F \eta_{act}}{RT}} \right) \tag{4.1.16}$$

$$i_v^- = A\ j_0^- \left(\frac{c^s_{V^{2+}}}{c^b_{V^{2+}}} e^{\frac{\alpha n F \eta_{act}}{RT}} - \frac{c^s_{V^{3+}}}{c^b_{V^{3+}}} e^{\frac{(1-\alpha) n F \eta_{act}}{RT}} \right) \tag{4.1.17}$$

There are several ways to determine the surface-to-bulk concentration ratio. One way is too explicit the surface concentration using the Buter-Volmer equation together with the mass transport equation [21]. Recalling then equation 2.3.15:

$$k_m(c_i^b - c_i^s) = \frac{j}{nF} \tag{4.1.18}$$

In this way, the surface concentration can be derived as [20]:

$$c^s_{V2} = \frac{(\overline{P^-} \cdot c_{V3} + (1 + \overline{P^-}) c_{V2})}{1 + \overline{M^-} + \overline{P^-}} \tag{4.1.19}$$

$$c^s_{V3} = \frac{(\overline{M^-} \cdot c_{V2} + (1 + \overline{M^-}) c_{V3})}{1 + \overline{M} + \overline{P}} \tag{4.1.20}$$

$$c^s_{V4} = \frac{(\overline{P^+} \cdot c_{V5} + (1 + \overline{P^+}) c_{V5})}{1 + \overline{M^+} + \overline{P^+}} \tag{4.1.21}$$

$$c^s_{V5} = \frac{(\overline{M^+} \cdot c_{V4} + (1 + \overline{M^+}) c_{V4})}{1 + \overline{M^+} + \overline{P^+}} \tag{4.1.22}$$

where:

$$\overline{M^-} = \frac{k^-}{nk_m} (c_{V2})^{-\alpha_a^-} (c_{V3})^{\alpha_a^-} \cdot exp\left(\frac{\alpha_a^- n F \eta^-}{RT} \right) \tag{4.1.23}$$

$$\overline{P^-} = \frac{k^-}{nk_m} (c_{V2})^{\alpha_c^-} (c_{V3})^{-\alpha_c^-} \cdot exp\left(-\frac{\alpha_c^- n F \eta^-}{RT} \right) \tag{4.1.24}$$

$$\overline{M^+} = \frac{k^+}{nk_m} (c_{V4})^{-\alpha_a^+} (c_{V5})^{\alpha_a^+} \cdot exp\left(\frac{\alpha_a^+ n F \eta^+}{RT} \right) \tag{4.1.25}$$

$$\overline{P^+} = \frac{k^+}{nk_m}(c_{V4})^{\alpha_c^+}(c_{V5})^{-\alpha_c^+} \cdot exp\left(-\frac{\alpha_c^+ nF\eta^+}{RT}\right) \quad (4.1.26)$$

Recalling equation 2.3.16, the k_m parameter can be calculated assuming two parametric coefficients in literature for a flow through cell [20] as:

$$k_m = 1.6 \cdot 10^{-4} \cdot |u|^{0.4} \quad (4.1.27)$$

Equations 4.1.16, 4.1.17 and equation from 4.1.19 to 4.1.27 are implemented in COMSOL using some user-defined variables.

To underline the importance of this phenomena is plotted in Figure 4.1.7 the difference between the polarization curves for a flow rate of 20 ml/min. The role of the mass transport, how explained in section 2.3.2 play a more important role especially at the higher current densities until the limit current is reached, so when the surface concentration of reactants goes to zero.

From the equations 4.1.19 to 4.1.27 it is possible to note how the mass transfer coefficient goes to zero when the velocity is null, for example at the boundary of the system. To avoid numerical divergences, it is assumed a cut-off value for the lower k_m equal 6.5E-7 m/s.

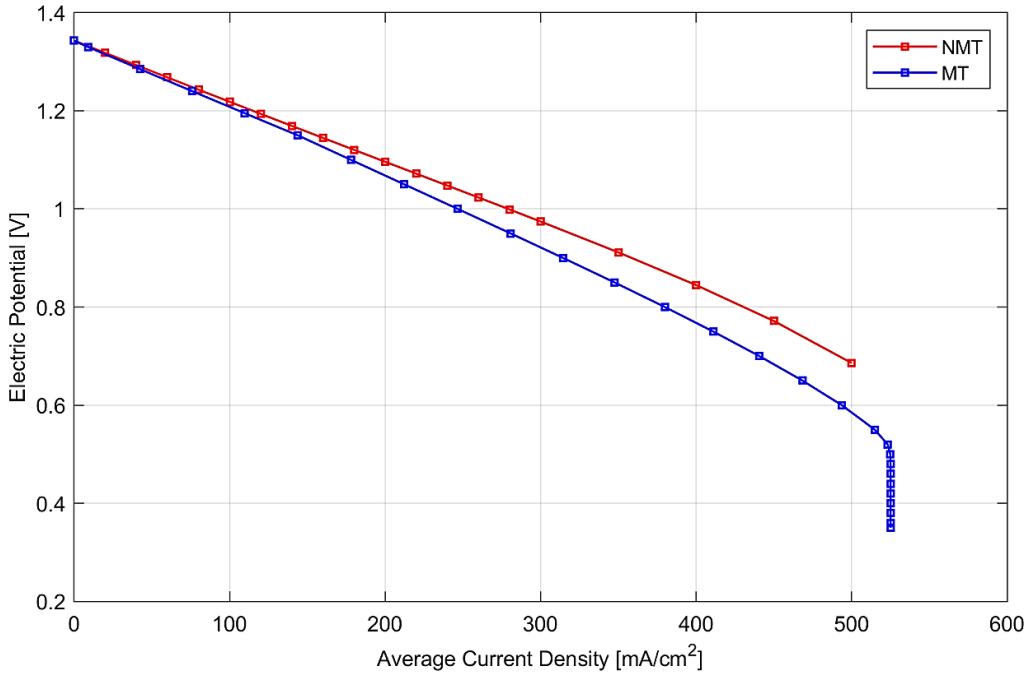

Figure 4.1.7 – Polarization curves comparisons between model with Mass transfer included (MT) and not included (NMT), at a flow rate of 20 ml/min.

4.1.8. Contact Resistances

A critical factor in evaluating the performance of electrochemical cells is the contact resistance encountered at the interface between the electrode and the bipolar graphite plates. Extensive research has been conducted on this topic, as highlighted in the literature. For the electrodes and bipolar graphite plates used in this study, the contact resistance is generally estimated to be around 270 mΩ cm^2 [17]. This value of contact resistance must be accounted for in the model's final cell voltage output by adjusting the voltage accordingly. This adjustment is essential because the contact resistance significantly influences the slope of the polarization curves derived from laboratory measurements, affecting the overall interpretation of cell performance

The final polarization curve voltage ($V_{p.c.}$) will be done by equation 4.1.28:

$$V_{p.c.} = (V_{cell} - i_{avg} R_{contact}) \tag{4.1.28}$$

Where $R_{contact}$ represent the contact resistance and V_{cell} the effective voltage at the electrode.

4.1.9. Validated Results

The final model can be considered validated after have included Mass Transfer phenomena and corrected values of electrode conductivity and ions diffusivity. The final polarization curves are reported in Figure 4.1.8.

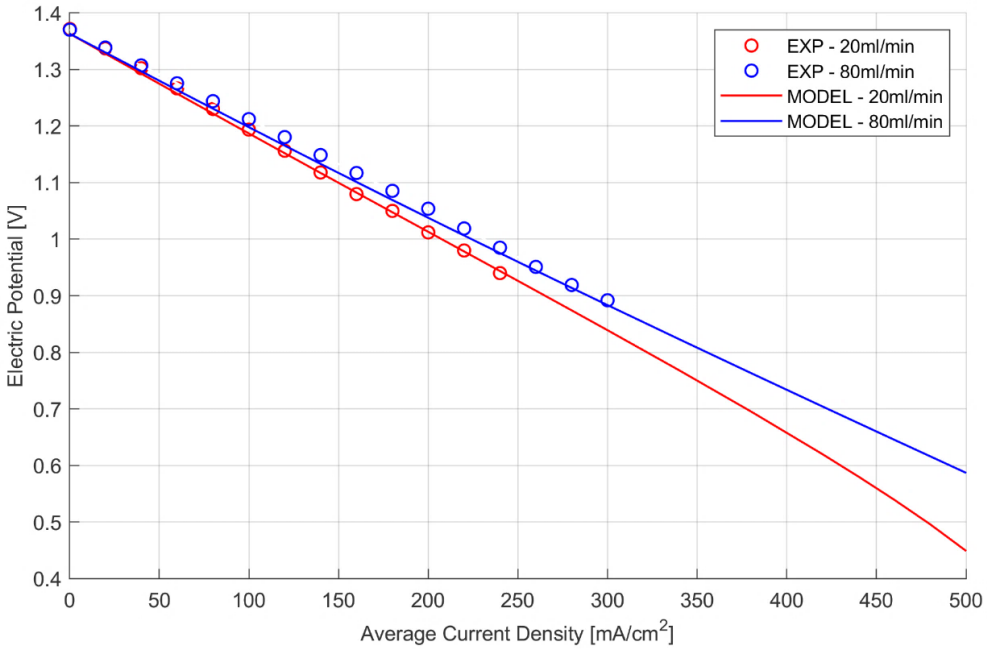

Figure 4.1.8 – Final polarization curve comparisons after the corrections implemented.

The possible increasing of the error with the last data can be due by the instability of the cell at high current densities for the progressively discharge of the flow battery and the depletion of reactants in the tanks.

All the corrections that had permitted the validation of the model and had improved the quality of the results are displayed in Figure 4.1.9. It is possible to observe how the implementation of Bruggeman correction for the electrode conductivity, the mass transport phenomena and the contact resistance progressively fit the experimental data.

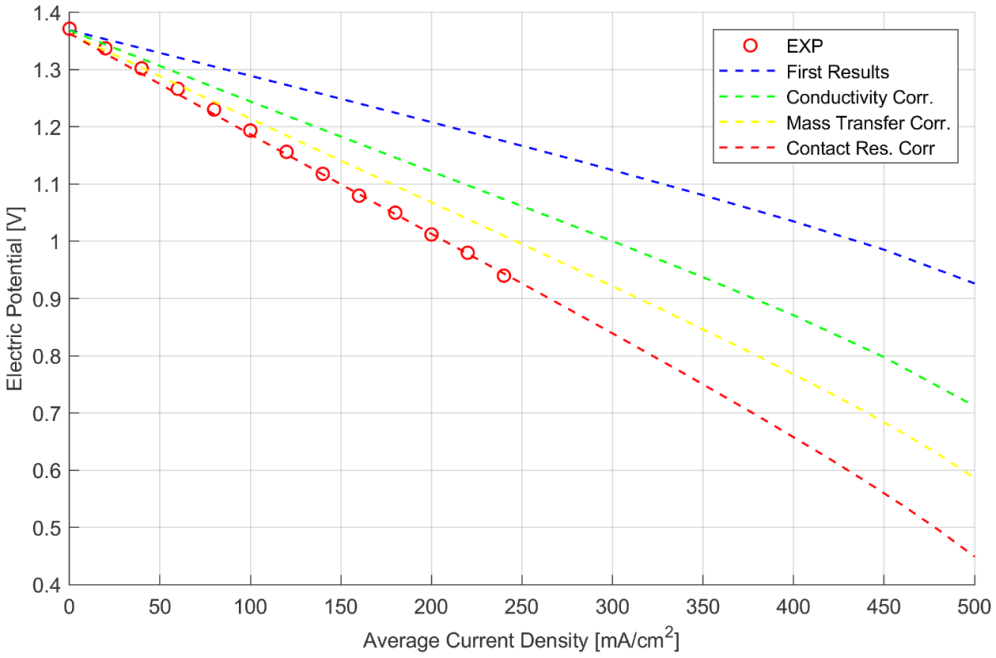

Figure 4.1.9 – Polarization curves for 20ml/min. The different curves show the progressively validation of the model. In all the cases the OCV has been corrected previously.

The distribution of reactants and the potentials, for the value of 100 mA/cm² are plotted in Figure 4.1.10, Figure 4.1.11, Figure 4.1.12 and Figure 4.1.13 while in Figure 4.1.14 are shown the ionic fluxes across the membrane.

The results of the 3D model will be discussed in the next section.

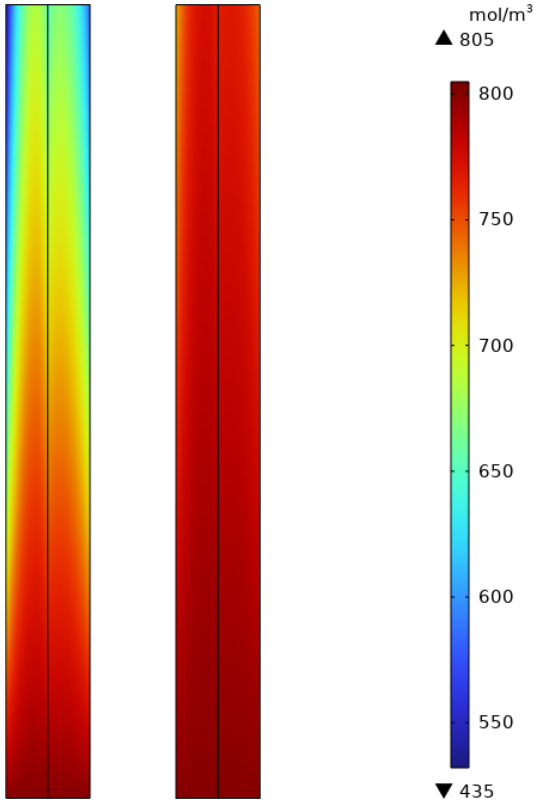

Figure 4.1.10 – V2 and V5 concentration for two different flow rate, 20ml/min (a) and 80 ml/min (b) at current density of 100 mA/cm². To note how the depletion of reactants is more important at the lowest flow rate.

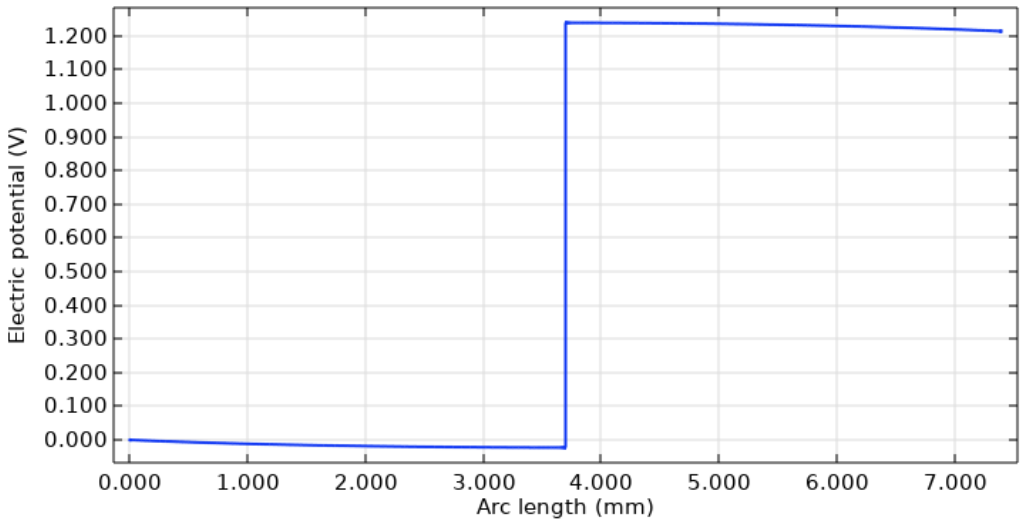

Figure 4.1.11 – Electrode potential at half-cell cut line; 20ml/min, 100 mA/cm².

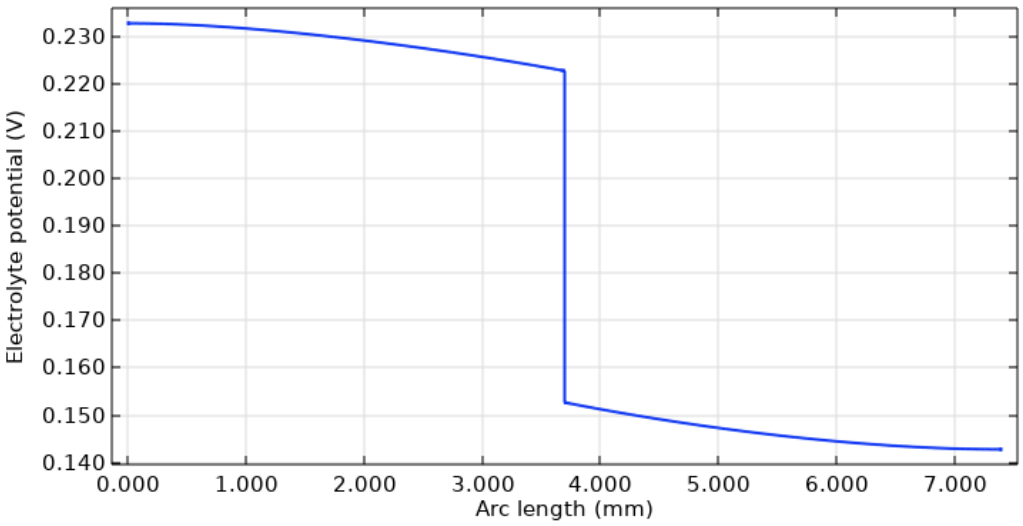

Figure 4.1.12 - Electrolyte potential at half-cell cut line; 20ml/min, 100 mA/cm².

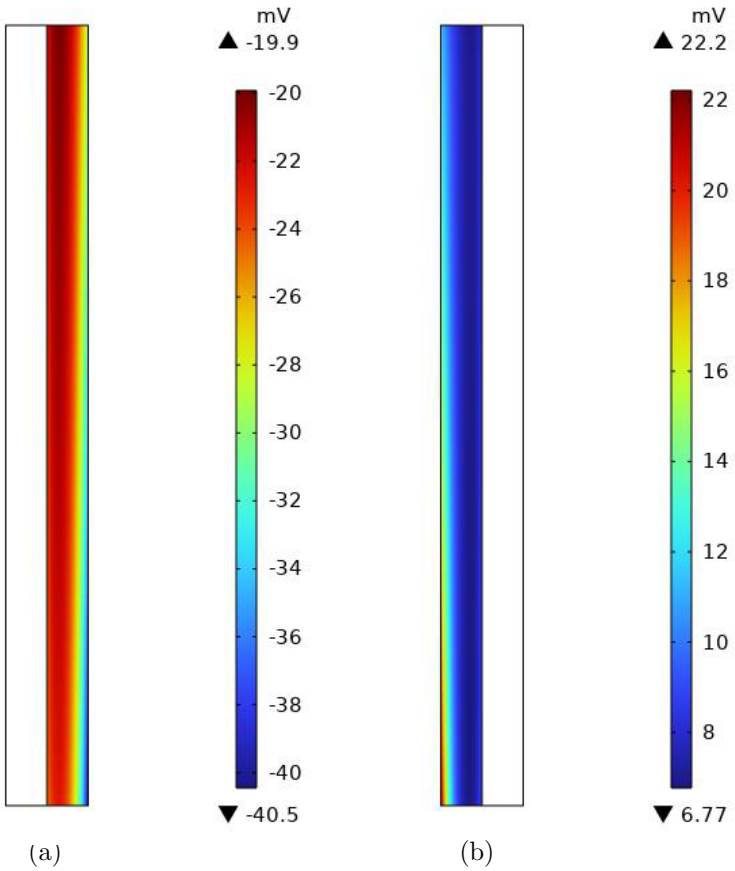

Figure 4.1.13 – Overpotentials for positive (a) and negative (b) electrodes; 20ml/min, 100 mA/cm².

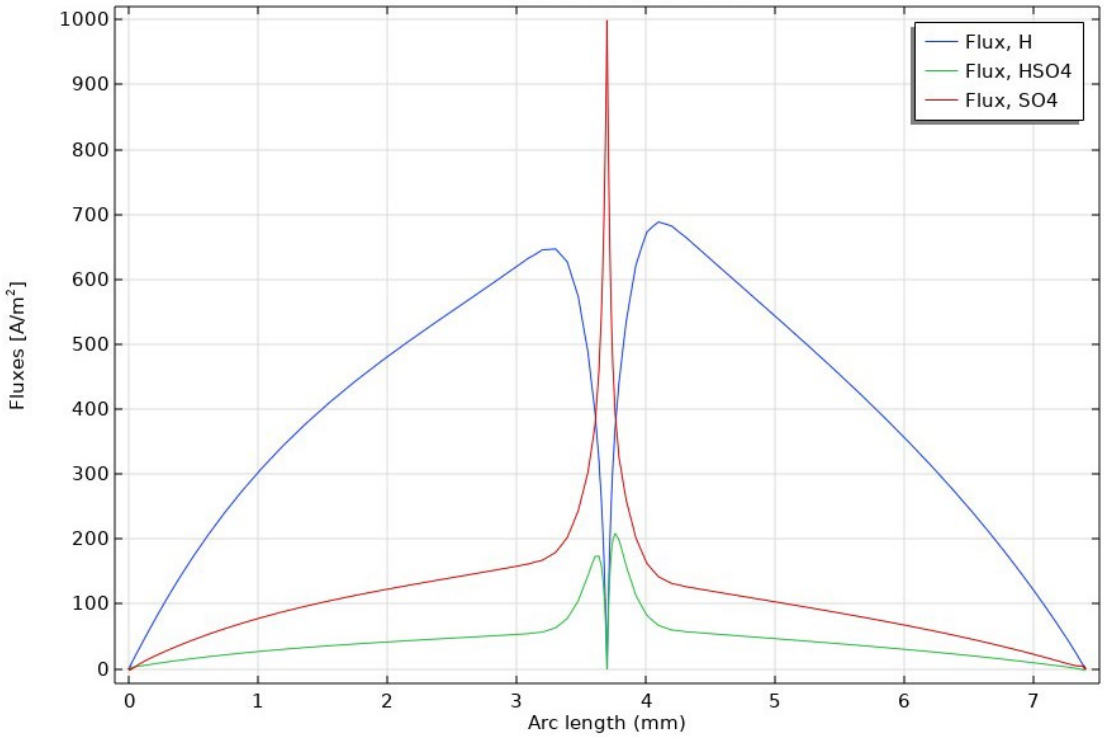

Figure 4.1.14 - Ionic Fluxes for the AEM, half-cell cut line, 1000A/m²; 20 ml/min. Only SO4- ions pass through the membrane.

4.2. 3D Model Validation

The developing of the 3D model of the FTFF laboratory cell has the goal to ensure the validity of the model considering also the third spatial coordinate. Clearly, this model can be meaningless for simple and almost symmetric configuration as the FTFF cell, but it constitutes a fundamental starting point to extend the model for more complex geometry configuration. Thus, the validation the 3D model is a necessary step for the managing of the modelling of the VRFB.

4.2.1. Flow Field

Differently from the 2D model, in the 3D model also the flow field has been modelled, in order to intercept all the possible variations in terms of reactant distribution and kinetic reactions in the cell geometry, having no idea about the distribution of the electrolyte after the inlet collector. This implies also the formulation of a strength model which can be applied also at different geometries configurations or which can be used to perform fluid dynamics optimizations.

To validate then also the model with the fluid dynamic coupling the permeability parameter of the electrode has been estimated from the Darcy law (equation 3.4.5).

For the determination of the permeability κ a pressure difference of 1 *bar* is applied between the two faces of the electrode with the compression ratio of 18.5% according with equation 4.1.11 obtaining a value of permeability of:

$$\kappa = 7 \cdot 10^{-11}\ m^2$$

Analyzing only half-cell, the boundary condition at the inlet described by equation 3.4.6 become:

$$\frac{Q}{2} = \int_A u \cdot n\ dS \tag{4.1.29}$$

The representation of the velocity field is shown in Figure 4.2.1 for the half-cell domain at the negative electrode.

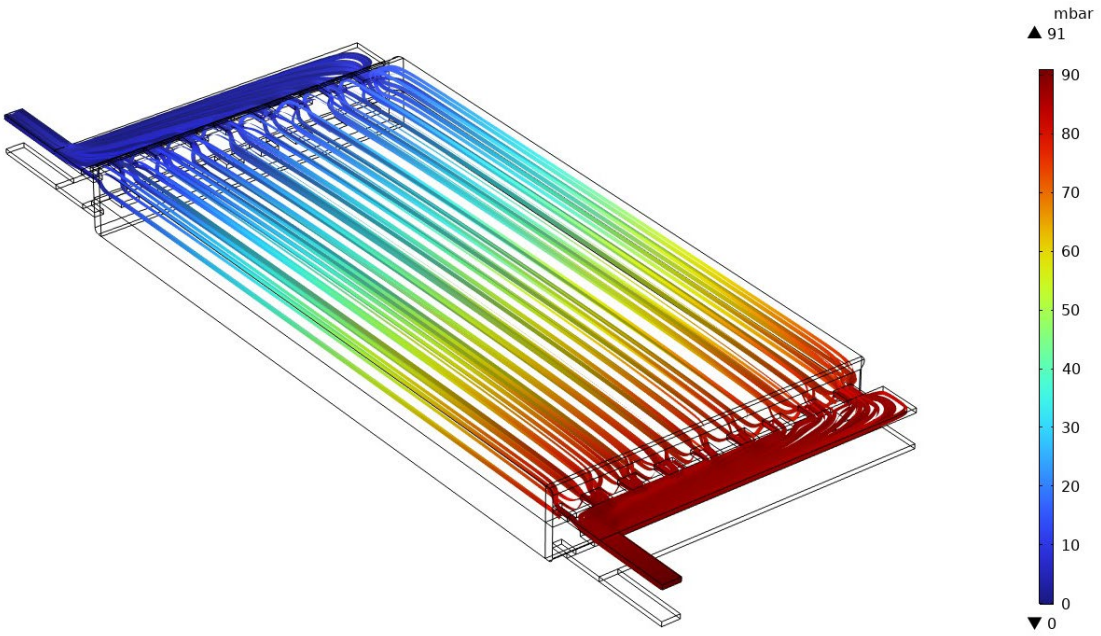

Figure 4.2.1 – Half-cell section with the flow field representation in the negative electrode at a flow rate of 20ml/min.

As predictable, the flow field in the cell is very simple and linear. After the inlet collectors, the fluid is rapidly distributed uniformly throughout the thickness of the electrode, visible in Figure 4.2.2. This makes the velocity field extremely linear, as just explained in Section 3.4.3.

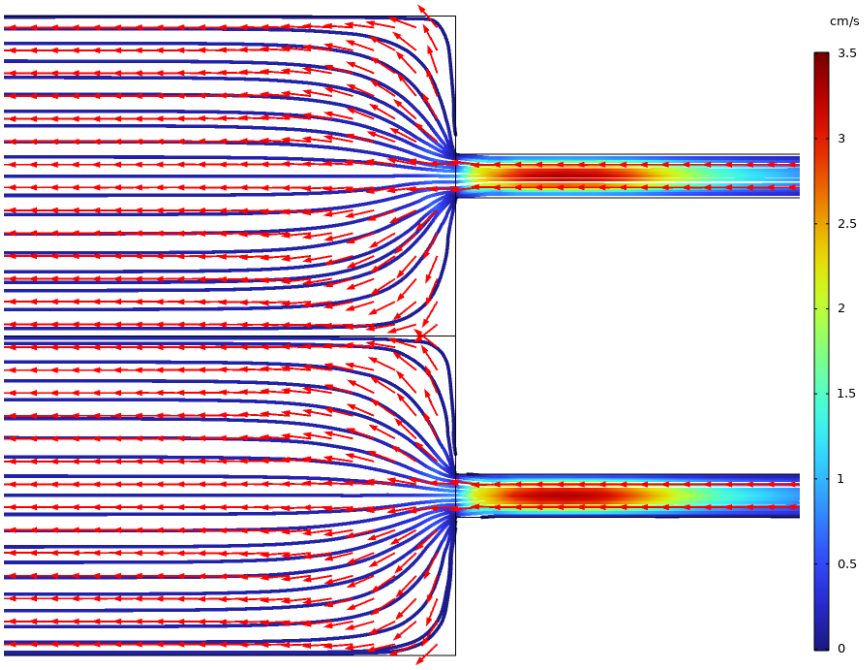

Figure 4.2.2 – Velocity streamline in a y-z cut-plane. The velocity distribution become homogeneous in the first mm of the electrode length.

The pressure losses values for the flow rates of 20 and 80 ml/min are reported in Table 4.2 where a comparison with laboratory data is made. As specified in Section 4.1.2 the SOC of the cell is assumed to be 50. It is important to specify the SOC for the fluid dynamic response because the electrolyte viscosity and density change in function of the state of charge.

	Model Results		**Experimental Data**	
	20 ml/min	80ml/min	20 ml/min	80 ml/min
Positive Half-Cell ΔP [mbar]	91	341	88	337
Negative Half-Cell ΔP [mbar]	81.5	324	81	315

Table 4.2 - Pressure losses in the cell for the positive and negative electrodes at different flow rates for a SOC 50.

From Table 4.2 it is possible to observe how the values of pressure losses are coherent with the experimental data. This indicates the goodness of the fluid dynamic physic implementation as the correct estimation of the permeability parameter. Little discrepancies can be due for measurements errors as other pressure losses due to roughness of the electrolyte collectors not implemented in the model. However, these differences do not influence significantly in the electrochemistry response.

4.2.2. Validated Results

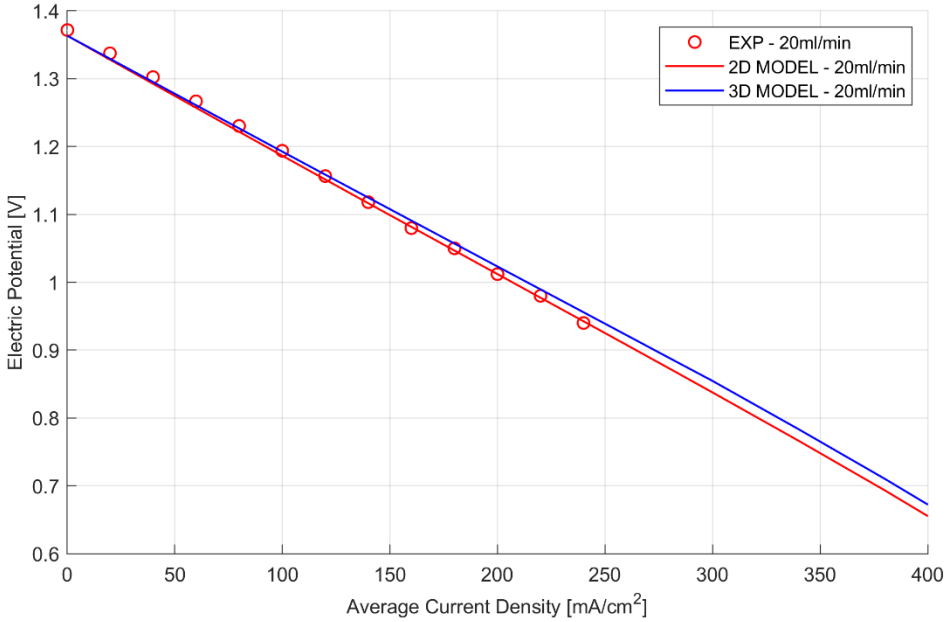

Figure 4.2.3 – Polarization curve comparison between the 2D and 3D model and Experimental data.

In Figure 4.2.4 are represented the polarization curves obtained for the 2D and 3D model of the FTFF cell. It is possible to observe a little difference for higher current densities with the 3D model who overestimates the cell voltage. This difference can be due for the 3D implementation of the flow field, while in the 2D model this is assumed to be constant. However, this overestimation does not mean lower model accuracy because for higher current densities also the measurements procedure (section 4.1.3) presents lower accuracy.

The error between the two model at the higher current density considered results about the 1,5%, so acceptable for the goal of this work.

The distribution the potentials, for the value of 100 mA/cm^2 are plotted in Figure 4.2.4 and Figure 4.2.5, where a comparison with the 2D model is made, the distribution of the overpotential and of the reactants concentration is plotted in Figure 4.2.6 and Figure 4.2.7. Concerning these last results, a comparison with the 2D model can be performed looking at Figure 4.1.10 and Figure 4.1.13, concluding very small acceptable discrepancies.

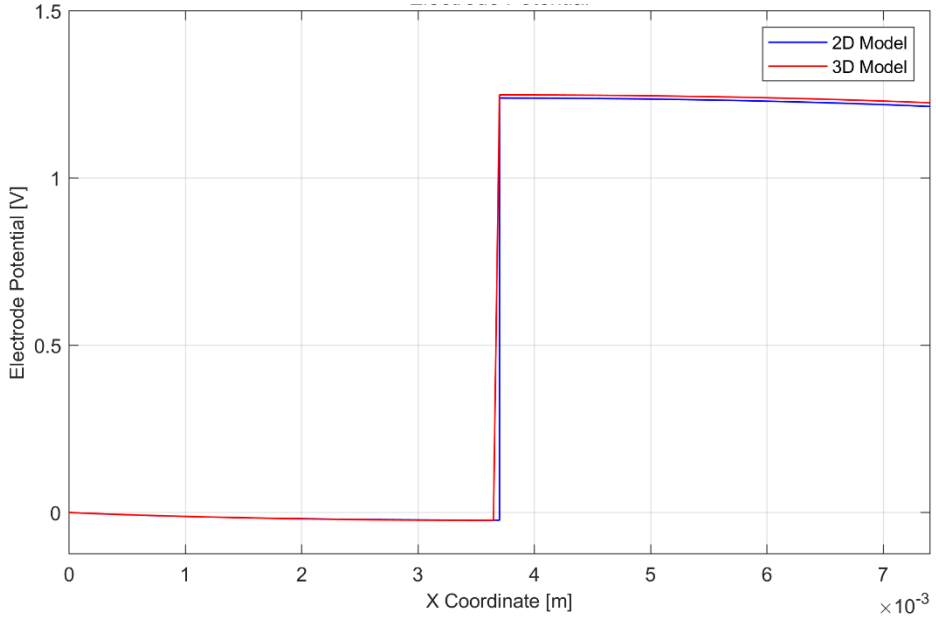

Figure 4.2.4 Electrode potential comparison between 2D and 3D model; 20ml/min, 100 mA/cm².

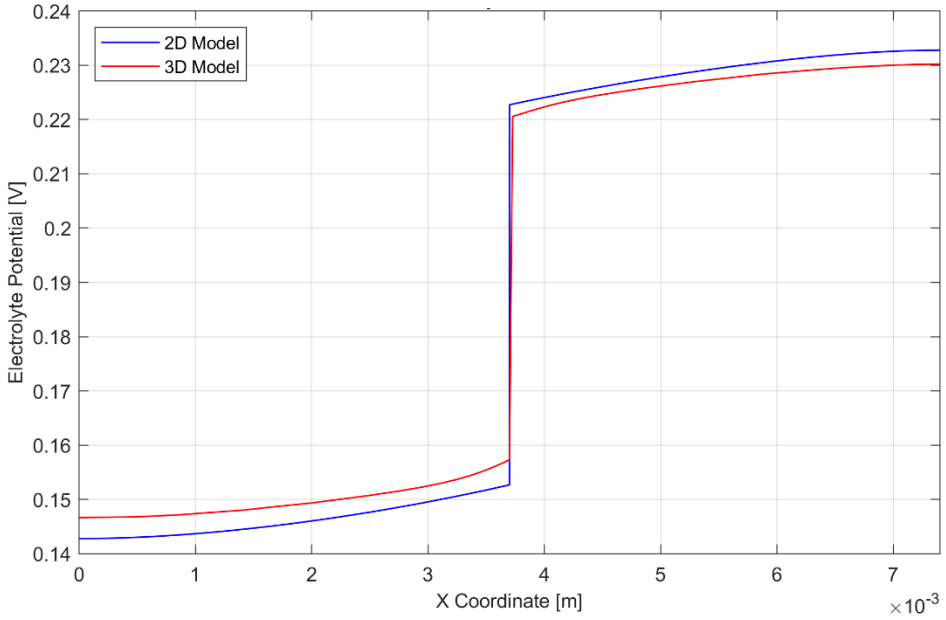

Figure 4.2.5 – Electrolyte potential comparisons between 2D and 3D model; 20ml/min, 100 mA/cm².

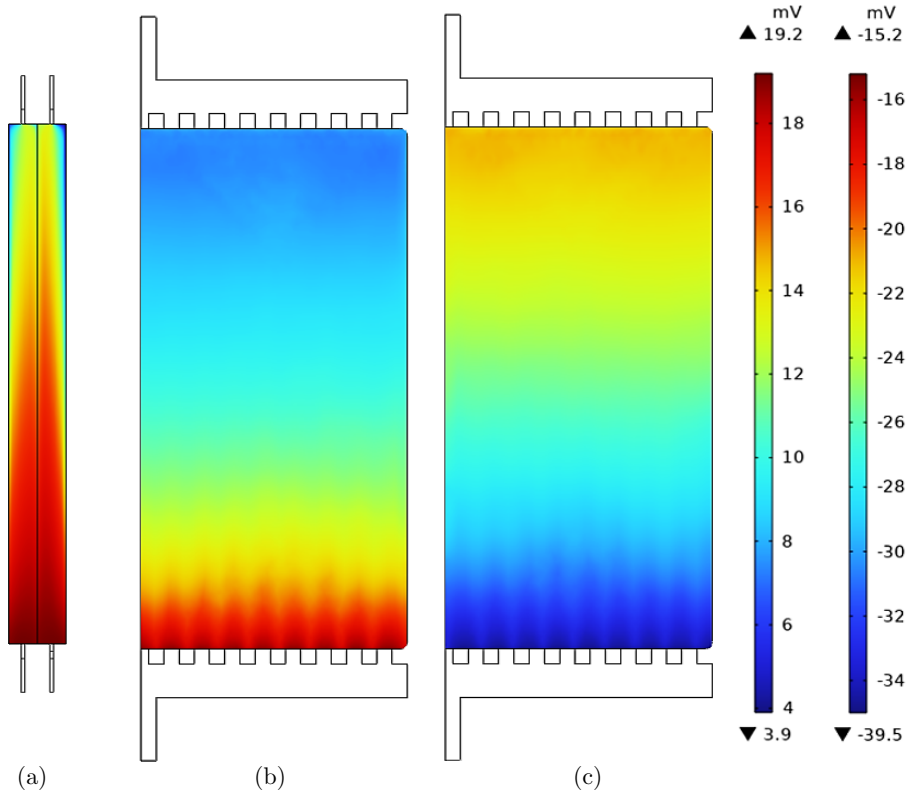

Figure 4.2.6 – Overpotentials at half-cell symmetry walls (a), negative (b) and positive (c) electrodes surfaces at half-electrode thickness cut-plane; 20ml/min, 100 mA/cm².

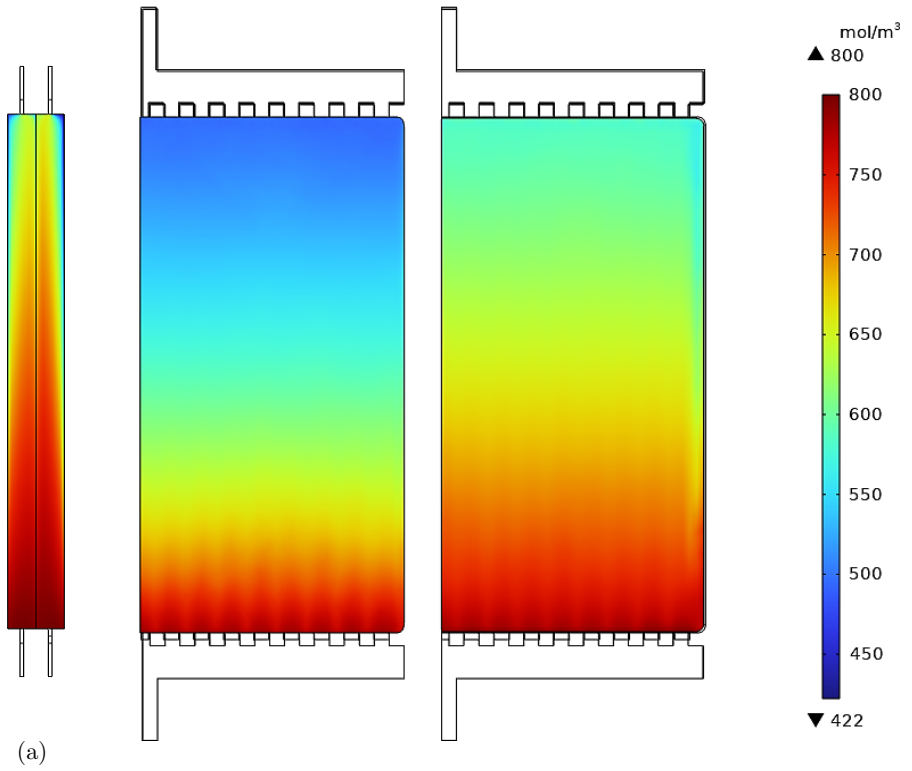

Figure 4.2.7 - V2 and V5 concentration at half-cell symmetry walls (a), negative (b) and positive (c) electrodes surfaces at half-electrode thickness cut-plane; 20ml/min, 100 mA/cm²

4.3. Mesh Sensitivity Analysis

In these multiphysics models, the accuracy of numerical results heavily relies on the discretization of the computational domain. One critical aspect of this discretization is the mesh, which divides the domain into smaller, finite elements or cells. The resolution and quality of this mesh profoundly impact the fidelity and reliability of simulations, particularly in complex systems such as vanadium redox flow batteries (VRFBs). This section investigates the sensitivity of VRFB modeling to mesh parameters, aiming to optimize computational efficiency while maintaining accuracy. For this, a systematic investigation into the sensitivity of VRFB simulations to mesh parameters is conducted to evaluate its impact on model predictions, finding the best discretization for the models.

4.3.1. Meshing

The meshing process has been performed differently for the 2D and 3D model.

For the 2D model, a structured mesh has been adopted, for the simplicity of the geometry. This allows to perform a better mesh sensitivity analysis and to have a better control on the mesh quality.

For the 3D model an unstructured mesh self-built by COMSOL has been used with corner refinement in the domain edge and boundary layers elements in the domain boundaries.

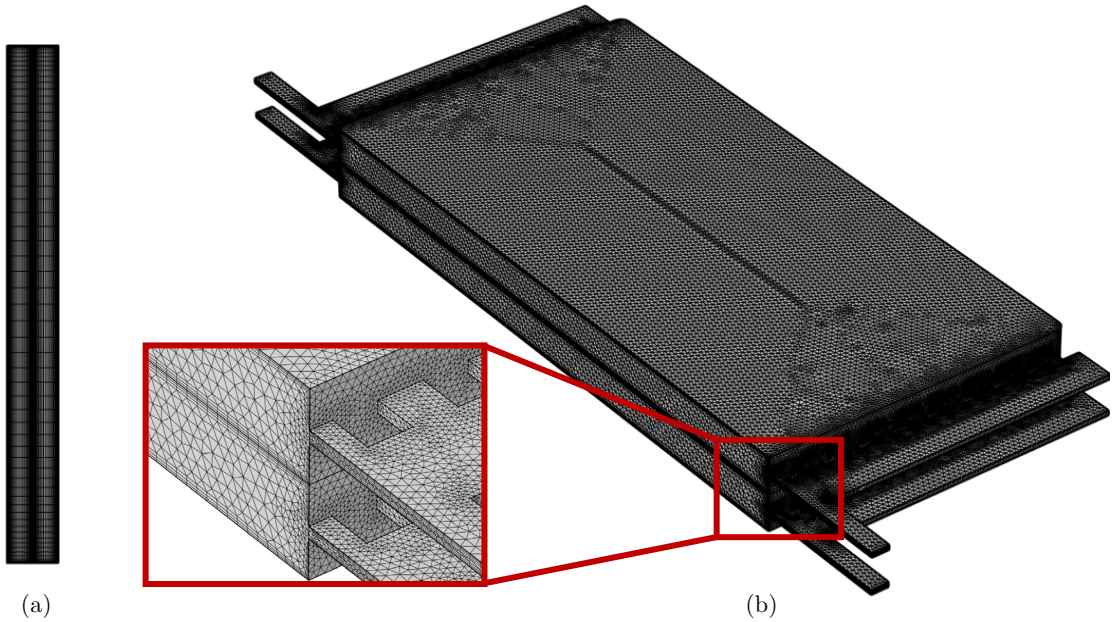

Figure 4.3.1 – Model mesh; (a) 2D model structured mesh, (b) 3D model mesh.

4.3.2. 2D Response

Regarding the 2D model, the fluid dynamic response in terms of pressure at half-cell is plotted in function of the number of elements in Figure 4.3.2. The number of elements selected for the mesh is set to have a discretization error lower than 0.1%.

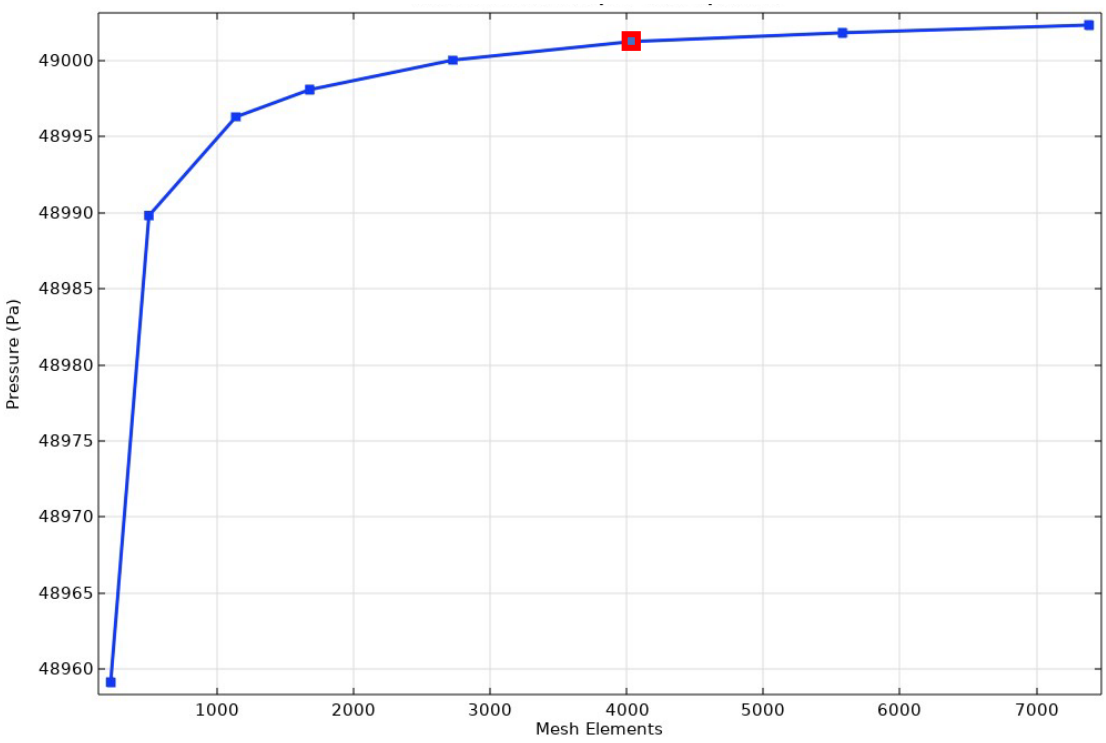

Figure 4.3.2 - Mesh refinement analysis for the 2D fluid dynamic response. The square in red indicates the number of elements selected.

Regarding the electrochemistry response, the number of elements of the mesh is considered in function of the current density as reported in Figure 4.3.3.

In the 2D model it is evident how the simple geometry of the cell ensures a very small range of variation of the current density for a further increase of the mesh elements number. For the very low computational burden has been chosen 4000 elements for the modelling of the cell to ensure a completely negligible error and to avoid results interpolation of the fluid dynamic study in the electrochemistry study mesh having the same mesh elements number.

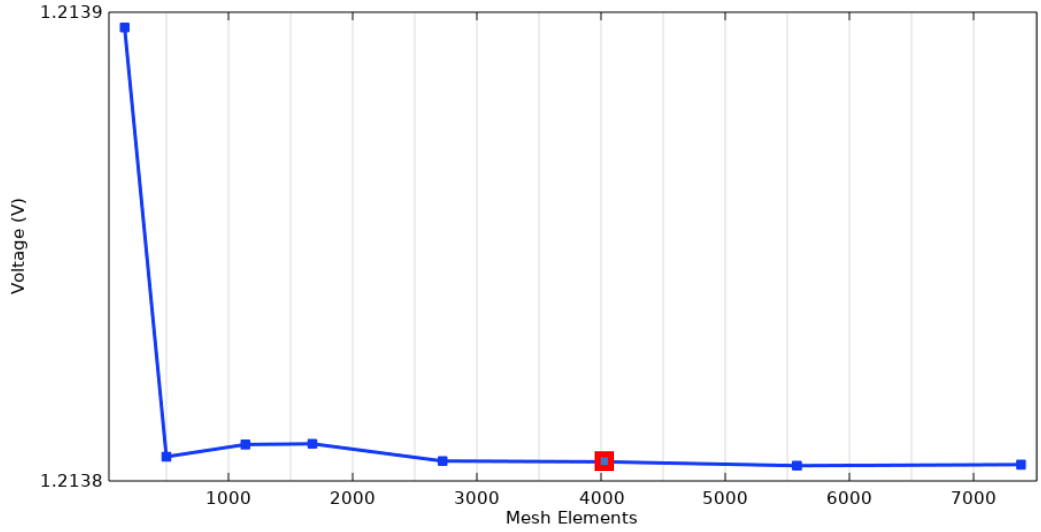

Figure 4.3.3 - Mesh refinement analysis for the electrochemistry response at 1000 A/m2. The square in red indicates the number of elements selected.

With this elements number the resolution time is in the average about 20 seconds per point and 4GB RAM required.

4.3.3. 3D Response

Regarding the 3D model, the fluid dynamic response and the electrochemistry response are analyzed in Figure 4.3.4 and Figure 4.3.5. The number of elements selected for the mesh is set to have, as for the 2D model, a discretization error lower than 0.1%.

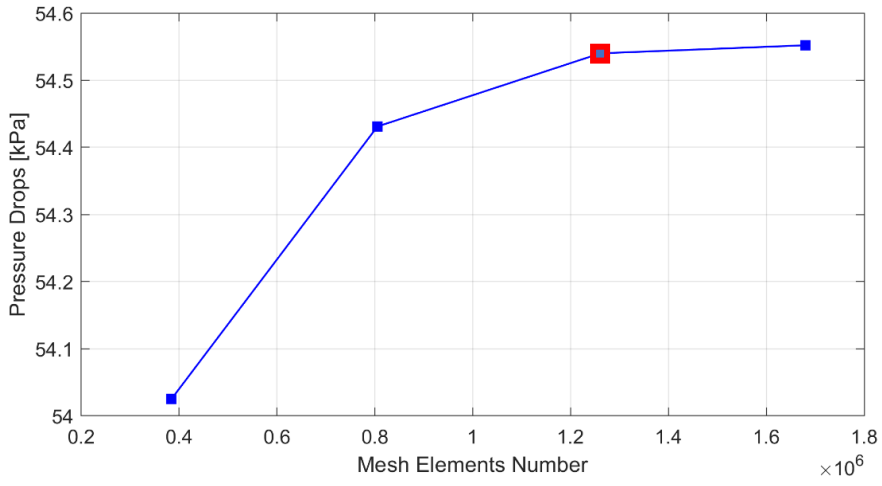

Figure 4.3.4 - Mesh refinement analysis for the 3D fluid dynamic response at 20ml/min. The square in red indicates the number of elements selected

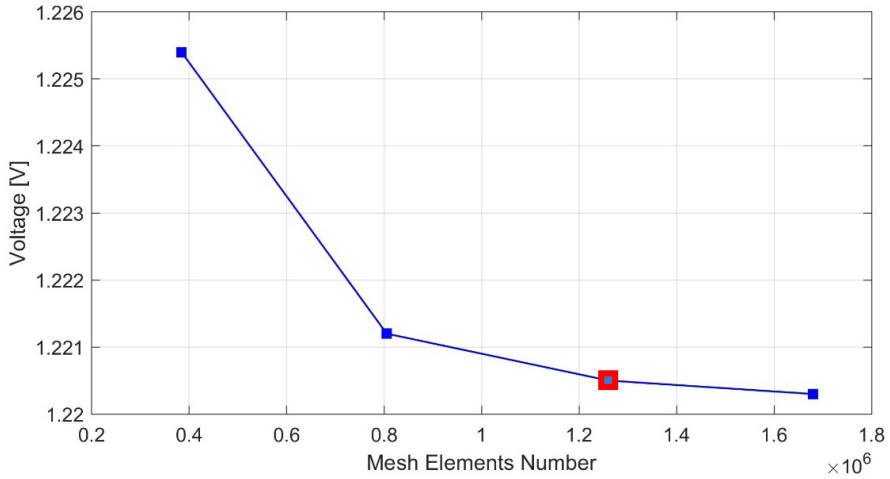

Figure 4.3.5 - Mesh refinement analysis for the 3D electrochemistry response at 100mA/cm², at 20ml/min. The square in red indicates the number of elements selected

With this elements number the resolution time is in the average about 720 seconds per point and 21GB RAM required.

4.4. Chen et Al Model Validation

4.4.1. Interdigitated Flow Field

To assess the validation of the model across different cell configurations, a comparison was made with the model by Chen et al. [19], which focuses on an Interdigitated Flow Field (IDFF) cell configuration. In IDFF configurations, the electrolyte flows through alternating channels created by sets of mesh-like electrodes arranged on either side, offering distinct advantages over the Flow Through (FT) configuration used in previous chapters for model validation:

- Enhanced Efficiency: IDFF design typically improves electrolyte utilization and achieves higher power density by maximizing the electrode-electrolyte interface area, enabling more efficient electrochemical reactions.
- Improved Mass Transport: This design facilitates better transport of electrolyte ions, minimizing concentration gradients within the cell and improving overall performance.
- Higher Energy Density: Due to increased efficiency and optimized use of active materials, IDFF configurations often result in higher energy density compared to FT cell designs.

Generally, interdigitated flow fields offer better performance in terms of efficiency, power density, and energy density but are more complex to manufacture and may require more careful maintenance.

The 3D geometry of the cell with IDFF analyzed in Chen et Al model is reported in Figure 4.4.1.

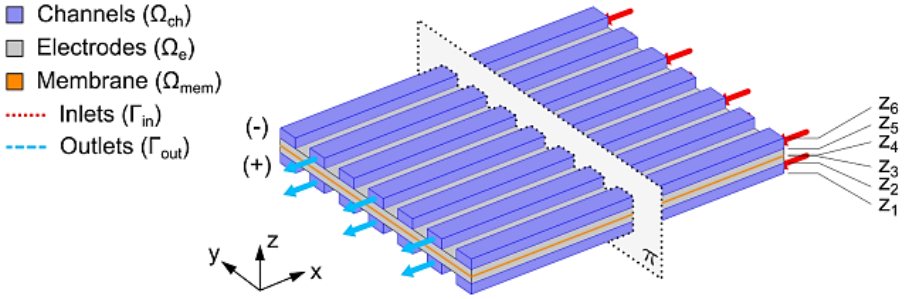

Figure 4.4.1 - Geometry of the cell with IDFF used in Chen et Al model.

The geometry parameters of the cell are reported in Table 4.3.

Symbol	Description	Value
L	Length of the electrode	16 mm
W	Width of the electrode	13 mm
$\mathbf{w_{ch}}$	Channel width	1 mm
$\mathbf{w_{rib}}$	Rib width	1 mm
$\mathbf{H_{ch}}$	Channel thickness	0.5 mm
$\mathbf{H_e^-}$	Negative electrode thickness	3.1496×10^{-4} m
$\mathbf{H_e^+}$	Positive electrode thickness	3.0988×10^{-4} m
$\mathbf{H_{mem}}$	Membrane thickness	50.8 μm

Table 4.3 – Geometric parameters of the IDFF cell.

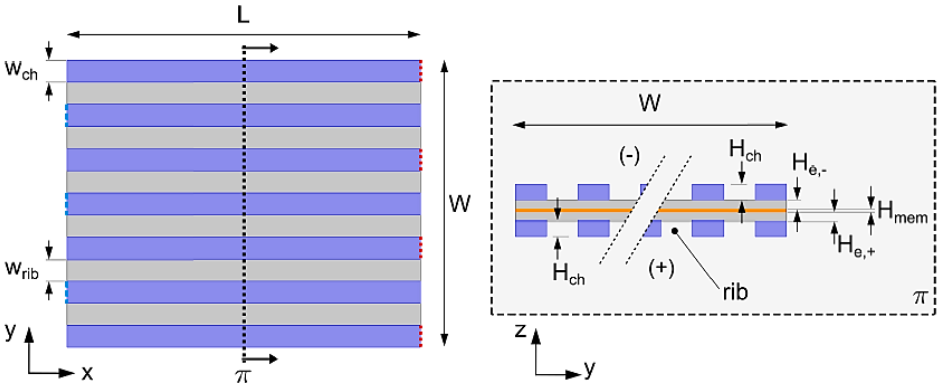

Figure 4.4.2 – Geometric representation of the cell used in the model.

4.4.2. Assumptions and Boundary Conditions

The model's assumptions remain consistent with those detailed in Section 3.4.1. However, in this scenario, the flow field significantly influences the cell's performance, acting as a crucial boundary condition.

The boundary conditions for the flow field, following the guidelines suggested in the reference, involve setting the inlet and outlet pressures of the collectors. To accurately determine the pressure values at the inlet and outlet of the channels for a 2D simulation, a comprehensive 3D simulation was conducted. This simulation allowed for the extraction of streamlines, which facilitates an analysis of the fluid's flow path, as depicted in Figure 4.4.3. Based on the reference, the pressure values at the inlet and outlet of the channel are established for a flow rate of 10ml/min, ensuring that these crucial parameters are accurately reflected in the model to predict cell performance effectively. These pressures values are:

$$p_{in} = 1506\ Pa$$

$$p_{out} = 0\ Pa$$

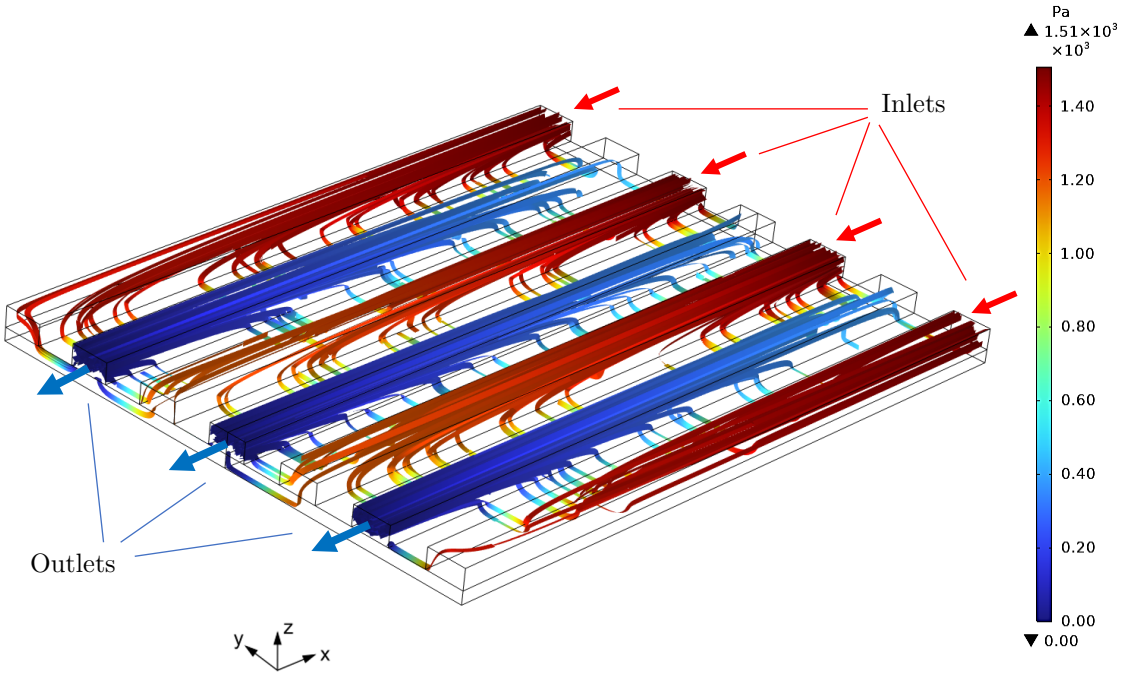

Figure 4.4.3 – 3D view of the streamline indicating the electrolyte flow path from the inlet and the outlet, with a flow of 10ml/min.

The pressure value at the outlet boundaries for the 2D simulation corresponds to an x-averaged 3D model pressure is reported in Figure 4.4.4 .

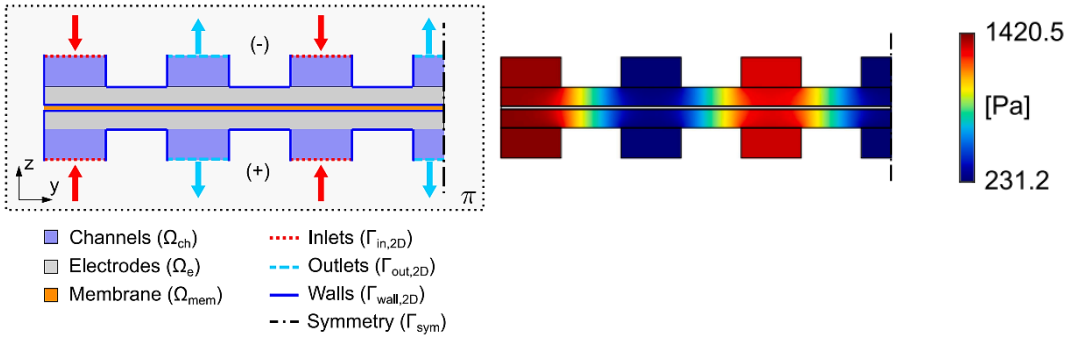

Figure 4.4.4 – Representation of the computational domain for the 2D simulation and of the pressure boundary conditions assumed after the full 3D fluid dynamic simulation.

Concerning the current collector, instead to applicate a current boundary condition, according with Chen reference is preferred and more realistic to assume a potential boundary condition ate the rib-electrode interfaces. This comports a difference in the distribution of the currents in the rib-electrode interfaces. So, to use the average current as boundary condition should require to model the entire current collector.

4.4.3. Polarization Curves Comparisons

The polarization curve obtained are reported in Figure 4.4.5 and Figure 4.4.6. The higher discrepancy is verified at the OCV conditions, coherently with that reported in the reference. This discrepancy can be attribute to the assumption of unitary activity coefficients. For the other points the curve present an excellent fit with the experimental datas, both for the 2D and 3D model.

The computational time for the 2D and 3D simulation and the memory required are here reported:

- 2D Model: Mesh Element Number: 28 000, Solution time per point: 21seconds; Memory: 11GB RAM;
- 3D Model: mesh element Number: 2 729 000; Solution time per point: 18 min, Memory: 44 GB RAM;

In this case, differently from the laboratory cell, the mesh elements number has been taken equal to that declared in the paper, where the mesh refinement analysis has been performed. It is possible then to assume the number of elements of the mesh acceptable for a negligible numerical error.

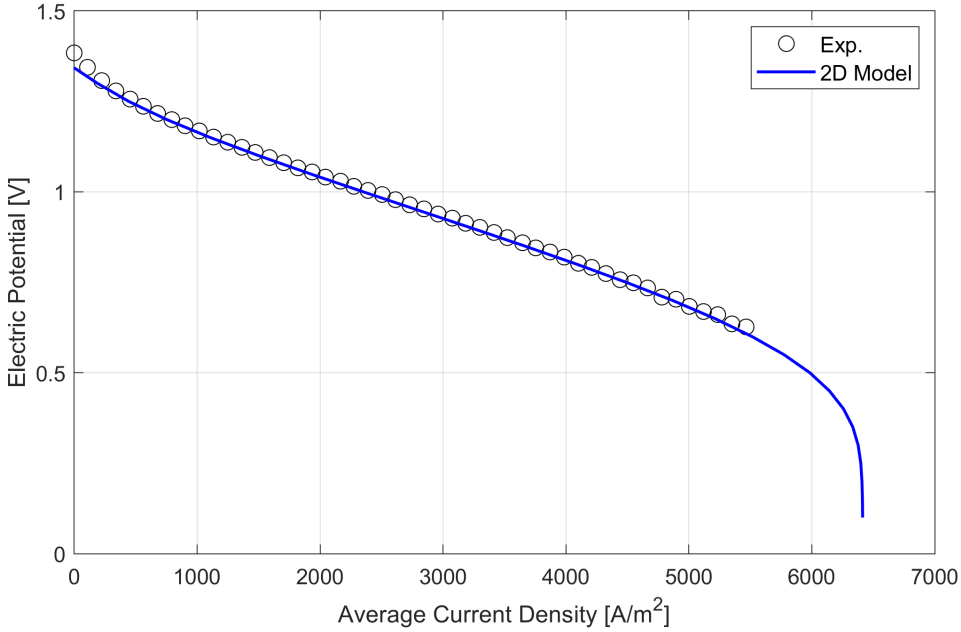

Figure 4.4.5 – Polarization Curve of the 2D model vs Extrapolated Experimental data.

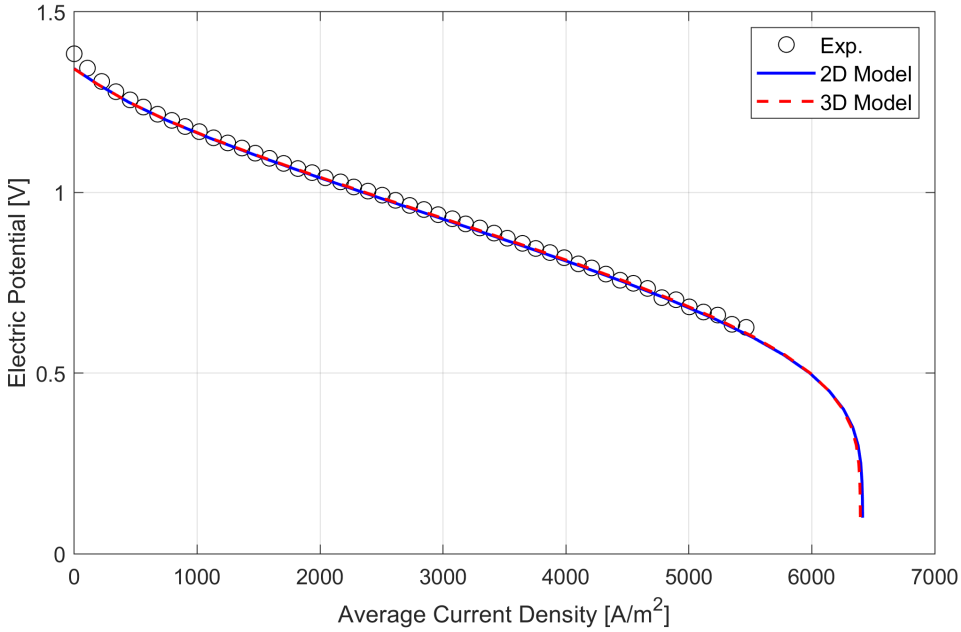

Figure 4.4.6 - Polarization Curve of the 2D and 3D model vs Extrapolated Experimental data.

It is possible to observe in Figure 4.4.6 how the 3D model perfectly fit the experimental data together with the 2D model.

4.4.4. 2D Model Results Comparisons

To ensure a comprehensive validation of the model, this section presents more detailed results. Concerning the flow field, a further comparison is reported in Figure 4.4.7 and Figure 4.4.8 where the close alignment between the two flow fields is clearly demonstrated, showing an almost perfect match.

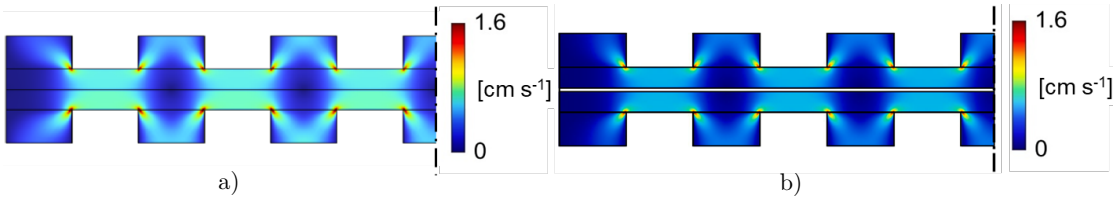

Figure 4.4.7 - Velocity field in z-y direction, of the 2D model (a) and Chen et Al model (b); 10ml/min

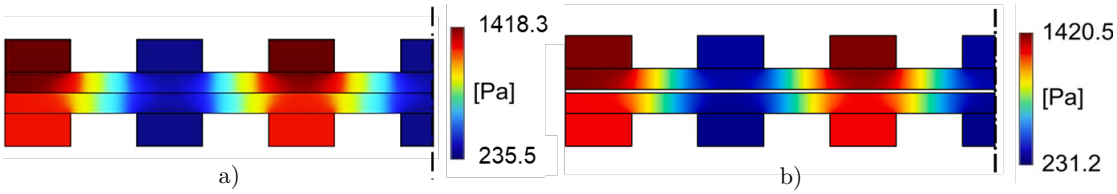

Figure 4.4.8 - Pressure magnitude of the 3D model (a) and Chen et Al model (b); 10ml/min

The distribution of reactants and the potentials results and their comparisons with that of the Chen model are reported in Figure 4.4.9, Figure 4.4.10, Figure 4.4.11 and Figure 4.4.12.

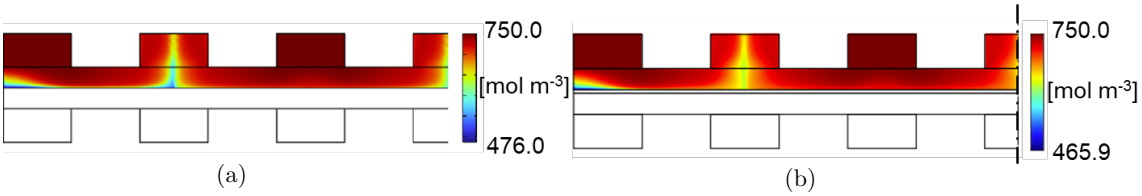

Figure 4.4.9 – V2 concentration of the 2D model (a) and Chen et Al model (b); 0.9 V 10ml/min.

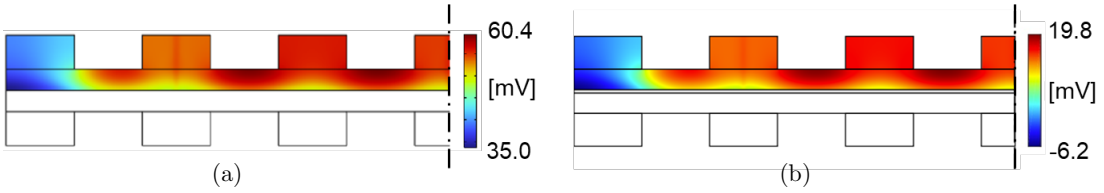

Figure 4.4.10 – Electrolyte potential of the 2D model (a) and Chen et Al model (b); 0,9V 10ml/min.

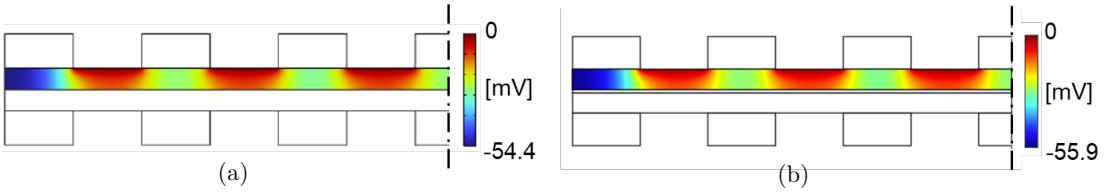

Figure 4.4.11 - Electrode potential of the 2D model (left) and Chen et Al model (right); 0,9V 10ml/min.

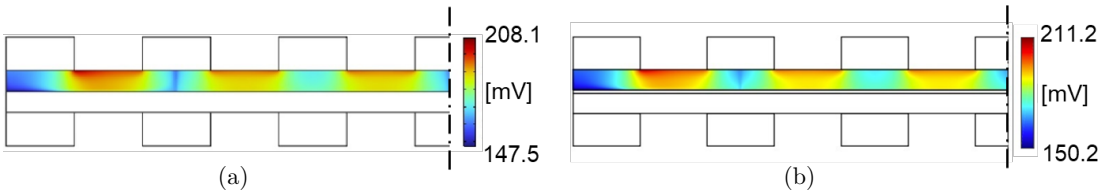

Figure 4.4.12 – Overpotential of the 2D model (left) and Chen et Al model (right); 0,9V 10ml/min.

A further comparison between the results displayed in Figure 4.4.10 show a good agreement between the two models.

A little discrepancy between the results can be observed on the potential of the liquid phase. However, this can be acceptable because both the value of overpotential and electric potential exactly matches in the two models. Indeed, the difference in the electrolyte potential is strictly related to the equilibrium potential as reported in equation 3.2.14 and 3.2.15, which can be expressed in the general form as:

$$E_{eq} = \phi_s - \phi_l - \eta \tag{4.4.1}$$

Because both the overpotential η and the solid phase potential ϕ_s perfectly matches the reference results, the cause of the discrepancy could be due by a different calculation of the equilibrium potential or to a different implementation of the Donnan potential at the membrane. However, the OCV of the cell calculated by the model match that of the reference: this consistency supports the conclusion that the error can be deemed acceptable, especially in the absence of additional parameters for comparison.

4.4.5. 3D Model Results Comparisons

In Figure 4.4.13 and Figure 4.4.14 are reported the results about the velocity magnitude in the zy direction and the pressure magnitude of the cell, compared with the results of the Chen model. The results depicted in these figures demonstrate a strong alignment, showing that our model's results are in good agreement with those from the Chen model, as well as with the outcomes of the 2D model illustrated in Figure 4.4.7 and Figure 4.4.8.

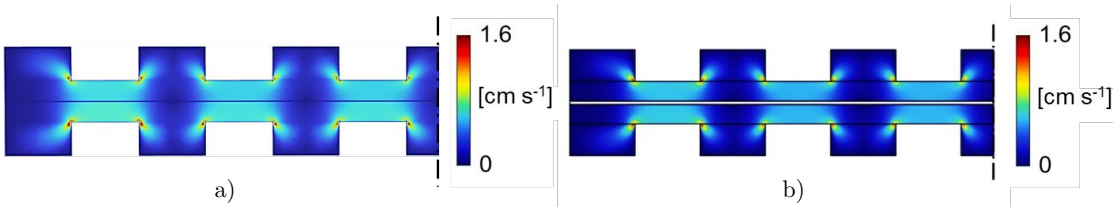

Figure 4.4.13 - Velocity field in z-y direction, of the 3D model (a) and Chen et Al model (b); 10ml/min

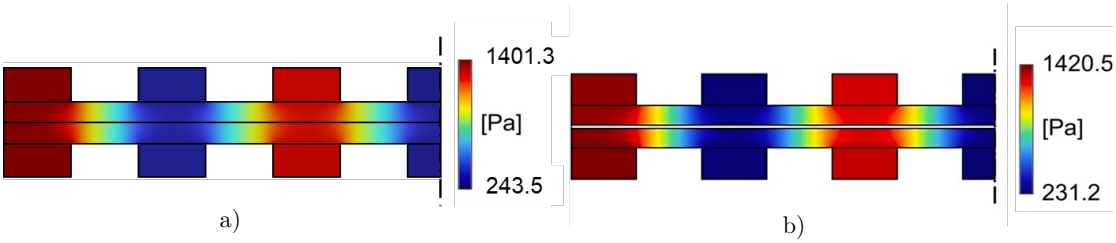

Figure 4.4.14 – Pressure magnitude of the 3D model (a) and Chen et Al model (b); 10ml/min.

The distribution of reactants and the potentials and their comparisons with the results of the Chen model are reported in Figure 4.4.15, Figure 4.4.16, Figure 4.4.17, Figure 4.4.18.

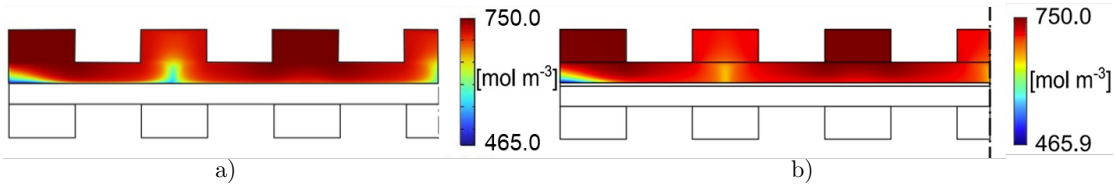

Figure 4.4.15 - V2 concentration of the 3D model (a) and Chen et Al model (b); 0,9V 10ml/min.

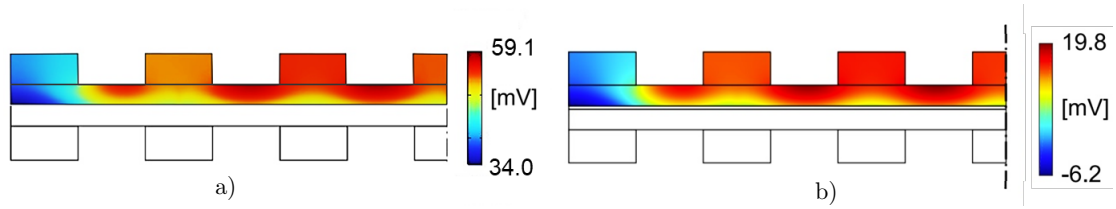

Figure 4.4.16 - Electrolyte potential of the 3D model (a) and Chen et Al model (b); 0,9V 10ml/min.

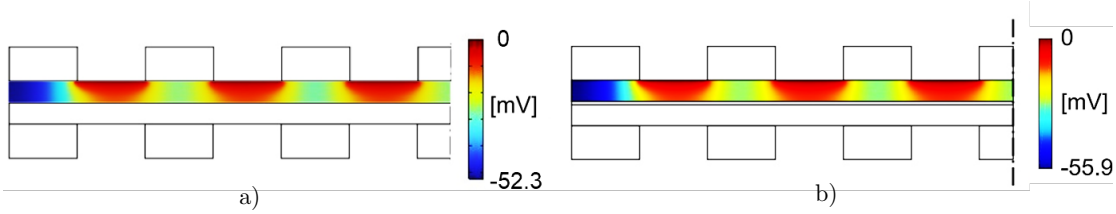

Figure 4.4.17 - Electrode potential of the 3D model (a) and Chen et Al model (b); 0,9V 10ml/min.

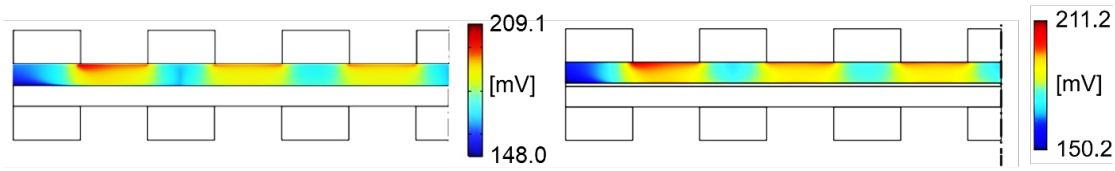

a) b)

Figure 4.4.18 - Overpotential of the 3D model (a) and Chen et Al model (b); 0,9V 10ml/min.

Also for the 3D model analysis, a slight discrepancy was noted in the liquid phase potential. As previously discussed, this deviation can be deemed acceptable due to its consistent offset from the reference results across various voltage values. This consistency suggests that the discrepancy is systematic and could potentially be attributed to specific modeling assumptions or simplifications.

Chapter 5

Conclusions

The final chapter aims to distill the essence of the findings, reflections, and the forward path carved out by this research. In this work, it is explored in deep the intricacies of Vanadium Redox Flow Batteries (VRFBs) modelling, looking their potential and challenges. This concluding chapter seeks to encapsulate the key insights gained, the significance of the contributions made to the field of energy storage, and to ponder the implications of these findings for future research and technological advancement.

5.1. Conclusions

This master's thesis represents a comprehensive effort to model and understand the complex physical and electrochemical processes occurring within Vanadium Redox Flow Batteries (VRFBs) using the COMSOL Multiphysics software. The study embarked on an ambitious journey to bridge the gap between theoretical models and practical, experimental validations, focusing on the detailed simulation of VRFBs through both 2D and 3D modeling approaches.

The initial phase of this work involved developing a 2D model of the VRFB system to manage computational complexity and resource demands efficiently. This model was instrumental in identifying critical parameters affecting VRFB performance, such as electrolyte flow rates, electrode porosity, and membrane conductivity. Despite its inherent simplifications, the 2D model offered valuable insights into the general behavior of VRFBs under various operational scenarios, facilitating a preliminary understanding of the interplay between electrochemical reactions and fluid dynamics within the system. This phase also served as a testing ground for hypotheses and modeling approaches, laying the groundwork for more sophisticated simulations.

Building upon the foundational knowledge gained from the 2D simulations, the study advanced to the development of a comprehensive 3D model. This model aimed to capture the full complexity of VRFB geometry, including the detailed architecture of flow fields, electrode structure, and the distribution of reactants and products within the cell. The 3D simulations provided a deeper understanding of the spatial variations

in species concentration, potential distribution, and the impact of geometric design on flow distribution and battery efficiency.

A pivotal aspect of this thesis was the rigorous validation of the developed models against experimental data. This validation process involved comparing simulation results with experimental measurements obtained from laboratory-scale VRFB cells, focusing on key performance indicators such as polarization curves. The experimental setup included a flow-through cell configuration enabling a comprehensive assessment of the models' accuracy in predicting VRFB behavior under varied operating conditions.

The validation process undertaken in this study was both rigorous and comprehensive, addressing initial disparities between model predictions and experimental data through a series of calibration steps. These adjustments were critical in refining the model's accuracy and ensuring its alignment with observed behaviors. Initially, discrepancies in the model's outputs necessitated a thorough evaluation, which led to the identification and incorporation of several key modifications to more accurately capture the dynamics of the system.

Significant among these modifications was the application of the Bruggeman correction, which enhanced the model's ability to accurately simulate the electrolyte conductivity, thereby improving the correlation with experimental findings. Furthermore, a detailed analysis of mass transfer phenomena was incorporated, offering a more nuanced understanding of reactant and product movements within the cell. This inclusion proved essential in replicating the complexities of real-world operation. Additionally, the model underwent refinement to account for the effects of contact resistance, an aspect previously overlooked. Recognizing the impact of contact resistance on overall cell performance allowed for a more comprehensive representation, particularly in terms of voltage losses and efficiency metrics.

Moreover, the validation of the model with a reference cell with a completely different geometry has permitted to affirm the robustness of the assumption and of the correction implemented in the model for the validation with the experimental data acquired.

The models exhibited a high degree of congruence with experimental observations, affirming the reliability of the simulations in replicating the nuanced dynamics of VRFB systems. This validation not only underscored the fidelity of the models but also enhanced confidence in their applicability for future research and development endeavors.

The work presented in this thesis offers significant contributions to the field of energy storage and VRFB technology. By developing and validating detailed 2D and 3D models, this study provides a robust platform for exploring the effects of design modifications, operational strategies, and material properties on VRFB performance. The insights garnered from this research have the potential to inform the design of more efficient, durable, and cost-effective VRFB systems, supporting the broader integration of renewable energy sources into the global energy mix.

Moreover, the methodologies and findings of this thesis contribute to the growing body of knowledge in electrochemical system modeling, offering valuable reference points for future studies in this domain. The successful validation of the models against experimental data reinforces the importance of integrating theoretical simulations with empirical research, paving the way for more informed and targeted advancements in battery technology.

In sum, this master's thesis encapsulates a significant step forward in the modeling and understanding of VRFB systems, leveraging the capabilities of COMSOL Multiphysics to bridge theoretical knowledge with practical applications. The detailed exploration of 2D and 3D modeling, coupled with rigorous experimental validation, marks a noteworthy contribution to the field, laying the groundwork for future innovations in VRFB design and optimization.

5.2. Futures Developments

The journey embarked upon in this master thesis, centering on the development and validation of a comprehensive 2D and 3D modeling framework for Vanadium Redox Flow Batteries (VRFBs) within COMSOL Multiphysics, has laid a solid foundation for understanding the intricate balance between electrochemistry and fluid dynamics in these energy storage systems. As we project into the future, several developmental avenues appear ripe for exploration. These avenues not only promise to extend the robustness and applicability of our current models but also aim to tackle some of the most pressing challenges and opportunities in the optimization and scaling of VRFB technology.

A natural progression from the current work is the scaling of the model from a single-cell configuration to a multi-cell stack. This scale-up is crucial for capturing the collective behavior of cells in a real-world VRFB system, where multiple cells are connected in series and parallel to meet desired energy and power outputs:

- Stack-Level Modeling: Developing a stack-level model involves complex considerations, including the interactions between cells, the management of fluid flow across cells, and the thermal dynamics that arise from the stack operation. This comprehensive modeling will require an advanced understanding of the electrical connections between cells, the uniform distribution of electrolyte flow, and the dissipation of heat generated during operation.
- Shunt Currents Simulation: An important aspect of stack-level modeling is the accurate simulation of shunt currents. Shunt currents, unwanted electrical pathways that can bypass the electrochemical reaction sites, lead to efficiency losses and uneven cell aging. Including shunt current dynamics in the stack model will be essential for predicting performance degradation and for designing mitigation strategies.

With a more detailed and scalable model at hand, the next step involves the integration of advanced optimization procedures. These procedures will be aimed at refining the VRFB design and operation to achieve optimal performance, longevity, and cost-efficiency:

- Design and Geometry Optimization: Utilizing optimization algorithms to explore the vast design space of cell geometry, electrode configurations, and flow field patterns. The goal is to identify designs that maximize energy efficiency, minimize pressure drops, and ensure uniform flow distribution and electrolyte utilization.
- Operational Parameter Optimization: Applying optimization techniques to the operational parameters of the VRFB, such as charge/discharge rates, flow rates, and temperature settings. This will help in identifying the optimal operating conditions that balance performance, efficiency, and the longevity of the battery.
- Material Optimization: Considering the advancements in material science, there is a continuous opportunity to optimize the materials used for electrodes, membranes, and electrolytes. Material optimization can lead to improvements in energy density, reduce crossover, enhance ion transport, and increase the overall efficiency and durability of the VRFB.

Future models should also aim to incorporate real-world operating conditions more comprehensively. This includes the simulation of VRFBs under transitional load conditions, the impact of environmental temperatures, and the integration of VRFB systems with renewable energy sources. Understanding how these external factors

influence VRFB performance is critical for the development of more resilient and adaptable energy storage solutions.

The modeling work presented in this thesis represents a significant step forward in the understanding and optimization of VRFB technology. However, the path ahead is filled with opportunities for further advancements. By scaling the models to reflect the complexity of stack-level operations, incorporating the nuances of shunt currents, and leveraging advanced optimization techniques, it will be possible to move closer to realizing the full potential of VRFB systems. These future developments will not only enhance the fidelity and applicability of our models but also contribute to the broader adoption and optimization of VRFBs in the global energy landscape.

5.3. Final Considerations

In concluding this research it's clear that this work extends beyond the technical achievements of refining a Vanadium Redox Flow Battery (VRFB) model. The methodology, with its detailed focus on calibration and adjustment, has not only aimed at enhancing the model's accuracy but also at deepening our understanding of the physical phenomena that dictate the behavior of VRFBs. This process reflects a broader scientific goal: to align theoretical models more closely with the realities of the natural world.

The effort to validate and improve the VRFB model underscores the importance of continuous inquiry and adaptation in scientific research. Each step of model refinement serves as a reminder of the complexity of physical systems. More importantly, it highlights the critical role of persistence and precision in uncovering the nuances of how such systems operate.

This research has not only contributed to the body of knowledge on VRFBs but also exemplified how scientific modeling can bridge the gap between theoretical predictions and experimental observations. Through this work, it has benn seen how a detailed and methodical approach can reveal insights into the mechanisms at play within electrochemical systems, offering potential pathways for innovation and improvement.

In essence, the journey of refining the VRFB model mirrors the broader endeavor of science to understand and harness the laws of nature. It reaffirms the value of rigorous scientific investigation and the potential of such endeavors to advance technology for practical applications. As we move forward, the insights gained from this study will undoubtedly fuel further exploration and innovation, driving us closer to sustainable energy solutions.

Acknoweldgments

This work was conducted at the Electrochemical Energy Conversion Laboratory (EESCoLab) of the University of Padua. I would like to express my deep gratitude to Professor Massimo Guarnieri and Andrea Trovò for giving me the opportunity to undertake this thesis. A special thanks also goes to all the laboratory staff who assisted and supported me during the execution of this project, particularly to Nicolò and Matteo, who have been essential points of reference. Furthermore, I would like to extend my thanks to Mirko d'Adamo, whose willingness and enthusiasm guided me on the right path to using COMSOL.

Finally, heartfelt thanks to all the people who, from the beginning of my master's degree at the University of Padua, have been important references, supporting and motivating me every day.

BIBLIOGRAPHY

[1] Z. Yang *et al.*, "Electrochemical Energy Storage for Green Grid," *Chem Rev*, vol. 111, no. 5, pp. 3577–3613, May 2011, doi: 10.1021/cr100290v.

[2] A. G. Olabi *et al.*, "Redox Flow Batteries: Recent Development in Main Components, Emerging Technologies, Diagnostic Techniques, Large-Scale Applications, and Challenges and Barriers," *Batteries*, vol. 9, no. 8, p. 409, Aug. 2023, doi: 10.3390/batteries9080409.

[3] Z. Qi and G. M. Koenig, "Review Article: Flow battery systems with solid electroactive materials," *Journal of Vacuum Science & Technology B, Nanotechnology and Microelectronics: Materials, Processing, Measurement, and Phenomena*, vol. 35, no. 4, Jul. 2017, doi: 10.1116/1.4983210.

[4] T. Puleston, A. Clemente, R. Costa-Castelló, and M. Serra, "Modelling and Estimation of Vanadium Redox Flow Batteries: A Review," *Batteries*, vol. 8, no. 9, p. 121, Sep. 2022, doi: 10.3390/batteries8090121.

[5] M. Skyllas-Kazacos and L. Goh, "Modeling of vanadium ion diffusion across the ion exchange membrane in the vanadium redox battery," *J Memb Sci*, vol. 399–400, pp. 43–48, May 2012, doi: 10.1016/j.memsci.2012.01.024.

[6] R. O'Hayre, S. Cha, W. Colella, and F. B. Prinz, *Fuel Cell Fundamentals*. Wiley, 2016. doi: 10.1002/9781119191766.

[7] C. Choi *et al.*, "Understanding the redox reaction mechanism of vanadium electrolytes in all-vanadium redox flow batteries," *J Energy Storage*, vol. 21, pp. 321–327, Feb. 2019, doi: 10.1016/j.est.2018.11.002.

[8] V. A. Danilov and M. O. Tade, "A new technique of estimating anodic and cathodic charge transfer coefficients from SOFC polarization curves," *Int J Hydrogen Energy*, vol. 34, no. 16, pp. 6876–6881, Aug. 2009, doi: 10.1016/j.ijhydene.2009.06.046.

[9] K. Knehr, E Agar, C. Dennison, A. Kalidindi, and E. Kumbur, "A Transient Vanadium Flow Battery Model Incorporating Vanadium Crossover and Water

Transport through the Membrane," *J. Electrochem*, vol. 159, no. 9, pp. A1446–A1459, 2012.

[10] A.A. Shah, M.J. Watt-Smith, and F.C. Walsh, "A dynamic performance model for redox flow batteries involving soluble species," *Electrochim. Acta*, vol. 53, pp. 8087–8100, 2008.

[11] K.W. Knehr and E.C. Kumbur, "Open circuit voltage of vanadium redox flow batteries: Discrepancy between models and experiments," *Electrochem. Commun*, vol. 13, pp. 342–345, 2011.

[12] M. Guarnieri, A. Trovò, A. D'Anzi, and P. Alotto, "Developing vanadium redox flow technology on a 9-kW 26-kWh industrial scale test facility: Design review and early experiments," *Appl Energy*, vol. 230, pp. 1425–1434, Nov. 2018, doi: 10.1016/j.apenergy.2018.09.021.

[13] K. W. Knehr, E. Agar, C. R. Dennison, A. R. Kalidindi, and E. C. Kumbur, "A Transient Vanadium Flow Battery Model Incorporating Vanadium Crossover and Water Transport through the Membrane," *J Electrochem Soc*, vol. 159, no. 9, pp. A1446–A1459, Jan. 2012, doi: 10.1149/2.017209jes.

[14] M. M. Tomadakis and T. J. Robertson, "Viscous Permeability of Random Fiber Structures: Comparison of Electrical and Diffusional Estimates with Experimental and Analytical Results," *J Compos Mater*, vol. 39, no. 2, pp. 163–188, Jan. 2005, doi: 10.1177/0021998305046438.

[15] D. Froning, J. Brinkmann, U. Reimer, V. Schmidt, W. Lehnert, and D. Stolten, "3D analysis, modeling and simulation of transport processes in compressed fibrous microstructures, using the Lattice Boltzmann method," *Electrochim Acta*, vol. 110, pp. 325–334, Nov. 2013, doi: 10.1016/j.electacta.2013.04.071.

[16] X. Ma, H. Zhang, and F. Xing, "A three-dimensional model for negative half cell of the vanadium redox flow battery," *Electrochim Acta*, vol. 58, pp. 238–246, Dec. 2011, doi: 10.1016/j.electacta.2011.09.042.

[17] K. Il Jeong, S. H. Lim, H. Hong, J.-M. Jeong, W. V. Kim, and S. S. Kim, "Enhancing Vanadium redox flow batteries performance through local compression ratio adjustment using stiffness gradient carbon felt electrodes," *Appl Mater Today*, vol. 35, p. 101928, Dec. 2023, doi: 10.1016/j.apmt.2023.101928.

[18] R. Banerjee, N. Bevilacqua, L. Eifert, and R. Zeis, "Characterization of carbon felt electrodes for vanadium redox flow batteries – A pore network modeling approach," *J Energy Storage*, vol. 21, pp. 163–171, Feb. 2019, doi: 10.1016/j.est.2018.11.014.

[19] Z. Cheng *et al.*, "Data-driven electrode parameter identification for vanadium redox flow batteries through experimental and numerical methods," *Appl Energy*, vol. 279, p. 115530, Dec. 2020, doi: 10.1016/j.apenergy.2020.115530.

[20] D. You, H. Zhang, and J. Chen, "A simple model for the vanadium redox battery," *Electrochim Acta*, vol. 54, no. 27, pp. 6827–6836, Nov. 2009, doi: 10.1016/j.electacta.2009.06.086.

[21] C. M. Krowne, "Nernst Equations and Concentration Chemical Reaction Overpotentials for VRFB Operation," *J Electrochem Soc*, vol. 170, no. 10, p. 100534, Oct. 2023, doi: 10.1149/1945-7111/ad0073.